

**US Army Corps
of Engineers®**
Engineer Research and
Development Center

Fast All-season Soil STrength (FASST)

Susan Frankenstein and George G. Koenig

September 2004

ERDC/CRREL SR-04-1
September 2004

Fast All-season Soil STrength (FASST)

Susan Frankenstein and George G. Koenig

Approved for public release; distribution is unlimited.

Prepared for U.S. ARMY CORPS OF ENGINEERS
 WASHINGTON, D.C. 20314-1000

ABSTRACT

The ability to predict the state of the ground is essential to manned and unmanned vehicle mobility and personnel movement, as well as determining sensor performance for both military and civilian activities. As part of the Army's Battlespace Terrain Reasoning and Awareness research program, the 1-D dynamic state of the ground model FASST (Fast All-season Soil STrength) was developed. It calculates the ground's moisture content, ice content, temperature, and freeze/thaw profiles, as well as soil strength and surface ice and snow accumulation/depletion. The fundamental operations of FASST are the calculation of an energy and water budget that quantifies both the flow of heat and moisture within the soil and also the exchange of heat and moisture at all interfaces (ground/air or ground/snow; snow/air) using both meteorological and terrain data. FASST is designed to accommodate a range of users, from those who have intricate knowledge of their site to those who know only the site location. It allows for 22 different terrain materials, including asphalt, concrete, bedrock, permanent snow, and the USCS soil types. At a minimum, the only weather information required is air temperature.

DISCLAIMER: The contents of this report are not to be used for advertising, publication, or promotional purposes. Citation of trade names does not constitute an official endorsement or approval of the use of such commercial products. All product names and trademarks cited are the property of their respective owners. The findings of this report are not to be construed as an official Department of the Army position unless so designated by other authorized documents. **DESTROY THIS REPORT WHEN IT IS NO LONGER NEEDED. DO NOT RETURN TO THE ORIGINATOR.**

THIS PAGE INTENTIONALLY LEFT BLANK.

CONTENTS

Preface	xvi
1 Introduction	1
1.0 Background	1
1.1 Overview	1
1.2 Basic Program Format	2
1.3 References	3
2 Shortwave (Solar) Radiation Model	4
2.0 Introduction	4
2.1 Downwelling Shortwave Radiation	4
2.2 Reflected Shortwave Radiation	6
2.3 Net Shortwave Radiation	6
2.4 Sloping Surface	6
2.5 Net Solar Flux on a Sloping Surface	7
2.6 Shortwave Solar Flux Model Validation	7
2.7 Model Input and Output	14
2.8 References	14
3 Longwave (IR) Radiation Model	15
3.0 Introduction	15
3.1 Downwelling Longwave Radiation	15
3.1.1 Modification of the Cloud Irradiance Factor (CIF)	17
3.2 Downwelling Infrared Flux Model Validation	18
3.3 Potential Modification	24
3.4 Upwelling Longwave Radiation	25
3.5 Model Input and Output	25
3.6 References	26
4 Soil Temperature Model	28
4.0 Introduction	28
4.1 Soil Thermal Model	28
4.1.1 Solar Radiation	29
4.1.2 Longwave Radiation	30
4.1.3 Sensible Heat	31
4.1.4 Latent Heat	32
4.1.5 Precipitation Heat	33
4.1.6 Final Top Boundary Equation	33
4.2 Numerical Solution	33
4.3 Material Properties	35
4.4 Model Validation	37
4.5 References	40
5 Soil Moisture and Strength Models	43
5.0 Introduction	43

5.1 Soil Moisture.....	43
5.1.1 Governing Equations	43
5.1.2 Numerical Solution	44
5.1.3 Hydraulic Parameters.....	45
5.1.4 Model Validation	48
5.2 Soil Strength.....	51
5.2.1 Theory	51
5.3 References.....	53
6 Ground State Model.....	55
6.0 Introduction.....	55
6.1 Physical Setup.....	55
6.2 Validation.....	56
6.3 References.....	57
7 Snow Accretion, Depletion, and Meltwater Outflow Model.....	58
7.0 Introduction.....	58
7.1 Governing Equations of Flow within the Snow.....	58
7.2 Evolution of Parameters.....	63
7.2.1 Grain Growth	63
7.2.2 Permeability	64
7.2.3 Irreducible Water Saturation.....	64
7.2.4 Snow Depth.....	64
7.2.5 Effective Saturation Exponent	65
7.2.6 Refreezing	65
7.3 Surface Energy Balance.....	66
7.4 Module Input and Output.....	66
7.5 Model Validation	67
7.6 References.....	69
8 Ice Thickness Model.....	71
8.0 Introduction.....	71
8.1 Theory	71
8.1.1 Growth	71
8.1.2 Decay	71
8.2 References.....	72
9 Model Inputs	73
9.0 Introduction.....	73
9.1 Meteorological Data.....	73
9.2 Soil Properties.....	75
9.3 Initial Conditions	79
9.4 Site Information	79
9.5 References.....	80

10 Model Initialization.....	81
10.0 Introduction.....	81
10.1 Surface Conditions.....	81
10.2 Temperature and Volumetric Moisture and Ice Content Profiles.....	81
10.3 Node Position and Number.....	82
10.4 Time Step Determination.....	82
10.5 References.....	83
11 Model Outputs	84
11.0 Introduction.....	84
11.1 Surface Condition Information	84
11.2 Soil Profile Information	86
11.3 Input/Output Data Source Information	86
11.4 References.....	86

FIGURES

Figure 1.1 Flowchart of the FASST Modules.....	3
Figure 2.1 Comparison of the measured and calculated total solar flux for a 10-day period for Grayling I. Only the values of the solar flux when the zenith angle is less than 90 degrees are plotted	8
Figure 2.2 Same as Figure 2.1 but for the direct component of the solar flux	8
Figure 2.3 Same as Figure 2.1 but for the diffuse solar flux	9
Figure 2.4 Scatter diagram of the total solar measured and calculated flux and the least square fit to the data.....	9
Figure 2.5 Calculated minus the measured total solar flux for different cloud conditions for Grayling I. The dashed lines are $\pm 50 \text{ W/m}^2$	11
Figure 2.6 Scatter diagram of the total solar measured and calculated flux and the least square fit to the data.....	12
Figure 2.7 Calculated minus the measured total solar flux for different cloud conditions for Yuma. The dashed lines are $\pm 50 \text{ W/m}^2$	12
Figure 2.8 Scatter diagram of the total solar measured and calculated flux and the least square fit to the data.....	13
Figure 2.9 Calculated minus the measured total solar flux for different cloud conditions for Grayling II. The dashed lines are $\pm 50 \text{ W/m}^2$	13
Figure 3.1 Calculated cloud irradiance in accordance with Equation (3.12) and the least square fit to the data points. Calculations are based on a mid-latitude summer atmosphere	17
Figure 3.2 Comparison of the downwelling measured and computed longwave flux based on the Grayling I meteorological observations	19
Figure 3.3 Comparison of the measured and model calculated downwelling longwave flux.....	19
Figure 3.4 Comparison of the downwelling measured and computed longwave flux based on the Yuma meteorological observations	20

Figure 3.5 Comparison of the measured and model calculated downwelling longwave flux.....	21
Figure 3.6 Comparison of the downwelling measured and computed longwave flux based on the Grayling II meteorological observations	22
Figure 3.7 Comparison of the measured and model calculated downwelling longwave flux.....	23
Figure 4.1 Surface Energy Balance	29
Figure 4.2 Sloped Solar Radiation Geometry	30
Figure 4.3 Comparison of model results and measurements for surface temperature (K) for Yuma, AZ	37
Figure 4.4 Effect on the results of having initial soil temperature profile data (yes) versus letting the model compute one (no). The number in the legend indicates the number of nodes.....	38
Figure 4.5 Sensitivity of the surface temperature to the albedo	39
Figure 4.6 The effect of soil type on surface temperature for Grayling, MI	39
Figure 4.7 Comparison of FASST and measured pavement surface temperatures	40
Figure 5.1 ψ versus θ for Yuma, AZ, sand.....	47
Figure 5.2 K versus θ and $\partial\theta/\partial\psi$ versus θ for Yuma, AZ, sand	47
Figure 5.3 Soil moisture comparisons for Grayling, MI, 1992.....	49
Figure 5.4 Soil moisture comparisons for Yuma, AZ	50
Figure 5.5 Investigation of soil type on soil moisture for Grayling, MI, 1992.....	50
Figure 6.1 Comparison of frost depth between FASST and measured values for South Royalton, VT	56
Figure 6.2 Comparison of FASST calculated frost depth and measured values as a function of soil depth and snow depth	57
Figure 7.1 Comparison between the measured snow depth and the snow depth calculated by FASST along with snow (yellow) and rain (blue) precipitation events for Sleepers River, VT	67
Figure 7.2 Comparison between the measured snow depth and the snow depth calculated by SNTHERM and FASST for Buffalo Pass, CO	68
Figure 7.3 Comparison between the measured snow depth and the snow depth calculated by SNTHERM and FASST for Indian River, CO	68

TABLES

Table 1.1.1 Meteorological information necessary for predicting the state of the ground	1
Table 2.6.1 Equation of fit (forced through the origin) and correlation coefficient for Grayling I	10
Table 2.6.2 Equation of fit (forced through the origin) and correlation coefficient for Yuma	11
Table 2.6.3 Equation of fit (forced through the origin) and correlation coefficient for Grayling II	11
Table 3.1.0 Coefficients for determining cloud base altitude (<i>meters</i>) as a function of season, latitude, and cloud type.....	16

Table 3.1.1 Calculated regressions for determining the cloud irradiance for the Geophysics Laboratory Model Atmospheres.....	18
Table 3.2.1 Grayling I average downwelling IR flux for different cloud conditions	20
Table 3.2.2 Yuma average downwelling IR flux for different cloud conditions.....	22
Table 3.2.3 Grayling II average downwelling IR flux for different cloud conditions.....	23
Table 4.3.1 Default Soil Properties.....	36
Table 5.1.1 Default Soil Moisture Properties	46
Table 5.2.1 Default Soil Strength Coefficients.....	52
Table 9.2.1 FASST Default Soil Properties.....	77
Table 9.2.2 FASST Default Soil Moisture Properties	78

NOMENCLATURE

Chapter 1

CI	Cone Index
VCI	Vehicle Cone Index
z_{wet}	frost depth over wet unfrozen soil (m)
z_{dry}	frost depth over dry unfrozen soil (m)

Chapter 2

α	surface albedo
φ_k	fraction of sky that is cloud covered ($\varphi_k = Wf_k$)
φ_o	solar zenith angle (radians)
φ	surface slope angle (radians)
ρ_k	cloud reflectance
τ_k	cloud transmission
ϑ_o	solar azimuth angle relative to north (radians)
ϑ	surface azimuth angle relative to north (radians)
ϑ_r	relative azimuth angle (radians) ($\vartheta_r = \vartheta - \vartheta_o$)
$a_k^0, a_k^1, a_k^2, a_k^3$	calculation coefficients
$aa_k^0, aa_k^1, aa_k^2, aa_k^3$	calculation coefficients
A_k	absorption of solar radiation by the atmosphere
$b_k^0, b_k^1, b_k^2, b_k^3$	calculation coefficients
$bb_k^0, bb_k^1, bb_k^2, bb_k^3$	calculation coefficients
c_1, c_2, c_3, c_4, c_5	calculation coefficients
D, d	calculation constants
f_k	fractional cloud amount
f_s	calculation factor
$I_s \downarrow^k$	downwelling solar flux for layer k (W/m^2)
$I_s \uparrow^k$	upwelling solar flux for layer k (W/m^2)
$I_s \downarrow$	downwelling solar flux at the ground (W/m^2) ($I_s \downarrow = I_s \downarrow^{dir} + I_s \downarrow^{dif}$)
$I_s \uparrow$	upwelling solar flux at the ground (W/m^2)
$I_s \downarrow^{dir}$	direct downwelling solar flux at the ground (W/m^2)
$I_s \downarrow^{dif}$	diffuse downwelling solar flux at the ground (W/m^2)
ΔI_s	net solar flux at the ground (W/m^2) ($\Delta I_s = I_s \downarrow - I_s \uparrow$)
I_o	solar flux at the top of the atmosphere ($I_o = 1369.3 \text{ } W/m^2$)
$I_s \uparrow^c$	upwelling solar flux corrected for a sloping surface (W/m^2)
$I_s \downarrow^{cdir}$	direct downwelling solar flux at the ground corrected for a sloping surface (W/m^2)
$I_s \downarrow^{cdif}$	diffuse downwelling solar flux at the ground corrected for a sloping surface (W/m^2)
k	subscript indicating atmospheric layer ($k = 0$ is the top of the atmosphere)
r_k	clear sky reflectance
R_k	reflectance of solar radiation by the atmosphere

t_k	clear sky transmission
T_k	transmission of solar radiation by the atmosphere ($T_k = T_k^{dir} + T_k^{dif}$)
T_k^{dir}	transmission of direct solar radiation by the atmosphere
T_k^{dif}	transmission of diffuse solar radiation by the atmosphere
W	cloud weighting factor

Chapter 3

$\chi_{(l,m,h)}$	cloud irradiance factor for low (middle, high) clouds
ε_a	atmospheric emissivity
λ	latitude
σ	Stefan-Boltmann constant ($\sigma = 5.669 \times 10^{-8} \text{ W/m}^2 \cdot \text{K}^4$)
$a_{(l,m,h)}$	parameterization coefficients for determining cloud height
$b_{(l,m,h)}$	parameterization coefficients for determining cloud height
$c_{(l,m,h)}$	parameterization coefficients for determining cloud height
$c_{(l,m,h)}$	fractional low (middle, high) cloud cover
c_{eff}^m	effective middle cloud cover amount
c_{eff}^h	effective high cloud cover amount
CIF	cloud irradiance factor
$d_{(l,m,h)}$	parameterization coefficients for determining cloud height
e_a, e_{as}	vapor pressure, saturated vapor pressure (mbar)
e_{so}	saturated vapor pressure at a standard pressure of 6.11 mbar (mbar)
$I_{ir\downarrow}^{clr}$	clear sky downwelling longwave radiation (W/m^2)
$I_{ir\downarrow}^{cld}$	cloudy sky downwelling longwave radiation (W/m^2)
l	latent heat of evaporation (sublimation) [$l = 2.505 \times 10^5 \text{ J/kg}$ ($2.838 \times 10^6 \text{ J/kg}$)]
R_v	gas constant for water vapor ($R_v = 461.296 \text{ J/kg} \cdot \text{K}$)
RH	relative humidity ($RH = e_a/e_{as}$)
T_a	ambient air temperature (K)
T_c	cloud base temperature (K)
T_o	standard temperature ($T_o = 273.15 \text{ K}$)
$Z_{(l,m,h)}$	height to base of low (middle, high) clouds (km)

Chapter 4

α	surface albedo
$\alpha_{j,i}$	numerical calculation constant
$\beta_{j,i}$	numerical calculation constant
$\delta_{j,i}$	numerical calculation constant
ε	surface emissivity
$\phi_{j,i}$	numerical calculation constant (K)
γ_d	bulk dry density of soil (kg/m^3)
γ_p	precipitation density (kg/m^3)
$\gamma_{j,i}$	numerical calculation constant
Γ_h	sensible heat exchange stability correction factor
κ	soil thermal conductivity ($\text{W/m} \cdot \text{K}$)

κ_{dry}	dry soil thermal conductivity ($W/m \cdot K$)
κ_i	thermal conductivity of ice ($W/m \cdot K$)
κ_{sat}	saturated soil thermal conductivity ($W/m \cdot K$)
κ_s	soil solids thermal conductivity ($W/m \cdot K$)
κ_w	thermal conductivity of water ($W/m \cdot K$)
$\mu_{j,i}$	numerical calculation constant
θ_i	volumetric ice content (cm^3/cm^3)
θ_{of}	organic fraction of solids (cm^3/cm^3)
φ	surface zenith (elevation) angle (<i>radians</i>)
φ_0	solar zenith angle (<i>radians</i>)
ρ_a	air density (kg/m^3) [$\rho_a = 0.00348(P_a/T_a)$]
ρ_i	ice density (kg/m^3) ($\rho_i = 916.5\ kg/m^3$)
ρ_w	water density (kg/m^3) ($\rho_w = 1000.0\ kg/m^3$)
σ	Stefan-Boltzmann constant ($\sigma = 5.669e-08\ W/m^2 \cdot K^4$)
ϑ	surface azimuth angle measured clockwise from north (<i>radians</i>)
ϑ_0	solar azimuth angle measured clockwise from north (<i>radians</i>)
$\Delta\vartheta$	relative azimuth angle (radians) ($\Delta\vartheta \equiv \vartheta - \vartheta_0 $)
B_i	numerical calculation constant (K)
c_p	specific heat of a material ($J/kg \cdot K$)
$c_{p,a}$	specific heat of dry air at constant pressure ($c_{p,a} = 1005.6\ J/kg \cdot K$)
$c_{p,w}$	specific heat of water ($c_{p,w} = 4217.7\ J/kg \cdot K$)
$c_{p,i}$	specific heat of ice ($c_{p,i} = -13.3 + 7.80T_a\ J/kg \cdot K$)
c_1, c_2	numerical calculation constants (K^3, K^4)
C	volumetric heat capacity (specific heat) ($J/m^3 \cdot K$)
C_a	specific heat of air ($C_a = 1005.6\ J/kg \cdot K$)
C_D^h	drag coefficient for sensible heat
C_D^e	drag coefficient for latent heat
$C_{hn}^{g_0}$	bulk transfer coefficient near the ground for sensible heat
C_s	specific heat of solids ($J/kg \cdot K$)
C_w	heat capacity of water ($C_w = 4217.7\ J/kg$)
e_d	vapor pressure (Pa)
e_0	windless exchange coefficient for sensible heat ($2.0\ W/m^2$)
g	gravitational acceleration ($9.81\ m/s^2$)
H	sensible heat flux from the surface (W/m^2)
I_{ir}^{\downarrow}	incoming longwave radiation at the surface (W/m^2)
I_{ir}^{\uparrow}	outgoing longwave radiation at the surface (W/m^2) (relected and emitted)
$I_{ir,emit}^{\uparrow}$	emitted longwave radiation from the surface (W/m^2) ($I_{ir,emit}^{\uparrow} = \varepsilon\sigma T^4$)
I_s^{\downarrow}	net solar radiation on the surface (W/m^2) ($I_s^{\downarrow} = I_s^{\downarrow dir} + I_s^{\downarrow dif}$)
$I_s^{\downarrow slope}$	net solar radiation for a sloped surface (W/m^2)
$I_s^{\downarrow dif}$	diffuse solar radiation on the surface (W/m^2)
$I_s^{\downarrow dir}$	direct solar radiation on the surface (W/m^2)
j, i	subscripts for time and depth, respectively
l	latent heat (J/kg)

l_{evap}	latent heat of evaporation ($l_{evap} = 2.505 \times 10^5 \text{ J/kg}$)
l_{fus}	latent heat of fusion ($l_{fus} = 3.335 \times 10^5 \text{ J/kg}$)
l_{sub}	latent heat of sublimation ($l_{sub} = 2.838 \times 10^6 \text{ J/kg}$)
L	latent heat flux from the surface (W/m^2)
k_{th}	soil thermal diffusivity (m^2/s)
k	von Karman's constant (0.4)
K_e	Kersten number
M_g	moisture factor ($0 \leq M_g \leq 1$)
n	porosity
P	precipitation heat flux from the surface (W/m^2)
P_a	air pressure (Pa)
q	quartz content
q_a	mixing ratio of the air at 2 m
q_g	mixing ratio
q_s	saturated mixing ratio
r_{ce}	turbulent Prandtl number (0.71)
r_{ch}	turbulent Schmidt number (0.63)
R_{ib}	bulk Richardson number
S_c	calculation factor
S_r	degree of saturation
t	time (sec)
Δt	time step (sec)
T	soil temperature (K)
T_a	air temperature (K)
T_p	precipitation temperature (K)
U_p	mass precipitation flux ($\text{kg/m}^2 \cdot \text{s}$)
wi	frozen water volume fraction
ww	unfrozen water volume fraction ($ww = S_r n$)
W	wind speed (m/s)
W'	wind speed corrected for gustiness (m/s) ($W' = 2.0$ if $W < 2.0$)
z	soil depth (m)
z_0^g	ground roughness length (0.0006 m for snow/ice, 0.0001 m for pavements, 0.001 m for all soils)
Δz	node spacing (m)
Z	site elevation (m)
Z_a	air temperature, wind speed, and relative humidity measurement height (m)

Chapter 5

α	surface albedo
α_{vG}	van Genuchten pressure head constant (cm^{-1})
ε	surface emissivity
γ_i	numerical calculation variable (m^{-1})
ϕ_i	numerical calculation variable (m^{-1})

ϕ	surface slope
κ	soil thermal conductivity ($W/m \cdot K$)
θ_w	volumetric moisture content (cm^3/cm^3)
θ_i	volumetric ice content (cm^3/cm^3)
θ_{max}	maximum volumetric moisture content (cm^3/cm^3)
θ_r	residual volumetric moisture content (cm^3/cm^3)
ρ_a	air density (kg/m^3)
ρ_i	ice density (kg/m^3) ($\rho_i = 916.5 \text{ kg/m}^3$)
ρ_s	soil density (kg/m^3)
ρ_w	water density ($\rho_w = 1000 \text{ kg/m}^3$)
σ	Stefan-Boltzmann constant ($\sigma = 5.669e-08 \text{ W/m}^2 \cdot K^4$)
Ψ	pressure head (m) ($\Psi = P_f/\rho_w g$)
$\Delta\Psi_{j,i}$	change in pressure head per time step Δt (m)
a_i^+	numerical calculation variable (m^{-1})
a_i^-	numerical calculation variable (m^{-1})
B_i	numerical calculation variable
c_p	specific heat of a material ($J/kg \cdot K$)
$c_{p,a}$	specific heat of dry air at constant pressure ($c_{p,a} = 1005.6 \text{ J/kg} \cdot K$)
c_1, c_2	calculation constants
C_r	condensation rate (m/s)
C_D	drag coefficient
CI	cone index
E	evaporation rate (m/s)
g	gravitational constant ($g = 9.81 \text{ m/s}^2$)
h	total head (m) ($h = z_e \cos \phi - \Psi$)
h_{pond}	head due to water collecting on the surface (m)
$h_{i,melt}$	head due to ice melt (m)
$h_{s,melt}$	head due to snow melt (m)
I_{ir}^\downarrow	incoming longwave radiation (W/m^2)
I_s^\downarrow	net solar radiation at the surface (W/m^2)
j, i	subscripts for time and depth, respectively
K	hydraulic conductivity (m/s)
K_{sat}	saturated hydraulic conductivity (m/s)
l	latent heat of evaporation (sublimation) [$l = 2.505 \times 10^5 \text{ J/kg}$ ($2.838 \times 10^6 \text{ J/kg}$)]
m_{vG}	van Genuchten constant ($m_{vG} = 1 - 1/n_{vG}$)
MC	percent moisture content by weight (% g/g)
n	porosity
n_{vG}	van Genuchten constant
P	precipitation rate (m/s)
P_f	fluid pressure at depth z (m)
q_{bot}	moisture flux at the bottom of the soil layer (m/s)
q_{top}	total moisture flux at the surface (m/s)
RCI	rating cone index

t	time (sec)
Δt	time step (sec)
T	surface temperature (K)
T_a	air temperature (K)
T_p	precipitation temperature (K)
U_p	mass precipitation flux ($kg/m^2 \cdot s$)
v	fluid flow through a porous media (m/s)
VCI	vehicle cone index
w	relative soil moisture
W	wind speed (m/s)
z	depth (m) (equivalent to the elevation head)
z_{wet}	frost depth over wet unfrozen soil (m)
z_{dry}	frost depth over dry unfrozen soil (m)
Δz_i	node spacing (m)

Chapter 6

θ_k	volume fraction of the soil constituents (cm^3/cm^3)
θ_r	residual volumetric moisture content (cm^3/cm^3)
$\Delta\theta_i$	change in volumetric ice content (cm^3/cm^3)
ρ_k	density of the soil constituents (kg/m^3)
c_{p_k}	specific heat of the soil constituents (J/kg)
l_{fus}	latent heat of fusion ($l_{fus} = 3.335 \times 10^5 J/kg$)
ΔQ_1	node energy (J/m^3)
ΔQ_2	freeze/thaw energy (J/m^3)
T_i	node temperature (K)
dt	time step (sec)
dz	nodal thickness (m)
Δz_i	node thickness (m)

Chapter 7

α_{cc}	calculation constant ($\alpha_{cc} = 1/\eta_{cf}$)
α	albedo at the snow surface
β	calculation constant ($\beta = -1/\eta_{cf}$)
χ	depth coordinate (cm) ($\chi = x + c_l$)
δ	time between the formation of wave U_1 and wave U_2 (sec)
ϕ	total pore volume per total volume
ϕ_e	effective pore volume/total volume
κ_{cf}	calculation factor
κ	soil thermal conductivity ($W/m \cdot K$)
η_{cf}	calculation factor ($\eta_{cf} = 1 - 1/n_c$)
η_c	dynamic viscosity coefficient ($g/cm \cdot s$)
η_o	base dynamic viscosity coefficient ($\eta_o = 5e08 g/cm \cdot s$)
η_w	dynamic water viscosity ($g/cm \cdot s$)

ρ	medium density (g/cm^3)
ρ_i	ice density within the snowpack (g/cm^3)
ρ_s	snow density (g/cm^3)
ρ_t	total density of the solid and liquid phases within the snow (g/cm^3)
ρ_w	density of water ($1 g/cm^3$)
σ_{wa}	wave area (cm^2)
τ	time coordinate (<i>sec</i>) ($\tau = t + c_2$)
τ_o	time for wave to reach depth D (<i>sec</i>)
Δ_2	total water volume the U_2 wave has absorbed (cm)
A	input wave volume per unit area, or runoff volume (cm)
A_m	wave volume at time τ_o (cm)
$A_{(I,II)}$	initial mobile water volume of the U_1 , U_2 wave (cm)
B	calculation constant ($B = K_{cf}^{-\sqrt{\eta_{ef}}}$)
c_1, c_2	depth and time offsets, respectively (cm , <i>sec</i>)
c_1, c_2	calculation variables
d	snow grain diameter (cm)
dA_m	differential mobile water element (cm)
D	depth of wave penetration at time τ_o (cm)
D_s	snow depth (cm)
f_l	fraction of snowpack that is wet
g	gravitational constant ($981 cm/s^2$)
H	sensible heat flux (W/m^2)
I_{conv}	convective heat flux (W/m^2)
I_{ir}^\downarrow	incoming longwave radiation at the surface (W/m^2)
I_{ir}^\uparrow	outgoing longwave radiation at the surface (W/m^2)
$I_s \downarrow$	net solar radiation at the surface (W/m^2)
I_{top}	energy balance at the top of the snowpack (W/m^2)
k_{w0}	water permeability (cm^2)
k_w	relative water permeability (cm^2)
k_{th}	thermal conductivity of the medium in the refrozen state ($k_{th} = 0.0045 J/s cm \cdot ^\circ C$)
l_f	latent heat of fusion ($l_f = 3.335e05 J/kg$)
L	latent heat flux (W/m^2)
n_c	proportionality constant ($n_c = 3.3$)
\bar{P}_s	average pressure load within the snowpack ($g \cdot sm/s^2$)
S_I	residual water saturation of wave 1
S_e	effective water saturation
S_{wa}	absolute water saturation
S_{wi}	irreducible water saturation
SWE	snow water equivalent (cm)
t	time (<i>sec</i>)
T	snow and soil temperature ($^\circ C$)
T_f	fusion temperature ($^\circ C$)

U	volume flux of water (cm/s)
U'	change in water volume flux with depth (cm/s)
V_{av}	average snow crystal volume (cm^3)
x	depth position (cm)
x_{A2}	deepest depth of wave 2 at which the solution still applies (cm)
x_u	depth of wave penetration (cm)
X	freezing front depth (cm)
z	soil depth (m)
$I, 2$	subscripts indicating wave number

Chapter 8

κ	soil thermal conductivity ($W/m \cdot K$)
ρ_i	ice density ($\rho_i = 916.5 \text{ kg/m}^3$)
ρ_w	water density ($\rho_w = 1000 \text{ kg/m}^3$)
c_i	specific heat of ice ($c_i = -13.3 + 7.80T_s \text{ J/kg} \cdot K$)
f	fraction of precipitation that freezes
h_i	ice thickness (m)
Δh_i	change in ice thickness due to melting (m)
l_f	latent heat of fusion ($l_f = 3.335e05 \text{ J/kg}$)
P	precipitation rate (m/hr)
q_{net}	net heat flux to surface (W/m^2)
Δt	time step (sec)
T_s	surface temperature (K)

Chapter 9

α	soil albedo
α_{vG}	van Genuchten pressure head constant (cm^{-1})
ε	soil emissivity
γ_d	bulk density of the soil (g/cm^3)
η	dynamic fluid viscosity ($kg/m \cdot s$)
κ	thermal conductivity of the soil ($W/m \cdot K$)
κ_a	thermal conductivity of air ($W/m \cdot K$)
κ_{dry}	thermal conductivity of the dry soil ($W/m \cdot K$)
κ_s	thermal conductivity of the solids ($W/m \cdot K$)
ν	kinematic fluid viscosity (m^2/s)
θ_d	volume fraction of soil solids (cm^3/cm^3)
θ_{max}	maximum volumetric moisture content (cm^3/cm^3)
θ_{of}	organic fraction (cm^3/cm^3)
θ_r	residual volumetric moisture content (cm^3/cm^3)
θ_w	volumetric moisture content (cm^3/cm^3)
ρ_d	intrinsic density of the soil (g/cm^3)
ρ_f	fluid density (kg/m^3)
c_1, c_2	soil strength of solids coefficients

C	specific heat ($J/kg \cdot K$)
CI	cone index
d	soil grain diameter (m)
e	void ratio
g	gravitational constant (9.81 m/s^2)
k_{th}	soil thermal diffusivity (m^2/s)
$k_{p_{sat}}$	saturated permeability (cm^2)
K	hydraulic conductivity (m/s)
K_{sat}	saturated hydraulic conductivity (cm/s)
m_{vG}	van Genuchten exponent relating soil moisture to pressure head ($m_{vG} = 1 - 1/n_{vG}$)
MC	soil moisture content (kg/kg)
n_{vG}	van Genuchten exponent relating soil moisture to pressure head
n	porosity
N	proportionality factor
q	quartz content
RCI	rating cone index
T_a	air temperature (K)
w	relative soil moisture

Chapter 10

$\alpha_{s,i}$	snow (s), ice (i) albedo
$\varepsilon_{s,i}$	snow (s), ice (i) emissivity
k_{th}	soil thermal diffusivity (m^2/s)
Δt	time step (sec)
Δz	nodal thickness (m)

PREFACE

This report was prepared by Dr. Susan Frankenstein and Dr. George G. Koenig, Research Physical Scientists, Geophysical Sciences Branch, Cold Regions Research and Engineering Laboratory (CRREL), U.S. Army Engineer Research and Development Center (ERDC), Hanover, New Hampshire.

This report was prepared under the general supervision of Dr. Richard M. Detsch, Chief, Geophysical Sciences Branch, CRREL; Dr. Lance D. Hansen, Deputy Director, CRREL; and James L. Wuebben, Acting Director, CRREL.

Funding was provided by AT42.

The Commander and Executive Director of the Engineer Research and Development Center is Colonel James R. Rowan. The Director is Dr. James R. Houston.

Chapter 1

Introduction

1.0 Background

The ability to predict the state of the ground is essential to vehicle mobility, both manned and unmanned, and personnel movement, as well as determining sensor performance. Trafficality, or ease of travel, is dictated by both soil strength and surface friction. Surface friction decreases in the presence of an ice or snow layer or when the top of the ground becomes too wet. Soil strength depends on the soil type and the distribution of moisture and ice with depth. For instance, the presence of a thawed layer (wet, low bearing capacity) overlying a competent layer of frozen ground has a negative impact on mobility as motion resistance increases and traction decreases (Sullivan et. al. 1997). Infrared and radar sensor performance is determined, in part, by the state of the ground. Weather-impacted state-of-the-ground conditions resulting in a high degree of clutter can degrade sensor performance.

1.1 Overview

The fundamental operations of FASST (Fast All-seasons Soil STrength) are the calculation of an energy and water budget that quantifies both the flow of heat and moisture within the soil and also the exchange of heat and moisture at all interfaces (ground/air or ground/snow; snow/air). To do this, FASST uses up to nine modules (Section 1.2). If all the necessary weather parameters (Table 1.1.1) are known from real-time data entry, a climatic database, or a mesoscale forecast model, then the only modules used are those that determine the state of the ground. These modules predict the soil temperature and moisture profiles and ultimately the thickness of any frozen and/or thawed soil layers. Otherwise, the solar radiation flux and the infrared radiation flux are calculated using the two radiation modules (Module 4) and the snow depth is calculated with the Snow Accretion–Depletion Module (Module 7). In both cases, FASST requires information on latitude, longitude, slope, aspect, elevation, and ground cover. The required information can be obtained from a TEM (Terrestrial Ecosystem Mapping) geographic information system. FASST is a one-dimensional model run in a distributed mode. That is, FASST is then run for each region object in the Area Of Interest (AOI). Region objects represent areas with similar attributes (slope, aspect, soil, and land cover).

Table 1.1.1 Meteorological information necessary for predicting the state of the ground

Radiation (W/m^2)	Incident and reflected shortwave radiation (0.3–3 μ); Downwelling and upwelling longwave radiation (3–50 μ)
Air temperature ($^{\circ}C$)	
Relative humidity (%)	
Wind speed (m/s)	
Snow depth (cm)	
Precipitation (mm water/ hr)	

The Snow Accretion–Depletion Module is also used to predict the amount of water available from snowmelt. If the ground surface is frozen, the meltwater is assumed to run off and the moisture content of the soil is unchanged. If there is a thawed layer, the moisture content of the soil increases, as the meltwater infiltrates the soil. If the Snow Accretion–Depletion Module is not being used to calculate the amount of meltwater from the snowpack, then the available water (cm) is assumed to be 0.28 times the change in thickness of the snow cover (cm). A factor of 0.28 instead of 0.33 is used to allow for the likelihood that some of the water in the snowpack evaporates and some of it runs off once the thawed soil layer is near saturation.

1.2 Basic Program Format

The individual models comprising FASST are grouped into nine modules. These modules accomplish the following tasks:

1. Read in the meteorological data and make any necessary unit conversions and assumptions. (Chapter 9)
2. If the solar or infrared flux information is missing, generate the appropriate values based on the cloud amount and type for all required flux information except the ground emitted IR flux, which is dependent on the surface temperature. (Chapters 2 and 3)
3. Read in the control file containing information concerning initial conditions, soil profile, and meteorological data. (Chapter 9)
4. Initialize the soil profile and the state of the ground. (Chapter 10)

START OF MAIN CALCULATION LOOP

5. Calculate the emitted and net IR fluxes. (Chapter 3)
6. Calculate the soil temperature and volumetric moisture content profiles. (Chapters 4 and 5)
7. Check for freezing and/or thawing. Calculate the soil strength. (Chapters 5 and 6)
8. If there is snow or ice on the ground, check to see if it is melting or accumulating. If it is melting, calculate the corresponding amount of runoff. (Chapters 7 and 8)
9. Check the calculation time increment, update as necessary.

END OF MAIN CALCULATION LOOP

10. Output the results.

A graphic representation of the above process is shown in Figure 1.1.

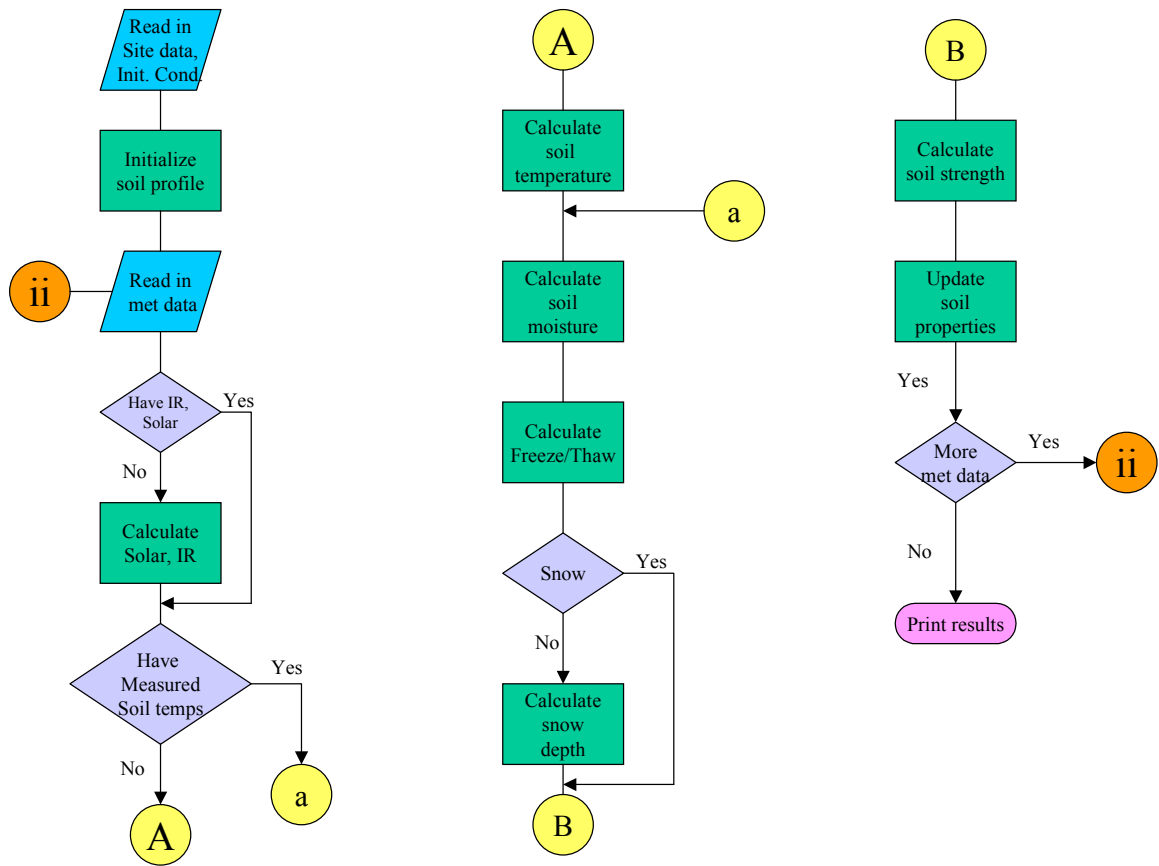


Figure 1.1 Flowchart of the FASST Modules.

1.3 References

Sullivan, P.M., C.D. Bullock, N.A. Renfroe, M.R. Albert, G.G. Koenig, L. Peck, and K. O'Neill (1997) Soil Moisture Strength Prediction Model Version II (SMSPII). U.S. Army Corps of Engineers Waterways Experiment Station, Technical Report GL-97-15.

Chapter 2

Shortwave (Solar) Radiation Model

2.0 Introduction

An important component of the surface energy budget is the solar net radiation. The solar radiation at the surface consists of direct and diffuse components. The relative magnitude of these two components depends in a large part on the optical depth of the clouds. As the cloud optical depth increases, the direct component will decrease, while the diffuse component may increase initially if the optical depth is small enough. As the optical depth increases beyond some threshold value, the diffuse component will decrease.

2.1 Downwelling Shortwave Radiation

Shapiro (1987, 1982, 1972) developed a simple model to determine the direct and diffuse shortwave irradiance at the surface using only standard surface meteorological observations. The Shortwave Radiation Module (SRM) developed for FASST uses this model to determine the downwelling shortwave irradiance. The module also uses a simple reflected shortwave irradiance model based on the downwelling shortwave irradiance and knowledge of the surface albedo. Surface albedo is parameterized in terms of the land surface type. For example, the albedo for grass is given as 0.20 and for sand as 0.40. For each land type there will be an albedo value based on that land type. The Solar Radiation Module requires cloud information that can be obtained from observations, climatology or cloud conditions generated by mesoscale forecast models such as the Army's Boundary layer Forecast Model (BFM).

The basic model approach involves dividing the atmosphere into k layers and assuming

$$R_k + T_k + A_k = 1. \quad (2.1)$$

R , T , and A are the reflectance, transmission, and absorption of layer k . In the SRM R , T , and A have been parameterized in terms of the solar zenith angle, φ_o , and the state of the atmosphere/clouds using the very extensive SOLMET database (NOAA 1979). The general form of the flux equations is

$$I_{s\downarrow}^k = T_k I_{s\downarrow}^{k-1} + R_k I_{s\uparrow}^k \quad (2.2a)$$

$$I_{s\uparrow}^k = T_{k+1} I_{s\uparrow}^{k+1} + R_{k+1} I_{s\downarrow}^k. \quad (2.2b)$$

Layer $k = 0$ is the top of the atmosphere. For operational use, the atmosphere has been divided into three layers consistent with the concept of low, middle, and high clouds. The downwelling solar flux at the ground (bottom of layer 3) is given as

$$I_{s\downarrow} = T_1 T_2 T_3 / D_2 \quad (2.3)$$

$$D_2 = d_3 \left(d_1 d_2 - R_1 R_2 T_2^2 \right) - d_1 R_2 \alpha T_3^2 - R_1 \alpha (T_2 T_3)^2 \quad (2.3a)$$

$$d_j = 1 - R_j R_{j-1}. \quad (2.3b)$$

α is the ground albedo. Assuming the total transmission T_k can be specified as the sum of the transmission of the direct solar component T_k^{dir} and the diffuse solar component T_k^{dif} , T_k can be written as

$$T_k = T_k^{dir} + T_k^{dif}. \quad (2.4)$$

The direct solar flux component at the ground is given as

$$I_{s\downarrow}^{dir} = T_1^{dir} T_2^{dir} T_3^{dir} I_{o\downarrow} \quad (2.5)$$

and the diffuse component as

$$I_{s\downarrow}^{diff} = I_{s\downarrow} - I_{s\downarrow}^{dir}. \quad (2.6)$$

$I_{o\downarrow}$ ($=1369.3 \text{ W/m}^2$) is the shortwave flux at the top of the atmosphere. In order to solve the above equations for the downwelling direct and diffuse flux it is necessary to assume

$$T_k^{dif} = R_k \quad (2.7)$$

and therefore T_k^{dir} can be obtained from

$$T_k^{dir} = T_k - T_k^{dif}. \quad (2.8)$$

Shapiro parameterized T_k and R_k in terms of the atmospheric and cloud conditions as follows:

$$R_k = \varphi_k \rho_k + (1 - \varphi_k) r_k \quad (2.9)$$

$$T_k = \varphi_k \tau_k + (1 - \varphi_k) t_k \quad (2.10)$$

$$\varphi_k = W f_k. \quad (2.11)$$

ρ_k is the cloud reflectance for cloud layer k , r_k the clear sky reflectance for layer k , τ_k the cloud transmission for layer k , t_k the clear sky transmission for layer k , f_k the fractional cloud amount for layer k , and W is a cloud weighting factor. ρ , r , t , τ , and W are parameterized in terms of the cosine of the solar zenith angle using the SOLMET data set.

$$\rho_k = a_k^o + a_k^1 + a_k^2 \cos^2 \varphi_o + a_k^3 \cos^3 \varphi_o \quad (2.12a)$$

$$r_k = a a_k^o + a a_k^1 + a a_k^2 \cos^2 \varphi_o + a a_k^3 \cos^3 \varphi_o \quad (2.12b)$$

$$t_k = b_k^o + b_k^1 + b_k^2 \cos^2 \varphi_o + b_k^3 \cos^3 \varphi_o \quad (2.12c)$$

$$\tau_k = b b_k^o + b b_k^1 + b b_k^2 \cos^2 \varphi_o + b b_k^3 \cos^3 \varphi_o. \quad (2.12d)$$

The coefficients (a_k 's, $a a_k$'s, b_k 's and $b b_k$'s) are parameterized in terms of the following atmospheric and cloud categories: clear, smoke and haze, thin cirrus and cirrostratus, thick cirrus and cirrostratus, altostratus and altocumulus, and low clouds. The cloud weighting factor W is given as

$$W = c_o + c_1 \cos \varphi_o + c_2 f_k + c_3 f_k \cos \varphi_o + c_4 \cos^2 \varphi_o + c_5 f_k^2. \quad (2.13)$$

The c 's are parameterized in terms of the following cloud categories: thin cirrus and cirrostratus, thick cirrus and cirrostratus, altostratus and altocumulus, and low clouds. The value of the coefficients can be found in the code or in Shapiro (1987).

2.2 Reflected Shortwave Radiation

The reflected shortwave flux is calculated from the downwelling shortwave flux and the surface albedo as follows

$$I_{s\uparrow} = \alpha I_{s\downarrow}. \quad (2.14)$$

The surface albedo α has been parameterized in terms of the land cover type.

2.3 Net Shortwave Radiation

The net shortwave radiation on a horizontal surface is given as

$$\Delta I_s = I_{s\downarrow} - I_{s\uparrow}. \quad (2.15)$$

2.4 Sloping Surface

All fluxes calculated above pertain to a flat surface. If the surface is sloping, correction factors must be used to get the insolation at the surface. The correction factor differs for the different components of the solar flux: downwelling direct, diffuse, total, and the reflected flux. For the direct beam, the corrected downwelling shortwave flux impinging on a sloping surface is given as

$$I_{s\downarrow}^{cdir} = I_{s\downarrow}^{dir} [\cos \varphi + \sin \varphi_o \sin \varphi \cos \vartheta_r / \cos \varphi_o]. \quad (2.16)$$

φ is the slope of the surface, and ϑ_r is the relative azimuth and is defined as the difference $(\vartheta - \vartheta_o)$ between the azimuth of the surface ϑ relative to north and the solar azimuth ϑ_o relative to north. The corrected diffuse component for a sloping surface is given as

$$I_{s\downarrow}^{cdiff} = I_{s\downarrow}^{diff} \left\{ \left[(180 - \vartheta_r) (f_s + \cos \vartheta_r) + \vartheta_r (1 + f_s \cos \vartheta_r) \right] / 180 (1 + f_s) \right\}. \quad (2.17)$$

f_s is given as

$$f_s = 1 + 0.5 \sin \varphi_o + 2 \sin(2\varphi_o). \quad (2.18)$$

The corrected reflected solar flux for a sloping surface is given as

$$I_{s\uparrow}^c = I_{s\uparrow} (1 - \cos \varphi) / 2. \quad (2.19)$$

2.5 Net Solar Flux on a Sloping Surface

The net solar flux on a sloping surface is given as

$$\Delta I_s = (I_{s\downarrow}^{cdiff} + I_{s\downarrow}^{cdir}) - I_{s\uparrow}^c. \quad (2.20)$$

2.6 Shortwave Solar Flux Model Validation

The Smart Weapons Operability Enhancement (SWOE) field program data were used to evaluate the shortwave solar flux model. The SWOE field programs were conducted during the fall of 1992 (Grayling I-Grayling, MI), the spring/summer of 1993 (Yuma, AZ), and the winter/spring of 1994 (Grayling II-Grayling, MI). Each program ran for approximately 44 days and meteorological information was collected at several locations in a 2-km-square area with a temporal frequency of one minute. Hourly average values of the meteorological information were used to evaluate the solar flux model. The hourly average values were computed using the one-minute values for a period of 30 minutes before and after the hour. The exception was the cloud amount information. During Grayling I, observations of the cloud cover were made on the hour from approximately 0700 to 1900 local. It should be realized that the cloud amount might not be consistent with the hourly average values of the measured solar flux. Since the exact time of the cloud observations is unknown, it is not possible to use the one-minute observation that corresponds to the cloud amount. Cloud amount can have a significant impact on both the direct and the diffuse solar flux. In general, an increase in the cloud amount will decrease the direct component of the solar flux and will increase the diffuse (more of the direct is scattered as diffuse) up to some value of cloud optical depth. Beyond this value the diffuse will decrease. The analysis presented deals only with the daytime solar flux values, that is, observations and model calculated values when the solar zenith angle is less than 90 degrees.

Figure 2.1 is a comparison of the model calculated total solar flux and the corresponding measured flux for a 10-day period. Some of the differences can be directly attributed to the fact that the measured values are one-hour averages while the calculated values basically use the instantaneous cloud observation. The phasing and the amplitudes match fairly well for clear conditions. Differences occur mainly for cloudy conditions. The components of the solar flux are presented in Figures 2.2 and 2.3. As the cloud amount increases, the direct solar flux decreases while the diffuse tends to increase. The solar flux model does not require cloud optical depth information. The dependence on optical depth is implicit in the coefficients for transmission, reflectance, and the cloud weighting function. As indicated above, the diffuse component should decrease when the optical depth exceeds some critical value.

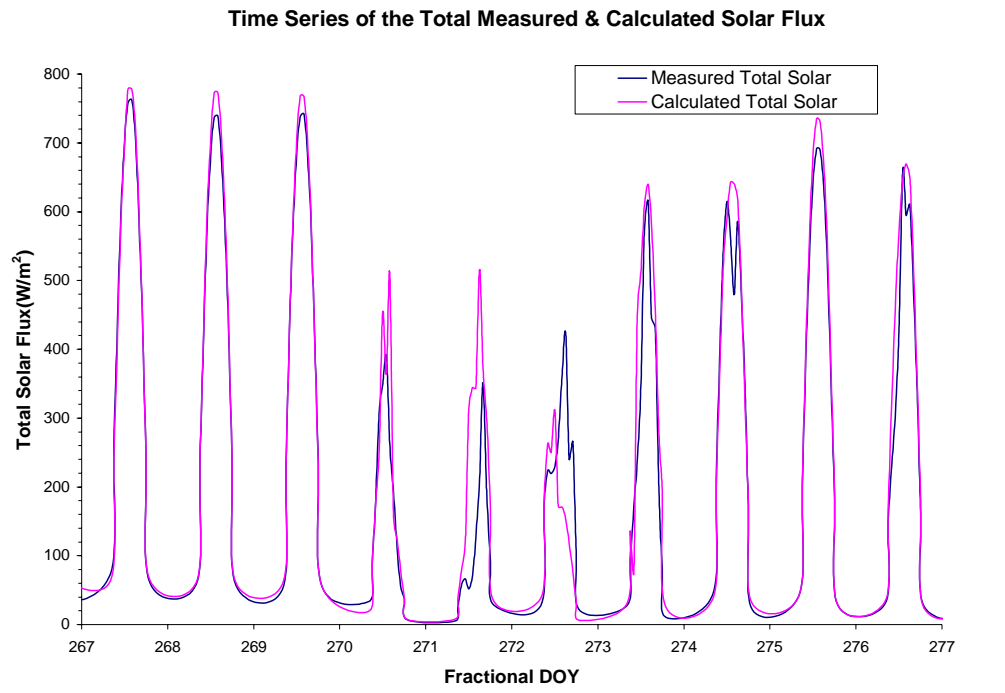


Figure 2.1 Comparison of the measured and calculated total solar flux for a 10-day period for Grayling I. Only the values of the solar flux when the zenith angle is less than 90 degrees are plotted.

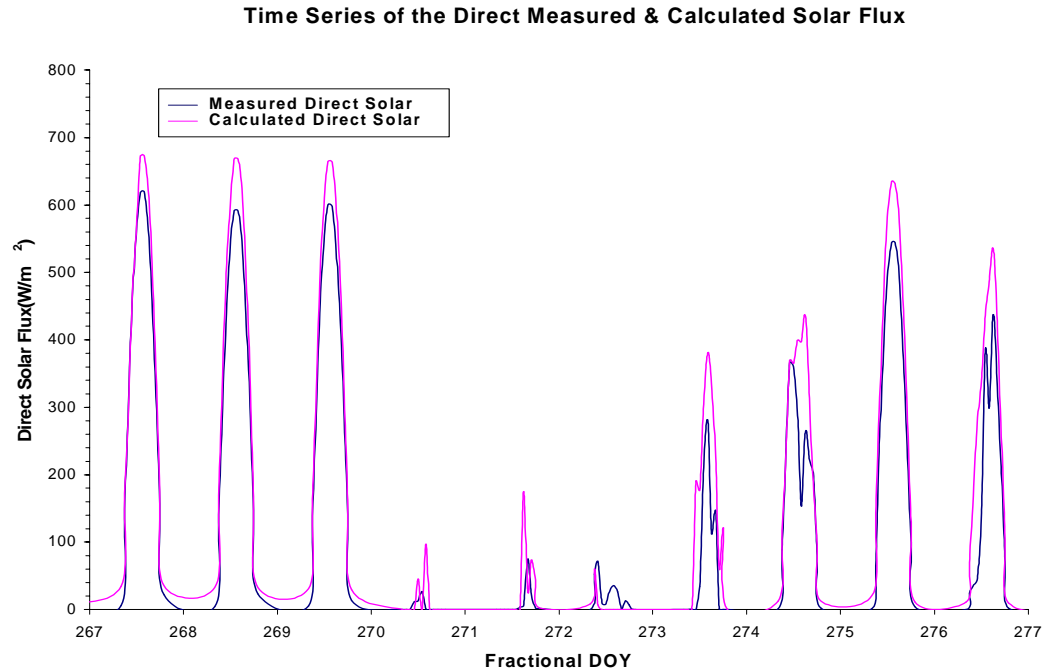


Figure 2.2 Same as Figure 2.1 but for the direct component of the solar flux.

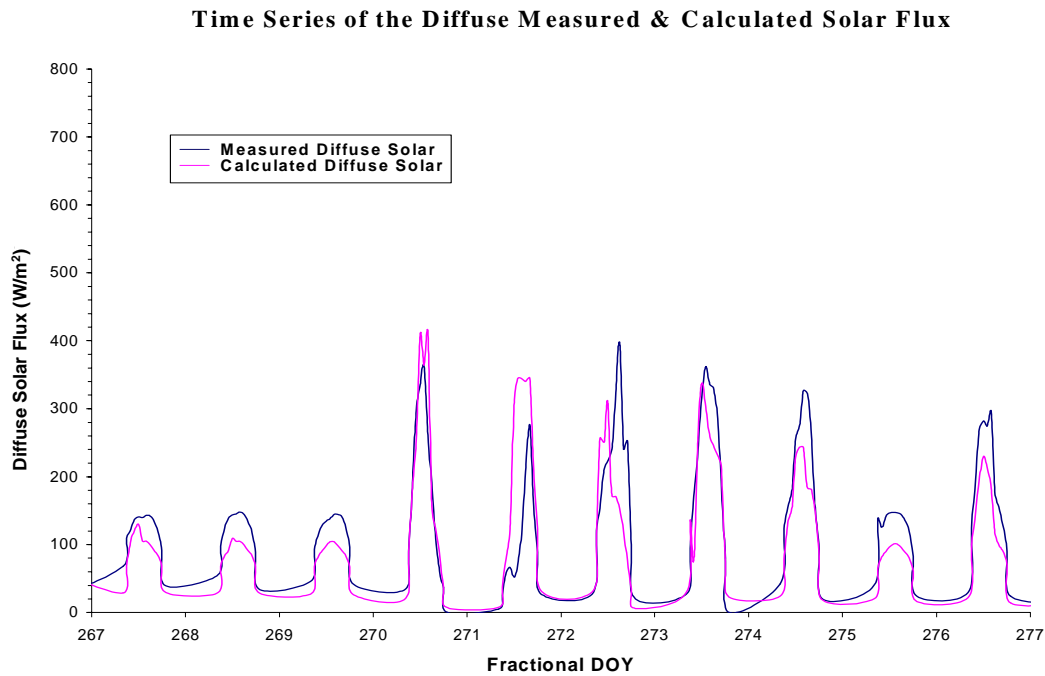


Figure 2.3 Same as Figure 2.1 but for the diffuse solar flux.

Most surface energy budget models, including FASST, utilize only the total solar flux. Figure 2.4 is a scatter diagram of the total measured and calculated solar flux. A least square fit to the data and its correlation coefficient, R^2 , is presented in the figure. The least square fit has been forced through the origin (0,0).

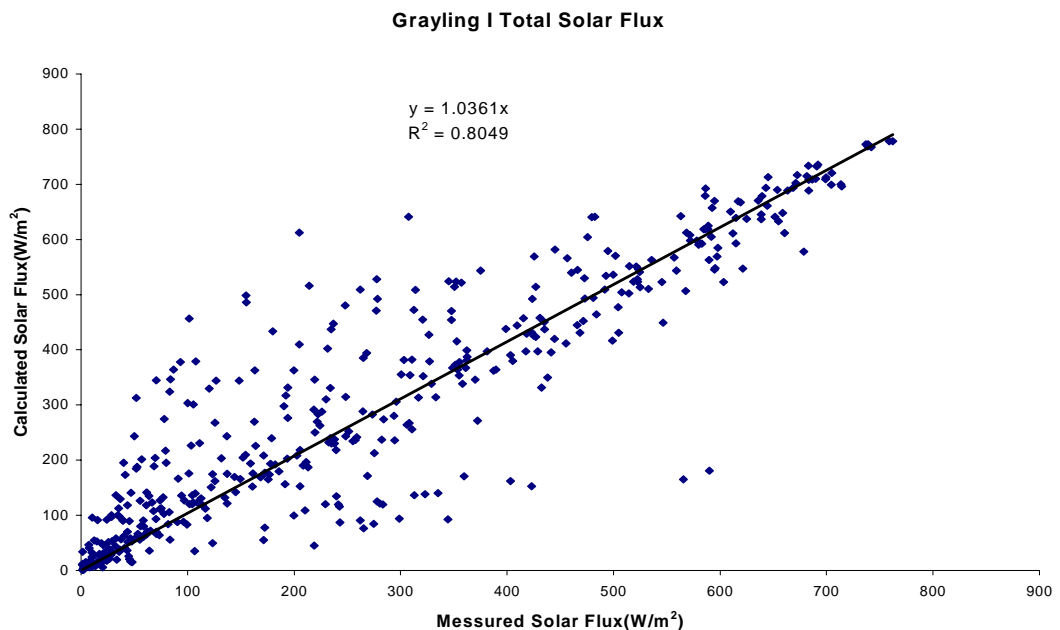


Figure 2.4 Scatter diagram of the total solar measured and calculated flux and the least square fit to the data.

The amount of scatter, relative to the least square fit, increases in the flux range from approximately 50 to 400 W/m^2 . Some of this scatter is no doubt due to the comparison of the average flux conditions with calculated fluxes based on the instantaneous observation of cloud amount on the hour. Table 2.6.1 presents the equation for the least square fit and its correlation coefficient for the total solar flux and each of the flux components.

Table 2.6.1 Equation of fit (forced through the origin) and correlation coefficient for Grayling I.

Solar Flux	Equation of Fit	R^2
Total	$y=1.0361x$	0.8049
Direct	$y=1.1353x$	0.8631
Diffuse	$y=0.8757x$	0.3752

The comparison of the diffuse components shows considerable amount of scatter as evident by the low correlation coefficient. There are a number of data points where the calculated is on the order of 100 to 200 W/m^2 greater than the measured value. This relatively large difference is due in part to inappropriate cloud representation. This includes both the cloud amounts and the implicit cloud optical depth as discussed earlier.

Figure 2.5 explores the impact of cloud conditions on the difference of the calculated total solar flux minus the total solar measured flux. Some interesting features are observed in Figure 2.5. The range of flux differences is smallest when there is no low cloud (clear, middle, high, or middle plus high). When there are only low clouds the differences are evenly distributed from -300 to $+300 W/m^2$. When there are low clouds plus another cloud type (low + middle, low + high, or low + middle + high), the calculated flux tends to be greater than the measured flux. The cloud optical depth is a function of the cloud thickness. The cloud model does not directly use cloud optical depth or cloud thickness. One of the reasons for this is that cloud thickness and cloud optical depth are not reported meteorological variables.

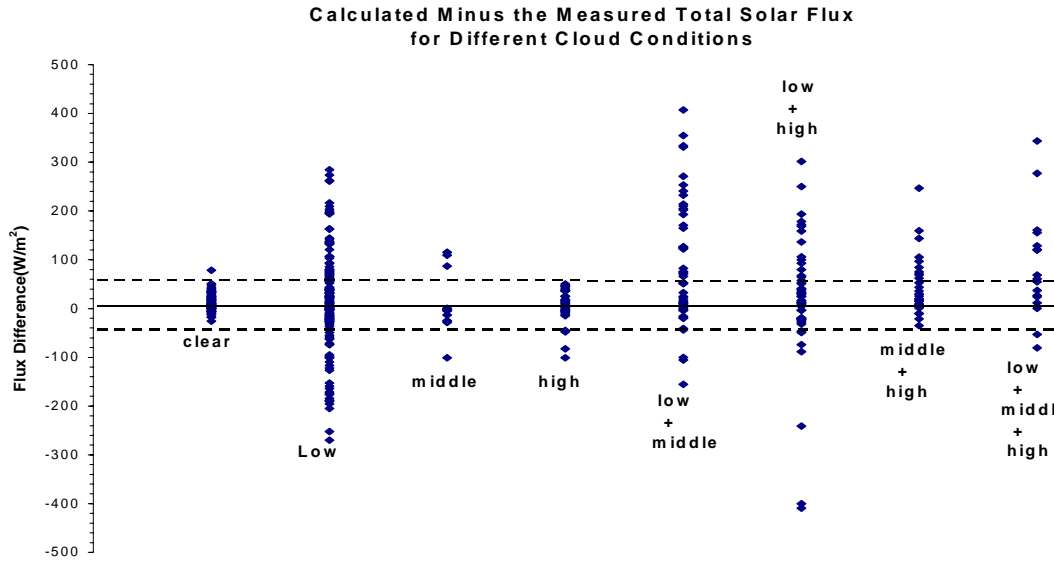


Figure 2.5 Calculated minus the measured total solar flux for different cloud conditions for Grayling I. The dashed lines are $\pm 50 \text{ W/m}^2$.

The analysis of the Yuma data indicates less scatter (Figure 2.6). This is anticipated, since there are fewer observations with clouds. Again, the correlation coefficient (Table 2.6.2) is lowest for the diffuse component of the solar flux. In general, the model performs better in the low cloud amount environment associated with the meteorological conditions at Yuma. The flux difference as a function of cloud conditions (Figure 2.7) again indicates that the model fluxes tend to be greater than the measured fluxes, even for clear conditions. Yuma is a very dry environment and a dust layer frequently developed by the end of the day as a result of the military traffic in the local training area. The model does not have a provision for handling the reduction of solar flux at the surface due to a dust layer.

Table 2.6.2 Equation of fit (forced through the origin) and correlation coefficient for Yuma.

Solar Flux	Equation of Fit	R^2
Total	$y=1.0656x$	0.9515
Direct	$y=1.0706x$	0.9023
Diffuse	$y=0.9708x$	0.6191

The analysis for Grayling II is presented in Figures 2.8 and 2.9 and Table 2.6.3. As with Grayling I, the correlation coefficients for the total, direct, and diffuse solar flux are less than the values for the Yuma analysis.

Table 2.6.3 Equation of fit (forced through the origin) and correlation coefficient for Grayling II.

Solar Flux	Equation of Fit	R^2
Total	$y=1.0395x$	0.8363
Direct	$y=0.98x$	0.8266
Diffuse	$y=1.1477x$	0.5471

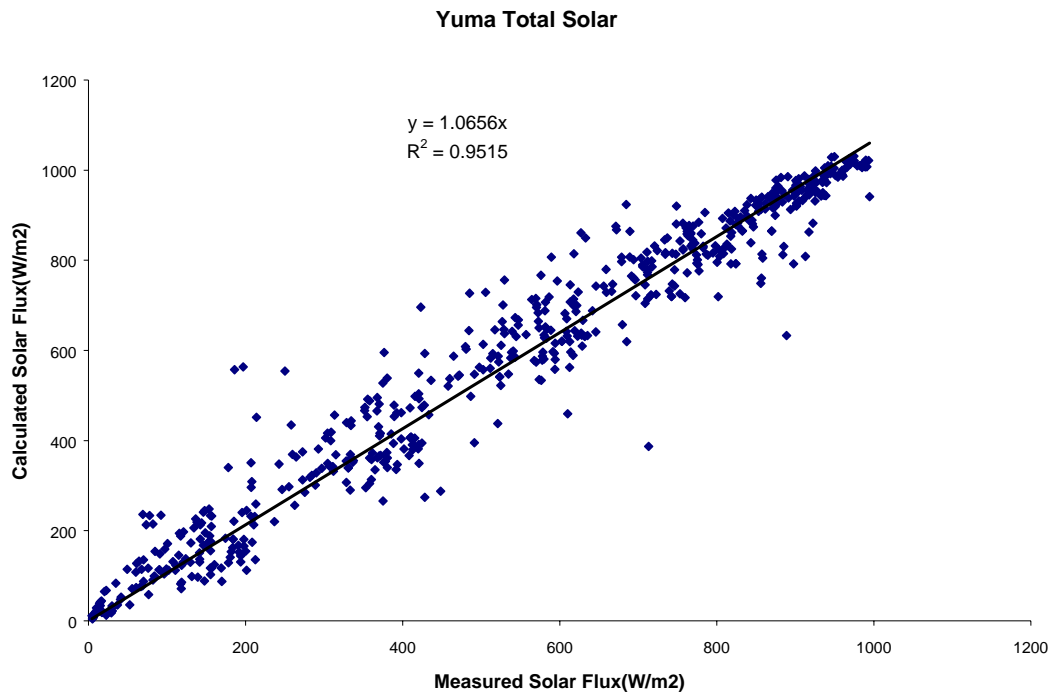


Figure 2.6 Scatter diagram of the total solar measured and calculated flux and the least square fit to the data.

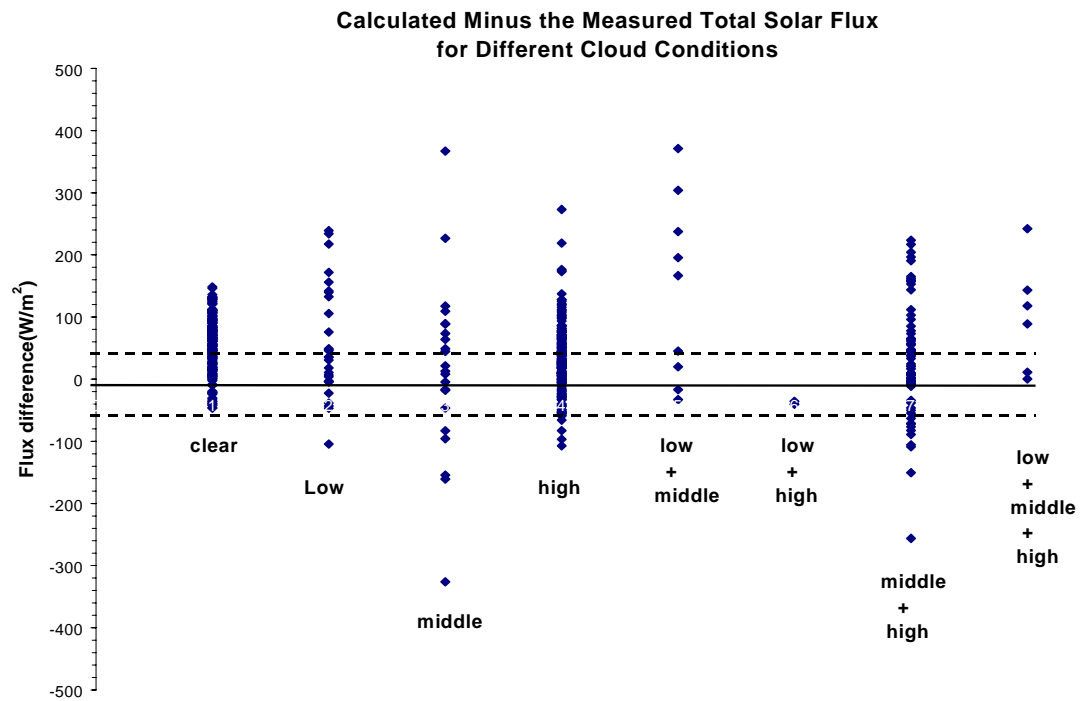


Figure 2.7 Calculated minus the measured total solar flux for different cloud conditions for Yuma. The dashed lines are $\pm 50 \text{ W/m}^2$.

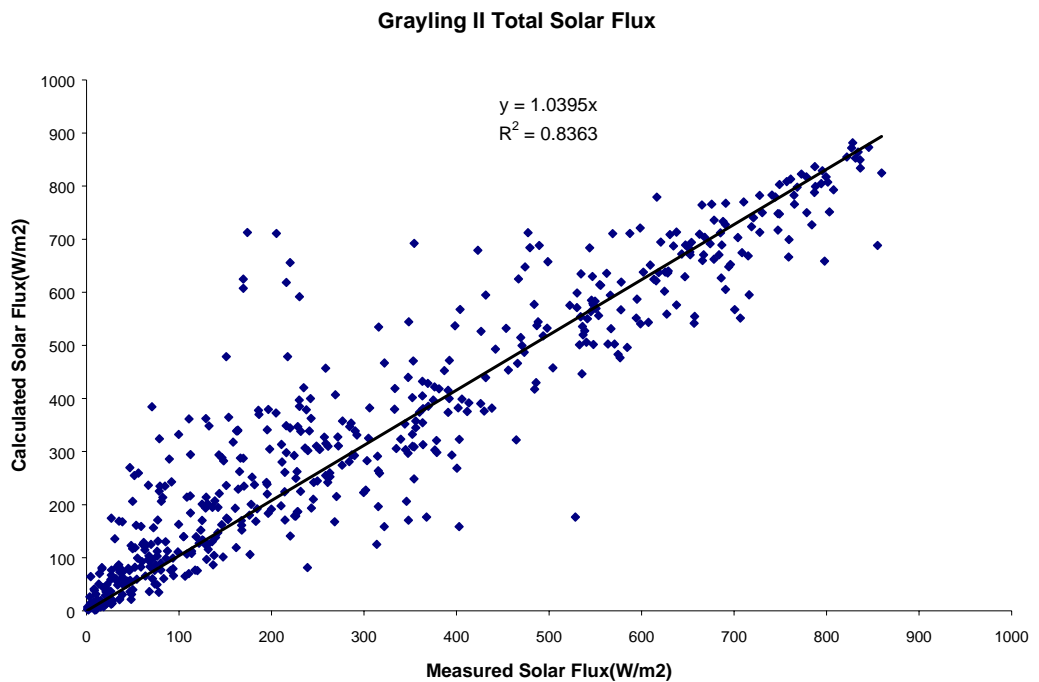


Figure 2.8 Scatter diagram of the total solar measured and calculated flux and the least square fit to the data.

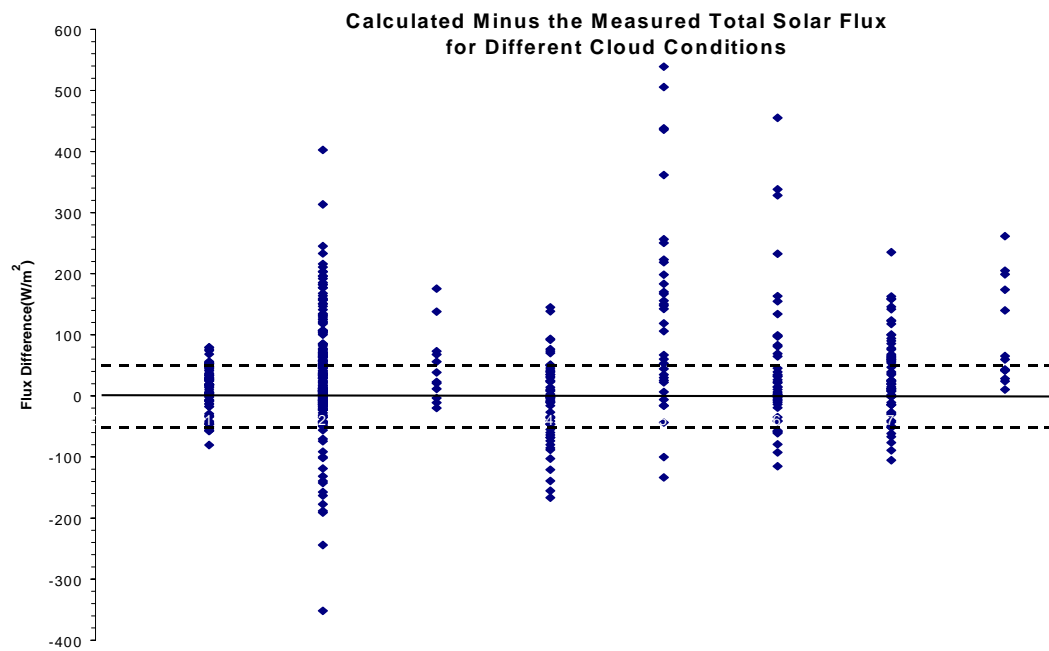


Figure 2.9 Calculated minus the measured total solar flux for different cloud conditions for Grayling II. The dashed lines are $\pm 50 W/m^2$.

2.7 Module Input and Output

The solar model inputs are

1. The latitude and longitude of the location.
2. The Day-Of-the-Year (DOY) and hour of the day.
3. The land surface category.
4. Low, middle, and high fractional cloud amount. If all three cloud amounts are missing, the low cloud amount is set equal to the global average cloud amount (0.54).
5. The low middle, and high cloud type. If missing, the model uses a set of default conditions. The low cloud default is cumulus, the middle cloud type is altostratus, and the high type is cirrus.

Items 1 and 2 are obtained from the meteorological data file, as are items 4 and 5 if they are available. Item 3 is found in the FASST input file.

The model outputs are the downwelling, reflected and net shortwave flux (W/m^2) at the surface for the input conditions. If the input conditions are representative of some time period, then the number of $Joules/m^2$ for that period is given as the flux (W/m^2) times the length of the period in seconds.

2.8 References

NOAA (1979) SOLMET Vol. 2: Hourly Solar Radiation-Surface Meteorological Observations, Final Report. D-9724, National Climatic Center, Asheville, NC.

Shapiro, R. (1972) Simple Model for the Calculation of the Flux of Solar Radiation through the Atmosphere, *Applied Optics*, V. 11, p. 760–764.

Shapiro, R. (1982) Solar Radiative Flux Calculations from Standard Surface Meteorological Observations. AFGL-TR-82-0039, Air Force Geophysics Laboratory, Hanscom AFB, MA.

Shapiro, R. (1987) A Simple Model for the Calculation of the Flux of Direct and Diffuse Solar Radiation Through the Atmosphere. AFGL-TR-0200, Air Force Geophysics Laboratory, Hanscom AFB, MA.

Chapter 3

Longwave (IR) Radiation Model

3.0 Introduction

The net longwave radiation at the surface is an important component of any surface energy budget model. Unfortunately, measurements of the net longwave radiation (upwelling longwave radiation and downwelling longwave radiation) are not readily available. Therefore, it is necessary to use parameters that are available and simple models to calculate the upwelling and downwelling longwave radiation at the surface. The net longwave radiation is a function of atmospheric conditions, especially cloud conditions, and the surface optical and physical properties.

3.1 Downwelling Longwave Radiation

One of the major components to the downwelling radiation at the surface is the atmosphere. Most of the downwelling atmospheric radiation originates in the lower atmosphere (below altitudes of several kilometers) where the absolute humidity is relatively high. The component ($I_{ir\downarrow}^{clr}$) for a clear sky is calculated from

$$I_{ir\downarrow}^{clr} = \varepsilon_a \sigma T_a^4 \quad (3.1)$$

where ε_a is the effective atmospheric emissivity, $T_a (K)$ is the ambient air temperature, and $\sigma (5.669 \times 10^{-8} \text{ W/m}^2 \cdot \text{K}^4)$ is the Stefan-Boltzmann constant. The effective atmospheric emissivity is calculated from Crawford et al. (1999)

$$\varepsilon_a = 1.24 * (e_a / T_a)^{(1/7)}. \quad (3.2)$$

e_a is the vapor pressure in millibars and can be found from

$$RH \approx 100 \frac{e_a}{e_{as}} \quad (3.3)$$

where RH is the relative humidity in percent and

$$e_{as} = e_{so} \exp \left[\frac{l}{R_v} \left(\frac{1}{T_o} - \frac{1}{T_a} \right) \right] \quad (3.4)$$

is the saturated vapor pressure. e_{so} is the saturated vapor pressure at standard conditions ($\approx 6.11 \text{ mbars}$), l is the temperature-dependent latent heat of condensation (sublimation), R_v is the gas constant for water vapor, and T_o is the standard temperature (273.15°C).

For cloudy skies the downwelling flux ($I_{ir\downarrow}^{cld}$) is given as

$$I_{ir\downarrow}^{cld} = c_l \chi_l + c_{eff}^m \chi_m + c_{eff}^h \chi_h \quad (3.5)$$

where c_l is the fractional low cloud amount, c_{eff}^m and c_{eff}^h are the effective middle and high cloud cover amounts based on the principle of random overlap, and $\chi_{(i,m,h)}$ is the cloud irradiance factor for low, middle, and high clouds, respectively. c_{eff}^m and c_{eff}^h are given as

$$c_{eff}^m = c_m(1 - c_l) \text{ and } c_{eff}^h = c_h(1 - c_m)(1 - c_l) \quad (3.6)$$

where c_m (c_h) are the fractional middle (high) cloud cover amounts. Hodges et al. (1983) originally defined $\chi_{(i,m,h)}$ as

$$\chi_{(i,m,h)} = 80 - 5Z_{(l,m,h)} \quad (3.7)$$

where $Z_{(l,m,h)}$ is either the low, middle, or high cloud base altitude in kilometers. Equation (3.7) has been modified based on the Geophysics Laboratory model atmospheres (tropics, mid latitude summer, mid-latitude winter, subarctic summer, and subarctic winter) and is given as

$$\chi_{(i,m,h)} = 94 - 5.8Z_{(l,m,h)} \quad (3.8)$$

The cloud base altitude, if not available from observations, has been parameterized in terms of season and latitude following the approach by Stowe et al. (1980) and London (1957) and data from the *Global Distribution of Total Cloud Cover and Cloud Type Amounts Over Land* (1986) prepared by DOE and NCAR (Table 3.1.0). The basic equation is given as

$$Z_{(l,m,h)} = a_{(l,m,h)} - b_{(l,m,h)} \{1 - \text{abs}[\cos(c_{(l,m,h)} \{\lambda - d_{(l,m,h)}\})]\} \quad (3.9)$$

where λ is the latitude and $a_{(l,m,h)}$, $b_{(l,m,h)}$, $c_{(l,m,h)}$ and $d_{(l,m,h)}$ are parameterization coefficients given in Table 3.1.0.

Table 3.1.0 Coefficients for determining cloud base altitude (*meters*) as a function of season, latitude, and cloud type.

Winter (Dec, Jan, and Feb)					
Cloud Type	Latitude	a	b	c	d
low	≥ 25	1050	600	1.5	25
low	< 25	1050	600	5.0	25
middle	≥ 25	4100	2000	1.7	25
middle	< 25	4100	300	4	25
high	all	7000	1500	3	30

Non-Winter (Mar, Apr, May, Jun, Jul, Aug, Sep, Oct, and Nov)					
Cloud Type	Latitude	a	b	c	d
low	≥ 25	1150	600	1.5	25
low	< 25	1150	450	5.0	25
middle	≥ 25	4400	1200	3.0	25
middle	< 25	4400	300	4	25
high	all	7000	1500	3	30

The total downwelling radiation is given as

$$I_{ir\downarrow} = I_{ir\downarrow}^{clr} + I_{ir\downarrow}^{cld} \quad (3.10)$$

3.1.1 Modification of the Cloud Irradiance Factor (CIF)

The total downwelling radiation at the ground, assuming a single optically thick overcast cloud layer, can be written as

$$I_{ir\downarrow} = \varepsilon_a \sigma T_a^4 + (80 - 5Z) \quad (3.11)$$

based on the original CIF (Z is the cloud base height). The total downwelling radiation can also be written as

$$I_{ir\downarrow} = \varepsilon_a \sigma T_a^4 + (1 - \varepsilon_a) \sigma T_c^4. \quad (3.12)$$

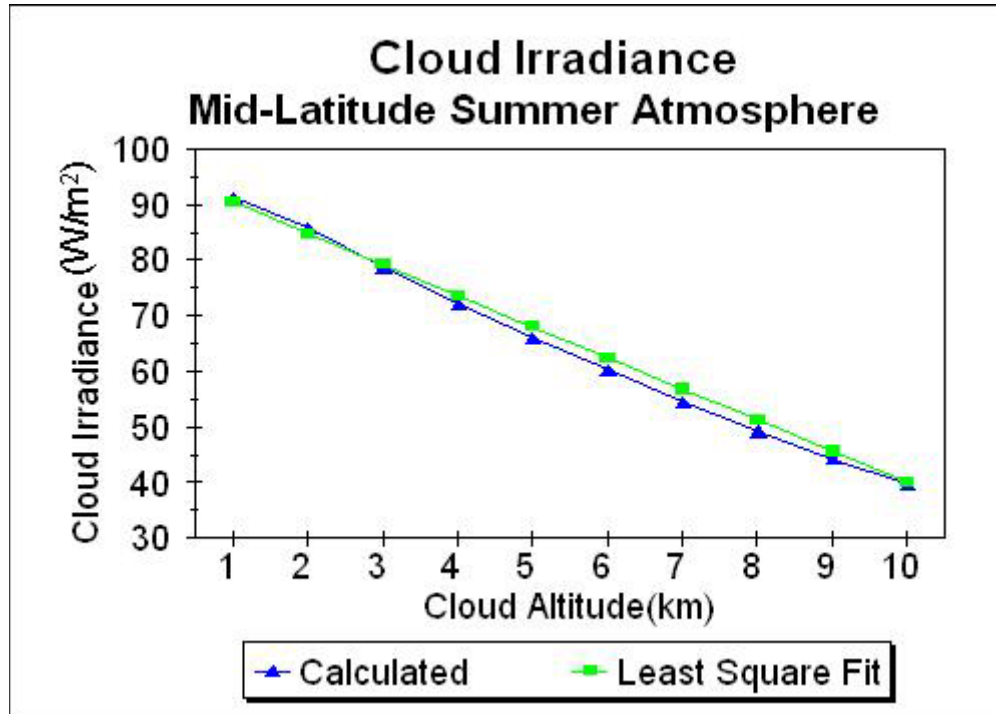


Figure 3.1 Calculated cloud irradiance in accordance with Equation (3.12) and the least square fit to the data points. Calculations are based on a mid-latitude summer atmosphere.

The term in parentheses is the atmospheric transmission below the cloud and T_c (K) is the cloud base temperature. The cloud emissivity is assumed to be one, implying the cloud reflection and transmission are zero. Using a cloud emissivity of one and the cloud base temperature (clouds radiate at a temperature slightly colder than the cloud base temperature) will result in an overestimation of the emitted cloud radiance. This is offset by the fact that the cloud reflection is assumed to be zero and therefore the cloud does not reflect downward any of the earth-emitted radiance. Equating Equations (3.11) and (3.12), we can re-derive the term in parentheses in Equation (3.11) by computing the cloud contribution to the total downwelling radiation using either measured moisture and atmospheric temperature profiles or the Geophysics Laboratory model atmospheres. The atmospheric emissivity was calculated using the Geophysics Laboratory model atmospheres and Equation (3.2) (and Equation [3.3] etc.). Next, the cloud radiance was

calculated for overcast optically thick clouds at altitudes from 1 *km* to 10 *km* for each of the Geophysics Laboratory model atmospheres. An example of the resulting calculations is given in Figure 3.1.

The results for all Geophysics Laboratory model atmospheres and the correlation coefficients are given in Table 3.1.1.

Table 3.1.1 Calculated regressions for determining the cloud irradiance for the Geophysics Laboratory Model Atmospheres.

<i>Atmosphere</i>	<i>Cloud Irradiance</i>	<i>Correlation coefficient</i>
Tropical	95-5.8Z	0.996
Mid-latitude Summer	96-5.8Z	0.997
Mid-latitude Winter	93-5.8Z	0.997
Subarctic Summer	95-5.9Z	0.998
Subarctic Winter	90-5.8Z	0.991

3.2 Downwelling Infrared Flux Model Validation

The Smart Weapons Operability Enhancement (SWE) field program data were used to evaluate the downwelling infrared flux model. The SWE field programs were conducted during the fall of 1992 (Grayling I-Grayling, MI), the winter/spring of 1994 (Grayling II-Grayling, MI), and the spring/summer of 1993 (Yuma, AZ). Each program ran for approximately 44 days and meteorological information was collected at several locations in a 2-*km*-square area with a temporal frequency of one minute. Hourly average values of the meteorological information were used to evaluate the downwelling infrared model. The hourly average values were computed using the one-minute values for a period of 30 minutes before and after the hour. The exception was the cloud amount information. During Grayling I, observations of the cloud cover were made on the hour from approximately 0700 to 1900 local. During the night, the cloud amounts were derived from ceilometer measurements. The hourly fractional cloud amount was computed from the number of one-minute ceilometer measurements that indicated clouds. The sixty observations were centered on the hour. Unfortunately, the ceilometer used to compute the nighttime cloud amounts was an older model that had an effective range of only several kilometers. It is highly unlikely that middle and high clouds ever entered into the calculation of the cloud amount. Figure 3.2 is a plot of the measured and computed downwelling longwave flux as a function of the fractional day of the year.

Grayling I Downwelling IR Flux Comparison

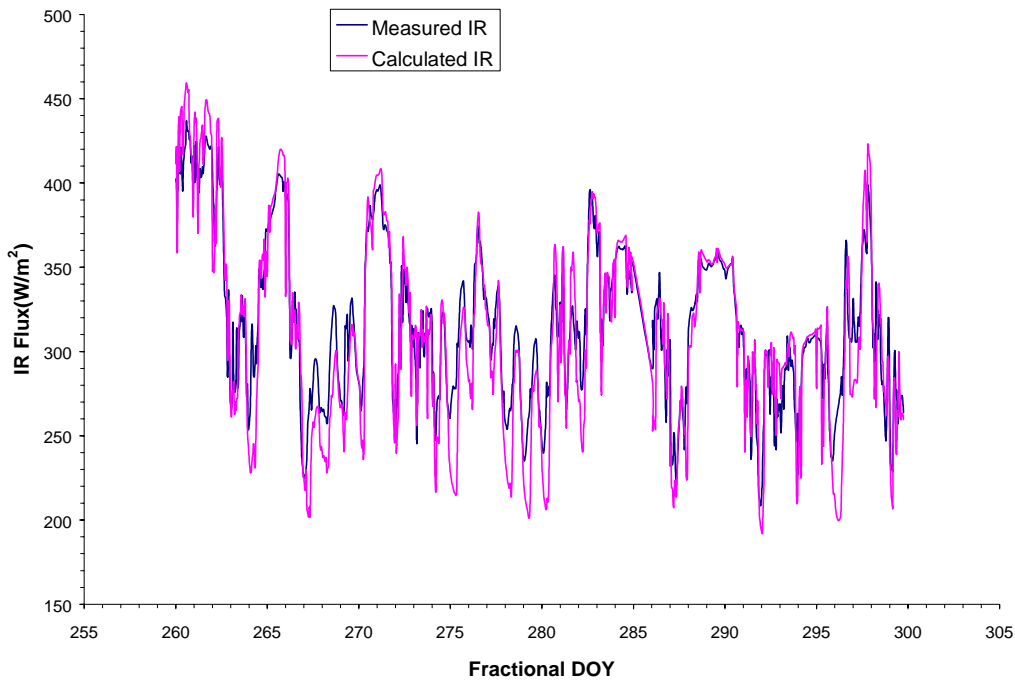


Figure 3.2 Comparison of the downwelling measured and computed longwave flux based on the Grayling I meteorological observations.

The comparison can also be presented as a scatter diagram (Figure 3.3). Also is the linear least square fit and the R^2 coefficient.

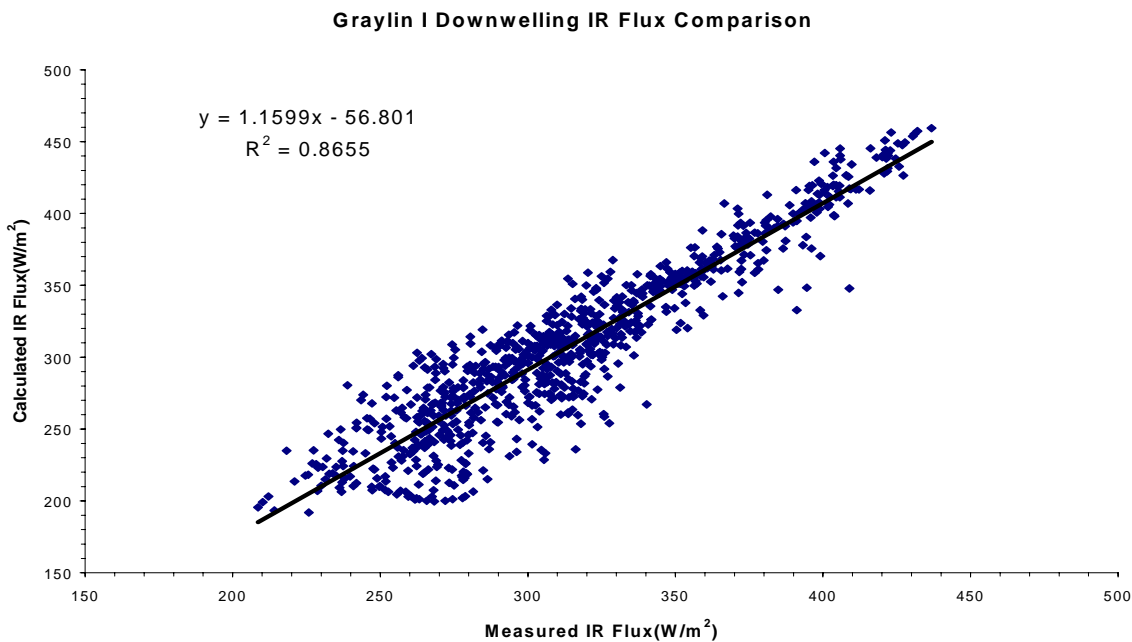


Figure 3.3 Comparison of the measured and model calculated downwelling longwave flux.

Some scatter is evident in Figure 3.3. All points where the difference between the measured and calculated downwelling fluxes was greater than 50 W/m^2 were investigated. Fifty-two points out of 932 points fell in this category. In every case, the measured flux was greater than the calculated. In 13 of these cases, the observer reported frost on the dome of the instrument during the morning inspection of the meteorological instruments. Of the 39 remaining cases, 24 occurred during periods of reduced visibility (fog or haze) and clear or scattered-cloud sky conditions. During periods of reduced visibility the sensor does not “see” the cold sky, but some temperature associated with the low atmosphere. The infrared model will not handle periods of reduced visibility effectively. Only two cases occurred during the day with no obscuration to the visibility and when an observer was on duty to take cloud observations. The average flux values for clear, scattered (0.1 to 0.5 cloud cover), broken (0.6 to 0.9 cloud cover), and overcast (1.0 cloud cover) are given in Table 3.2.1.

Table 3.2.1 Grayling I average downwelling IR flux for different cloud conditions.

Cloud amount	Measured IR	Calculated IR
clear	284.6	257.3
Scattered (0.1 to 0.5 cloud cover)	293.3	282.3
Broken (0.5 to 0.9 cloud cover)	331.9	336.3
Overcast (1.0 Cloud cover)	349.8	359.2

A similar analysis of the Yuma data is presented in Figures 3.4 and 3.5.

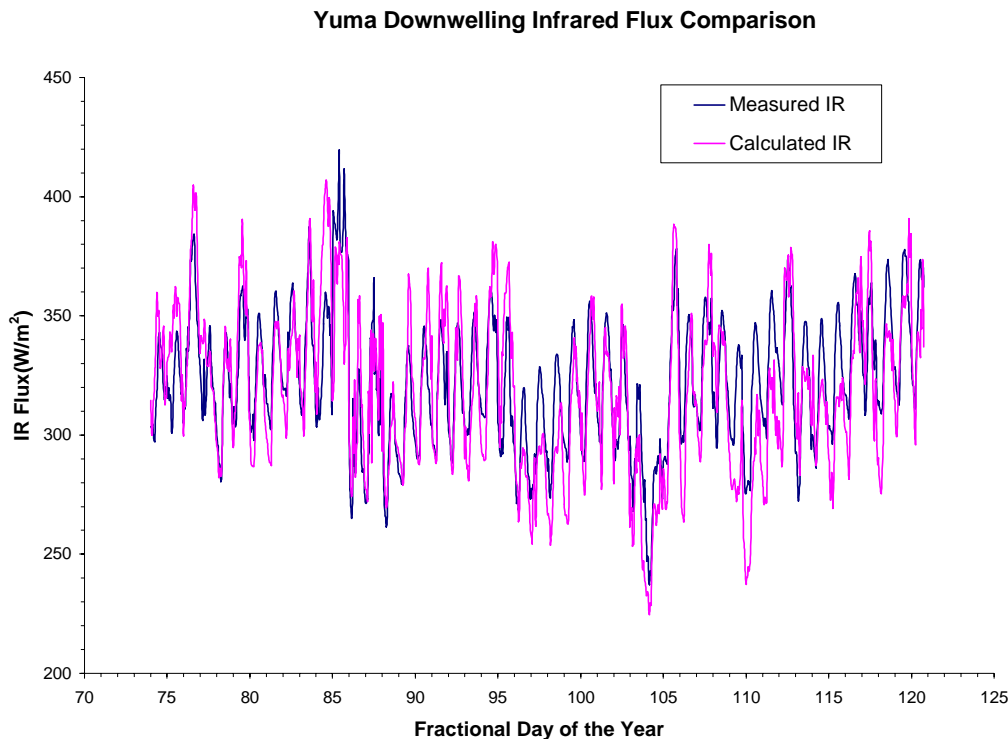


Figure 3.4 Comparison of the downwelling measured and computed longwave flux based on the Yuma meteorological observations.

Yuma Downwelling Infrared Flux Comparison

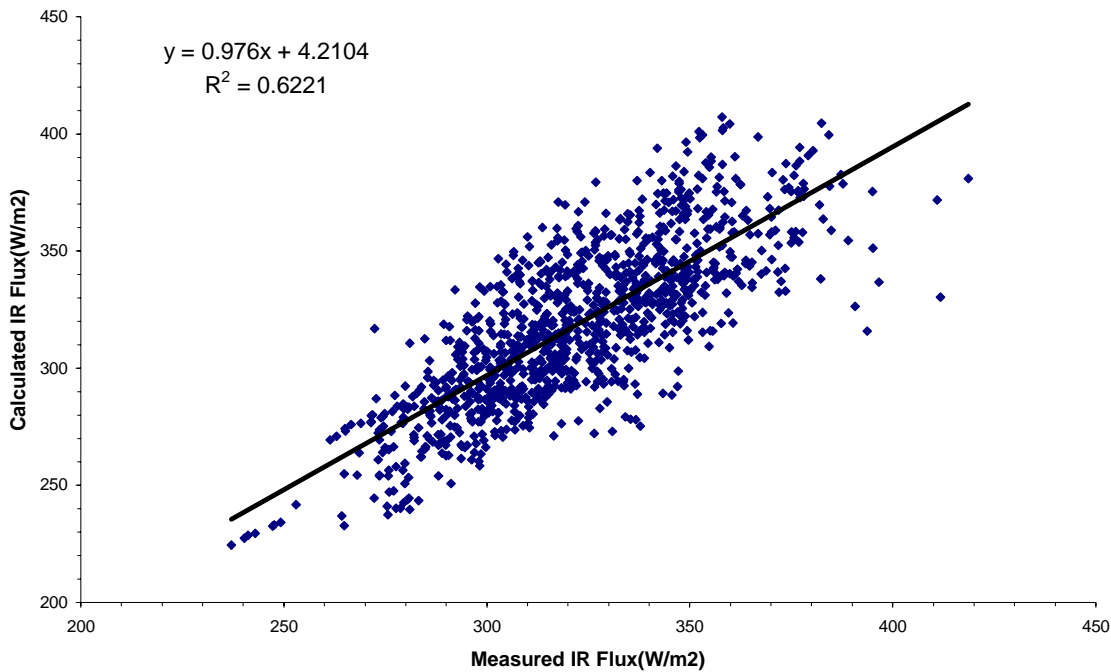


Figure 3.5 Comparison of the measured and model calculated downwelling longwave flux.

There is considerable spread in the data resulting in a relatively low R^2 . During the field program, daytime temperatures were as high as 31°C with relative humidity as low as 3 percent. Out of 1124 observations, a difference of 50 W/m^2 or greater between the measured value and the corresponding calculated occurred only seventeen times. For four of the seventeen cases the calculated flux was greater than the measured flux. In every one of these cases, eight tenths or more of thin cirrus was reported. Two cirrus regimes invaded this area: mid-latitude cirrus and cirrus associated with a subtropical jet stream. Cirrus associated with the subtropical jet usually consists of smaller ice crystals. In addition, the base of the cirrus normally occurs at a higher altitude than mid-latitude cirrus (based on LIDAR and aircraft observations taken during the First ISCCP Regional Experiments [FIRE] program at Coffeeville, KS). Thin cirrus (meteorologically, thin cirrus is defined as cirrus that is transparent enough that blue sky can be observed) will have an emissivity that is less than optically thick cirrus. Paltridge and Platt (1981) reported cirrus emittance as a function of Ice Water Path (IWP). Emittance values range from 0.1 for IWPs of approximately 10 g/m^2 to 0.9 for IWPs of 60 g/m^2 . The model implicitly assumes an emissivity of one for all clouds. The calculated base of the clouds was on the order of seven kilometers. Using an emissivity (0.5 rather than 1.0) and cloud base altitude (10 km rather than 7 km) that is more characteristic of thin subtropical jet stream cirrus, the contribution to the flux at the surface is reduced by approximately 36 W/m^2 . Six of the observations that exceeded the 50 W/m^2 criteria occurred when the relative humidity was 5 percent or less and the temperature was approximately 30°C . It is

not known whether the parameterization of the atmospheric emissivity can effectively handle these extreme conditions. In addition, the computed downwelling infrared flux is fairly sensitive to the low cloud amount as anticipated. For example, a change of 0.1 in the cloud amount for a cloud at one kilometer will result in a change of approximately 90 W/m^2 in the downwelling flux. The average flux values for clear, scattered (0.1 to 0.5 cloud cover), broken (0.6 to 0.9 cloud cover), and overcast (1.0 cloud cover) are given in Table 3.2.2.

Table 3.2.2 Yuma average downwelling IR flux for different cloud conditions.

Cloud amount	Measured IR	Calculated IR
Clear	311.7	296.40
Scattered (0.1 to 0.5 cloud cover)	328.7	332.33
Broken (0.5 to 0.9 cloud cover)	369.2	373.10
Overcast (1.0 Cloud cover)	348.7	370.40

Grayling II was a winter field program. Fog, including ice fog, and very low surface temperatures (-20°C) will tax the ability of the model to accurately predict the downwelling infrared flux. The comparison of the measured and the calculated flux is presented in the following figures and table.

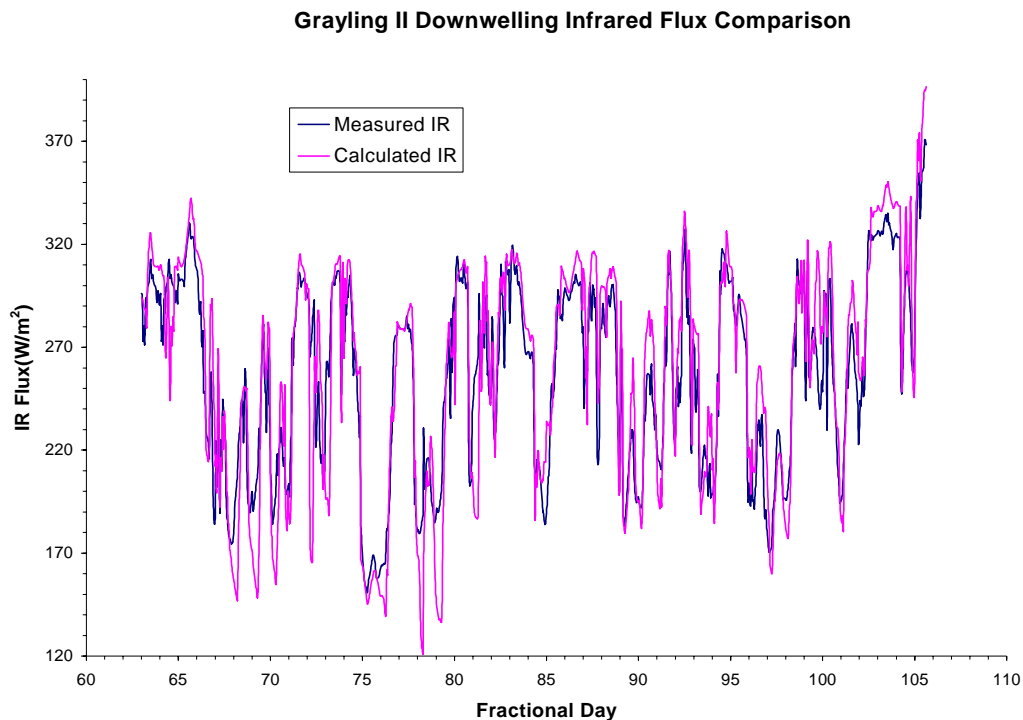


Figure 3.6 Comparison of the downwelling measured and computed longwave flux based on the Grayling II meteorological observations.

Grayling II Downwelling Infrared Flux Comparison

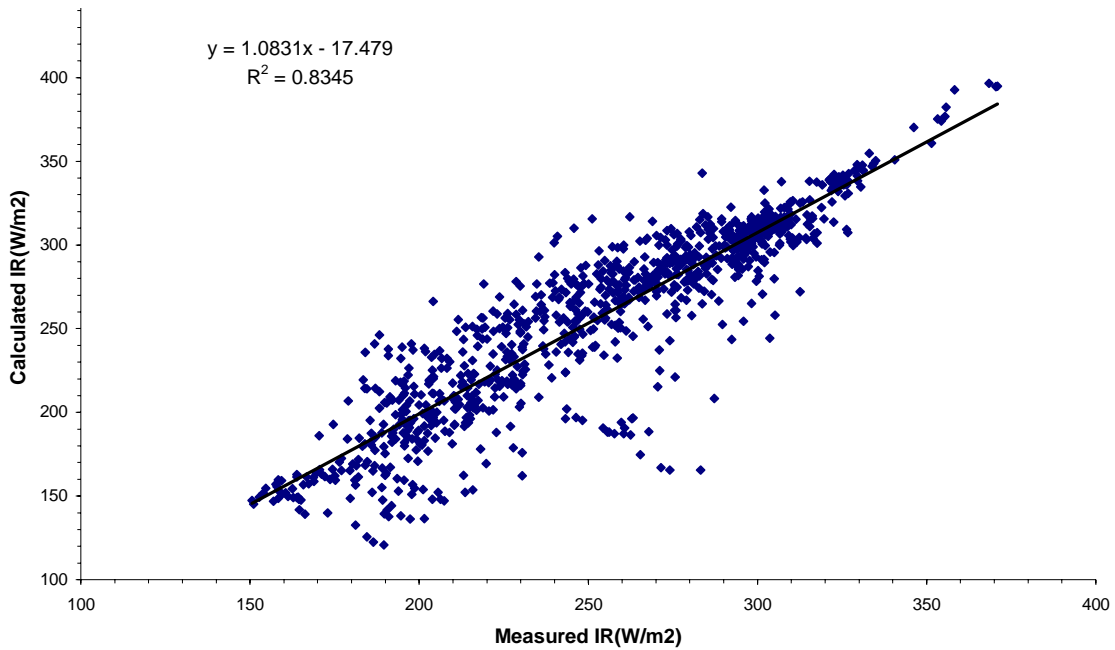


Figure 3.7 Comparison of the measured and model calculated downwelling longwave flux.

Four percent (49 out of 1024) of the calculated flux values differed by more than 50 W/m^2 from the corresponding measured values. In 25 of the 49 cases, either ice/snow was reported on the dome of the instrument or fog with visibilities on the order of 2 km was reported. R^2 increases to 0.89 if these cases are removed from the database. As indicated, the model can not handle the impact of fog on the downwelling infrared flux. In addition, surface temperatures on the order of $-20 \text{ }^{\circ}\text{C}$ were reported in seventeen of the comparisons. It is doubtful that the model will predict the correct cloud base temperature, especially the cloud base temperature of low clouds, under these conditions. Usually, in a winter environment when the surface temperature is very low, there is a strong inversion. Not only will the calculation of the cloud base temperature be affected by the presence of an inversion, but the calculation of the atmospheric emissivity will also be affected.

Table 3.2.3 Grayling II average downwelling IR flux for different cloud conditions.

Cloud amount	Measured IR	Calculated IR
clear	203.9	182.1
scattered (0.1 to 0.5 cloud cover)	222.1	225.0
broken (0.5 to 0.9 cloud cover)	257.5	269.9
overcast (1.0 Cloud cover)	289.2	301.5

3.3 Potential Modification

As indicated above, there are no provisions for handling inversions and optically thin clouds. With this in mind, it is feasible to recast the formulation of the cloud radiance and the attenuation of the cloud-emitted radiance in terms of parameters that would be readily available. It should be remembered that the proposed approach is only a surrogate for a more complete representation of cloud and atmospheric processes that account for the downwelling radiance at the surface. To accurately model these more complicated processes, it is necessary to have atmospheric profiles of temperature and moisture plus profiles of the cloud optical properties, parameters that are not readily available. The proposed model is based on the following assumptions:

1. Low and middle clouds are optically thick. This implies the cloud emissivity is one, while the cloud reflection and transmission are zero. It also implies that clouds radiate at the cloud base temperature. This assumption is not true for ice clouds and some of the thinner stratus type clouds found over ocean areas. Ice clouds, because of their relatively cold temperatures, do not contribute significant amounts of downwelling radiance. For high clouds (ice clouds), an emissivity of less than one would be used.
2. The lower atmosphere contributes the greatest amount of clear sky radiance and causes the greatest amount of attenuation of the cloud-emitted radiance. This implies that an effective atmospheric emissivity can be computed from the ambient relative humidity (or vapor pressure).
3. Cloud overlap, for multi-layered cloud systems, is governed by the principle of random overlap. In reality the dynamic atmospheric processes most likely govern the overlap. If the dynamic processes are synoptic scale in nature, they influence the atmosphere from the surface to the tropopause and above. In this case, the multi-layered clouds are most likely correlated.

The general equation for the downwelling radiation can be given as

$$I_{ir\downarrow} = \varepsilon_a \sigma T_a + (1 - \varepsilon_a) c_l \sigma T_{cl} + (1 - \varepsilon_a) c_{eff}^m \sigma T_{cm} + (1 - \varepsilon_a) c_{eff}^h \sigma T_{ch}. \quad (3.13)$$

The effective atmospheric emissivity and effective middle and high cloud cover are calculated as indicated above. The cloud radiating temperature is calculated as follows:

$$T_{c(l,m,h)} = T_a + \Gamma(lat, season, z)Z \quad (3.14)$$

where $\Gamma(lat, season, z)$ is the integrated atmospheric lapse rate and is a function of station location (latitude), season, and cloud base altitude. The lapse rate can be obtained from the Geophysics Laboratory model atmospheres or from the Atmospheric Circulation Statistics model atmospheres of Oort and Rasmusson (1971). The Geophysics Laboratory model atmospheres is stratified into three latitude zones and two seasons, while the Atmospheric Circulation Statistics model atmospheres is stratified by month and five degree latitude bands. For each latitude zone and each time period, the integrated lapse rate could be computed for the altitude range 0–1 km, 0–2 km, 0–3 km, and 0–10 km. In addition, the atmospheric profile could be adjusted in the lower levels of the atmosphere to be consistent with the observed ambient temperature and humidity. The cloud height, if not available from observations, can be specified in a physically consistent manner with the model vertical temperature profiles.

The impact of fog or haze on the downwelling infrared flux would be parameterized using MODTRAN (MODerate resolution TRANsmision) and tied to the visibility and the cause of the restricted visibility, parameters reported on standard meteorological observations. MODTRAN is the Department of Defense's standard atmospheric IR/VIS/UV radiance and transmission band model for lower altitudes.

3.4 Upwelling Longwave Radiation

The upwelling radiance can be specified in terms of the surface temperature, downwelling radiance, and the surface emissivity (ε_g). If the surface temperature is not available it may be necessary to assume the surface temperature is approximately equal to the ambient temperature. In addition, the surface emissivity is parameterized in terms of the land cover. The values of the land cover emissivities can be obtained from the literature. Assuming land cover (or land use) category is available from GIS information. The upwelling radiance is given as

$$I_{ir\uparrow} = \varepsilon_g \sigma T_g^4 + (1 - \varepsilon_g) I_{ir\downarrow}. \quad (3.15)$$

3.5 Model Input and Output

The model inputs are

1. The latitude of the location.
2. The Day-Of-the-Year (DOY) and hour of the day for the model calculations.
3. The land surface category. The land surface categories currently modeled are grass, all USCS soil types, and snow. It is assumed that the land category is input by the user.
4. Ambient (air) temperature. The model will not run unless this parameter is provided.
5. Relative Humidity. If this is missing the model assumes a value of 60%.
6. Surface Temperature. If the surface temperature is missing, it is set equal to the air temperature. For daily average conditions this assumption is not that bad since at times during the day the surface temperature is greater than the air temperature while at other times it is less than the air temperature.
7. Low, middle, and high fractional cloud amount. If all three cloud amounts are missing, the low cloud amount is set equal to the global average cloud amount of 0.5.
8. Low, middle, and high cloud type. If the cloud type information is missing and the cloud amount is not zero, a cloud type is assigned based on climatological averages.
9. Low, middle, and high cloud height. If the cloud base altitude is missing and the cloud amount is not zero, a cloud-base altitude is calculated based on the cloud type, location (latitude), DOY, and climatological information.

The model outputs are the downwelling, upwelling, and net longwave radiation (W/m^2) at the surface for the input conditions. If the input conditions are representative of some time period, then the number of $Joules/m^2$ for that period is given as the flux (W/m^2) times the length of the period in seconds.

3.6 References

Carslaw, H.S., and J.C. Jaeger (1959) *Conduction of Heat in Solids*, Oxford: Clarendon Press.

Carslaw, H.S., and J.C. Jaeger (1973) *Conduction of Heat in Solids, Second Edition*, Oxford: Clarendon Press.

Chapman, A.J. (1984) *Heat Conduction, Fourth Edition*, New York: Macmillan Publishing.

Crawford, T.M., and C.E. Duchon (1999) An Improved Parameterization for Estimating Effective Atmospheric Emissivity for Use in Calculating Daytime Downwelling Longwave Radiation. *Journal of Applied Meteorology*, V. 18, p. 474–480.

Hodges, D.B., G.J. Higgins, P.F. Hilton, R. Shapiro, C.N. Touart, and R.F. Wachtmann (1983) Final Tactical Decision Aid (FTDA) for Infrared 8–12 Micron Systems—Technical Backgrounds. Systems and Applied Sciences Corporation, Scientific Report No. 5, Air Force Geophysics Laboratory Rep. AFGL-TR-83-0022.

Ingersoll, L.R., O.J. Zobel, and A.C. Ingersoll (1954). *Heat Conduction with Engineering, Geological, and Other Applications*, Madison: University of Wisconsin Press.

London, J. (1957) A Study of the Atmospheric Heat Balance, Final Report. Contract AF19(122)-165 (AFCRC-TR-57-287), New York University {ASTIN 117227}, 99 p.

Oort, A.H., and E.M. Rasmusson (1971) Atmospheric Circulation Statistics. NOAA Professional Paper 5, DOC c55.25:5, U.S. Department of Commerce, 323 p.

Paltridge, G.W., and C.M. Platt (1981) Aircraft Measurements of Solar and Infrared Radiation and the Microphysics of Cirrus Clouds. *Quarterly Journal of the Royal Meteorological Society*, V. 107, p. 155–175.

Shapiro, R. (1972) Simple Model for the Calculation of the Flux of Solar Radiation Through the Atmosphere. *Applied Optics*, V.11, p. 760–764.

Shapiro, R. (1982) Solar Radiative Flux Calculations from Standard Surface Meteorological Observations. AFGL-TR-82-0039, Air Force Geophysics Laboratory, Hanscom AFB, MA.

Shapiro, R. (1987) A Simple Model for the Calculation of the Flux of Direct and Diffuse Solar Radiation Through the Atmosphere. AFGL-TR-0200, Air Force Geophysics Laboratory, Hanscom AFB, MA.

Stowe, L.L., H. Jacobowitz, and V.R. Taylor (1980) Reflectance Characteristics of Earth and Cloud Surfaces as Measured by the ERB Scanning Channels on the Nimbus-7

Satellite. *Proceedings, International Radiation Symposium*, Colorado State University, Fort Collins, CO, p. 430–432.

Chapter 4

Soil Temperature Model

4.0 Introduction

The soil temperature at the current time step is a function of the past soil temperature, soil moisture state, and the surface forcing. The latter depends on the time of day, wind, relative humidity, precipitation, air temperature, and presence of clouds.

4.1 Soil Thermal Model

The temperature gradient in a non-uniform soil layer can be described by the one-dimensional heat flow equation:

$$\begin{aligned}\frac{\partial T}{\partial t} &= \frac{\partial}{\partial z} \left(k_{th} \frac{\partial T}{\partial z} \right) - v \frac{c_{p,w}}{c_p} \frac{\partial T}{\partial z} + \frac{l_{fus}}{c_p \rho_w} \frac{\rho_i}{\rho_w} \frac{\partial \theta_i}{\partial t} \\ &= \frac{\partial k_{th}}{\partial z} \frac{\partial T}{\partial z} + k_{th} \frac{\partial^2 T}{\partial z^2} - v \frac{c_{p,w}}{c_p} \frac{\partial T}{\partial z} + \frac{l_{fus}}{c_p \rho_w} \frac{\rho_i}{\rho_w} \frac{\partial \theta_i}{\partial t}\end{aligned}\quad (4.1)$$

where T is the temperature (K), t is time (s), k_{th} is the thermal diffusivity (m^2/s), $c_{p,w}$ is the specific heat of water ($J/kg \cdot K$), c_p is the specific heat of the soil ($J/kg \cdot K$), v is the vertical rate of water flow (m/s), l_{fus} is the latent heat of fusion (J/kg), θ_i is the volumetric ice content (cm^3/cm^3), ρ_i is the density of ice (kg/m^3), ρ_w is the density of water (kg/m^3), and z is depth (m) measured positive downward from the surface. Further discussions on the water flow rate and the change in ice content are found in Chapter 5 and Chapter 6, respectively. The temperature is subject to the following boundary condition:

$$\begin{aligned}F(T) &= (1-\alpha)I_s \downarrow + I_{ir}^\downarrow - I_{ir}^\uparrow + H + L - P + \\ &\quad \kappa \frac{\partial T}{\partial z} + l_{fus} \frac{\rho_i}{\rho_w} \frac{\partial \theta_i}{\partial t} \Delta z - v c_p T = 0\end{aligned}\quad @ z = 0m \quad (4.2)$$

where α is the surface albedo, $I_s \downarrow$ is the total solar radiation (W/m^2) impinging on the surface, I_{ir}^\downarrow is the incoming longwave radiation (W/m^2), I_{ir}^\uparrow is the outgoing longwave radiation (W/m^2) both reflected and emitted, H is the sensible heat (W/m^2), L is the latent heat (W/m^2), P is the heat due to precipitation (W/m^2), and κ is the surface thermal conductivity ($W/m \cdot K$). In Equation (4.2), heat that is transferred to the surface is considered positive, as is shown in Figure 4.1. Energy that can be transferred either to/from the surface depending on the gradient is shown as double-headed arrows.

The first term in Equation (4.2) represents the amount of solar, or shortwave radiation, absorbed by the surface. The second term is the incoming longwave radiation while the third term is the outgoing longwave radiation, which is composed of radiation emitted from the surface and incoming radiation reflected from the surface. The sensible and latent heat fluxes together are called the turbulent heat fluxes and have non-zero values in

the presence of wind. The precipitation heat represents the energy needed to cool or heat any snow or rain that falls on the surface. The first term in the second row of Equation (4.2) takes care of heat conduction to/from the surface by the underlying ground depending on the temperature gradient. This is followed by the heat released/absorbed by the soil as the soil moisture melts/freezes. Finally, the last term represents heat that is advected away/towards the surface as a result of the vertical movement of moisture.

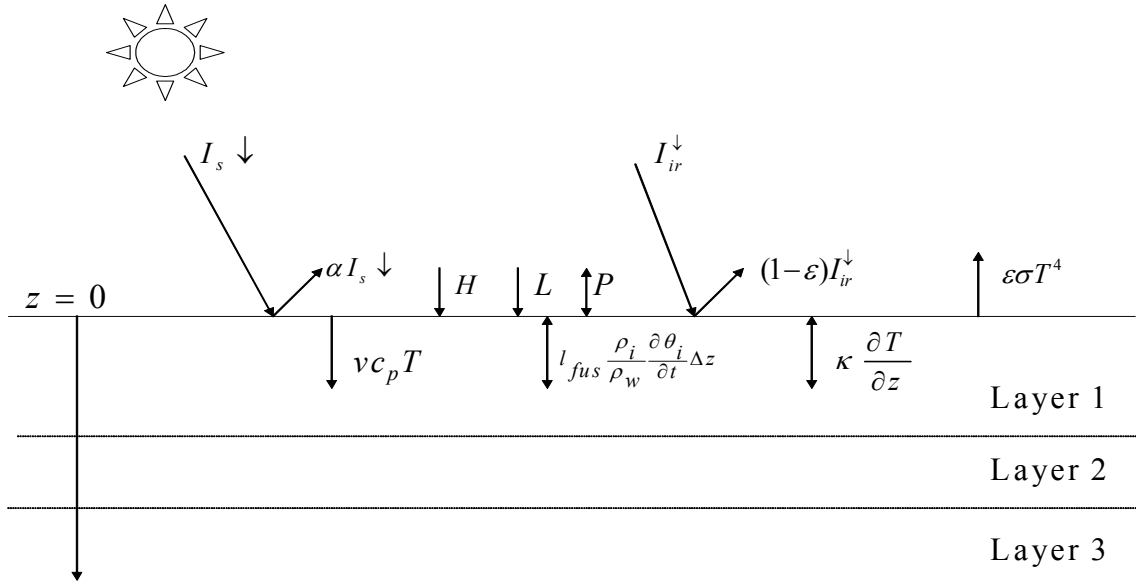


Figure 4.1 Surface Energy Balance.

4.1.1 Solar Radiation

Both diffuse ($I_s \downarrow^{dif}$) and direct ($I_s \downarrow^{dir}$) solar radiation comprise $I_s \downarrow$ such that $I_s \downarrow = I_s \downarrow^{dir} + I_s \downarrow^{dif}$. Since most surfaces are not horizontal, the effect of slope on the amount of solar radiation that impacts a site must be taken into consideration. The position of the sun is determined by the solar zenith angle, φ_o , and the solar azimuth angle, ϑ_0 as measured clockwise from North to its horizontal projection. Similarly, the slope is defined by φ , the zenith (elevation) angle of the surface as measured in the positive direction upwards from the horizontal and ϑ , the azimuth or aspect angle measured positive clockwise from North to its horizontal projection. Refer to Figure 4.2 for clarification. Following the work of Jordan (1991) and Shapiro (1978) the following correction is applied during daylight hours, i.e., $\varphi_0 < 90^\circ$,

$$\begin{aligned}
I_s \downarrow_{slope} &= I_s \downarrow^{dir} \left[\cos \varphi + \frac{\sin \varphi_0 \sin \varphi \cos \Delta \vartheta}{\cos \varphi_0} \right] + \\
I_s \downarrow^{dif} & \frac{(\pi - \Delta \vartheta)(S_c + \cos \varphi) + \Delta \vartheta(1 + S_c \cos \varphi)}{\pi(1 + S_c)} + I_s \downarrow \frac{\alpha(1 - \cos \varphi)}{2}
\end{aligned} \tag{4.3}$$

where all angles are in radians and $\Delta \vartheta \equiv |\vartheta - \vartheta_0|$ and $S_c = 1.0 + 0.5 \sin \varphi_0 + 2.0 \sin(2\varphi_0)$ is the ratio of the average diffuse radiance from the solar and anti-solar quadruplespheres (Jordan 1991). The last term in Equation (4.3) represents solar radiation reflected back onto the surface due to the slope.

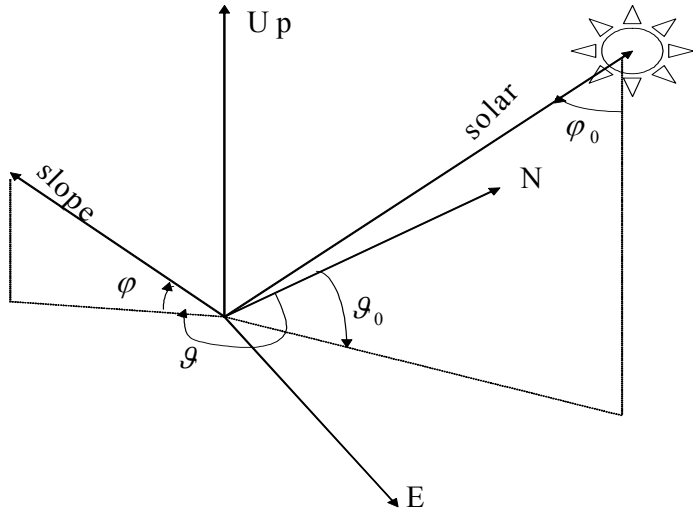


Figure 4.2 Sloped Solar Radiation Geometry.

4.1.2 Longwave Radiation

All objects radiate energy over the entire spectrum proportional to their surface properties and temperature according to the Planck's function, $I_{ir,emit}^{\uparrow} = \varepsilon \sigma T^4$ where, ε is the broad band surface emissivity, $T (K)$ is the surface temperature, and σ is the Stefan-Boltzmann constant ($5.669e-08 \text{ W/m}^2 \text{ K}^4$). The incoming longwave radiation is either measured or calculated according to Chapter 3.

The outgoing longwave radiation is composed of an emitted component, which follows the Stefan-Boltzmann behavior, and a reflected component, which is proportional to the incoming longwave radiation. According to Kirchoff's law, the emissivity, transmissivity, and reflectance of a surface must sum to 1.0. The transmissivity of soil surfaces is approximately zero, therefore,

$$I_{ir}^{\downarrow} = \varepsilon \sigma T^4 + (1 - \varepsilon) I_{ir}^{\downarrow}. \tag{4.4}$$

Unlike the shortwave radiation, no corrections are made for sloped surfaces.

4.1.3 Sensible Heat

The sensible heat flux incorporates the transfer of energy between the surface and the atmosphere due to molecular conduction and turbulent mixing. It depends on the temperature gradient between the two media. It is given as (Jordan 1991)

$$H = (e_0 + \rho_a c_{p,a} C_D^h W)(T_a - T) \quad (4.5)$$

with e_0 the windless exchange coefficient for sensible heat (2.0 W/m^2) (Jordan 1996), ρ_a the air density (kg/m^3), $c_{p,a}$ the specific heat of dry air at constant pressure (1005.6 $\text{J/kg}\cdot\text{K}$), C_D the dimensionless drag coefficient (discussed below), W the wind speed (m/s) at a height of 2.0 m , and T_a the air temperature (K) at a height of 2.0 m . Based on the work of Balick et al. (1981), $\rho_a = 0.00348(P_a / T_a)$ where $0.00348 \text{ (kg}\cdot\text{K/m}^3\cdot\text{Pa)}$ is the molecular weight of air divided by the universal gas constant and P_a is the air pressure (Pa).

The parameterization of the drag coefficient, C_D^h , is dependent on the snow depth. If the snow depth is greater than measuring height, Z_a (m) of the air temperature, wind speed and relative humidity, then $C_D^h = 0.002 + 0.006(Z/5000)$, where Z is the site elevation (m). Otherwise (Koenig 1994),

$$C_D^h = \Gamma_h C_{hn}^{g_0} \quad (4.6)$$

where

$$\Gamma_h = \begin{cases} \frac{1.0}{(1.0 - 16.0R_{ib})^{0.5}} & R_{ib} < 0.0 \\ 1.0 & R_{ib} = 0.0 \\ \frac{1.0}{1.0 - 5.0R_{ib}} & 0.0 < R_{ib} < 0.2 \end{cases} \quad (4.7)$$

$$R_{ib} = \frac{2gZ_a(T_a - T)}{(T_a + T)W^2} \quad C_{hn}^{g_0} = \frac{\left[k / \ln(Z_a / z_0^g) \right]^2}{r_{ch}}$$

Γ_h is the sensible heat exchange stability correction factor, $C_{hn}^{g_0}$ is the bulk transfer coefficient near the ground, R_{ib} is the bulk Richardson number, g is the gravitational acceleration (9.81 m/s^2), k is von Karman's constant (0.4), z_0^g is the ground roughness length (0.0006 m for snow/ice, 0.0001 m for pavements, 0.001 m for all soils), and r_{ch} is the turbulent Schmidt number (0.63).

4.1.4 Latent Heat

The latent heat flux term quantifies the energy lost or gained from the surface due to evaporation or condensation, respectively. In order for latent heat to be present, there must be a vapor gradient between the surface and the atmosphere. It is formulated as (Kahle 1977, Balick et al. 1981b)

$$L = \rho_a C_D^e W' l (q_g - q_a) \quad (4.8)$$

where ρ_a is defined in Sec. 4.1.3, l is either the latent heat of evaporation, l_{evap} (2.505e05 J/kg), or sublimation, l_{sub} (2.838e06 J/kg), depending on the air and surface temperatures, q_g is the mixing ratio of the air at the surface, and q_a is the mixing ratio of the air at 2.0 m, and W' is the corrected windspeed (m/s). If W is below 2.0 m/s then $W' = 2.0$ m/s else $W' = W$ (Kahle 1977, Hughes et al. 1993). C_D^e is described similarly to C_D^h except that the turbulent Schmidt number, r_{ch} , is replaced by the turbulent Prandtl number, r_{ce} (0.71), in the expression for the bulk transfer coefficient near the ground and W' replaces W in calculating the bulk Richardson number in Equation (4.7). Balick et al. (1981) give the latent heat of evaporation as

$$l_{evap} = 2,500,775.6 - 2369.729 \left[\frac{T_a - T}{2} - 273.15 \right]. \quad (4.9)$$

The mixing ratio $q_g = M_g q_s(T)$ with M_g the moisture factor ($0 \leq M_g \leq 1$) and q_s the saturated mixing ratio. The value assigned to the moisture factor depends on the degree of saturation of the soil. If it is raining, $M_g = 1$ otherwise it is equal to the surface soil moisture content (refer to Chapter 7). Balick et al. (1981) quantify the mixing ratios as

$$q_{s,a} = \frac{0.622e_d}{P_a - e_d} \quad (4.10)$$

$$e_d = RH_{s,a} \cdot 610.78 \exp \left[\frac{17.269(T_a - 273.15)}{T_a - 35.86} \right]$$

where e_d is the vapor pressure (Pa) and $RH_{s,a}$ is the relative humidity. $RH_s = 1.0$ and $RH_a = RH$ and

$$a = \begin{cases} 17.269 & \text{over water} \\ 21.8745 & \text{over ice/snow} \end{cases}$$

$$b = \begin{cases} 35.86 & \text{over water} \\ 7.66 & \text{over ice/snow} \end{cases}$$

4.1.5 Precipitation Heat

Jordan (1991) quantifies the precipitation heat flux as

$$P = U_p c_p T_p$$

$$U_p = -\gamma_p \frac{\text{fallrate}(m/hr)}{3600(\text{sec}/hr)} \quad (4.11)$$

with T_p the precipitation temperature defined as the wet-bulb temperature, c_p either the specific heat of water, $c_{p,w}$ (4217.7 J/kg·K) or ice, $c_{p,i}$ ($-13.3 + 7.80T_a$ J/kg·K) depending on T_p , U_p the mass precipitation flux ($kg/m^2 \cdot s$), and γ_p the precipitation density (kg/m^3). It is assumed that the precipitation temperature is the same as the air temperature.

4.1.6 Final Top Boundary Equation

Combining Equations (4.2), (4.4), (4.5) (4.8) and (4.11), the top boundary condition is reconfigured as

$$\begin{aligned} F(T) = & (1-\alpha)I_s \downarrow + \varepsilon I_{vp} \downarrow - \varepsilon \sigma T^4 + (e_0 + \rho_a c_{p,a} C_D^h W)(T_a - T) \\ & - \rho_a C_D^e W l (q_g - q_a) + U_p c_p T_p + \kappa \frac{\partial T}{\partial z} @ z = 0 \text{m.} \\ & + l_{fus} \frac{\rho_i}{\rho_w} \frac{\partial \theta_i}{\partial t} \Delta z - v c_p T = 0 \end{aligned} \quad (4.12)$$

This is solved at each time step for the surface temperature.

4.2 Numerical Solution

Equation (4.1) is solved using a modified second-order Crank-Nicholson approach. Following the technique presented in Hornbeck (1975), Equation (4.1) is rewritten as

$$\begin{aligned} \frac{T_{j+1,i} - T_{j,i}}{\Delta t} = & \left[\frac{k_{th_{j+1}} - k_{th_{j,i}}}{\Delta z} \right] \left[\frac{T_{j,i+1} - T_{j,i}}{\Delta z} \right] + \\ & \frac{k_{th_{j,i}}}{2} \left[\frac{T_{j+1,i+1} - 2T_{j+1,i} + T_{j+1,i-1}}{(\Delta z)^2} + \frac{T_{j,i+1} - 2T_{j,i} + T_{j,i-1}}{(\Delta z)^2} \right] \\ & - \frac{c_{p,w}}{c_{p,j,i}} v_{j,i} \left[\frac{T_{j,i+1} - T_{j,i}}{\Delta z} \right] + \frac{l_{fus}}{c_p} \frac{\rho_i}{\rho_w} \frac{(\Delta \theta_i)_{j,i}}{\Delta t}. \end{aligned} \quad (4.13)$$

where the subscripts j and i represent time and depth, respectively. Combining like terms and rearranging so that all terms involving T_{j+1} are on the left-hand side of the equation, Equation (4.13) becomes

$$\begin{aligned} T_{j+1,i-1} + \gamma_{j,i} T_{j+1,i} + T_{j+1,i+1} = & \\ -T_{j,i-1} + T_{j,i} (\beta_{j,i} + \alpha_{j,i} - \delta_{j,i}) + T_{j,i+1} (1 - \beta_{j,i} + \delta_{j,i}) + \mu_{j,i} & \equiv \phi_{j,i} \end{aligned} \quad (4.14)$$

where

$$\begin{aligned}\alpha_{j,i} &= -2 \left(\frac{(\Delta z)^2}{k_{th_{j,i}} (\Delta t)} \right), \quad \gamma_{j,i} = \alpha_{j,i} - 2, \quad \beta_{j,i} = 2 \left(\frac{k_{th_{j,i+1}}}{k_{th_{j,i}}} \right), \\ \delta_{j,i} &= 2v_{j,i} \left(\frac{c_{p,w}}{c_{p_{j,i}}} \frac{\Delta z}{k_{th_{j,i}}} \right), \quad \mu_{j,i} = \alpha_{j,i} \frac{l_{fus}}{c_p} \frac{\rho_i}{\rho_w} (\Delta \theta_i)_{j,i}.\end{aligned}\quad (4.15)$$

Equation (4.14) is solved for T_{j+1} using a Newton-Raphson technique so that the final matrix equation becomes

$$\begin{bmatrix} -\gamma_{j,1} & -1 & & & \\ -1 & -\gamma_{j,2} & -1 & & \\ & & \ddots & & \\ & & & -1 & -\gamma_{j,n-1} & -1 \\ & & & & -1 & -\gamma_{j,n} \end{bmatrix} \begin{bmatrix} \Delta T_{j+1,1} \\ \Delta T_{j+1,2} \\ \vdots \\ \Delta T_{j+1,n-1} \\ \Delta T_{j+1,n} \end{bmatrix} = \begin{bmatrix} B_1 \\ B_2 \\ \vdots \\ B_{n-1} \\ B_n \end{bmatrix} \quad (4.16)$$

where

$$B_i = -T_{j+1,i-1} - \gamma_{j,i} T_{j+1,i} - T_{j+1,i+1} + \phi_{j,i} \quad 2 \leq i \leq n-1. \quad (4.17)$$

T_1 must satisfy the boundary condition set forth in Equation (4.2). Following the technique of Kahle (1977), Equation (4.2) may be rewritten in the form

$$T^4 + c_1 T + c_2 = 0 \quad (4.18)$$

with

$$\begin{aligned}c_1 &= \frac{1}{\varepsilon_1 \sigma} \left[\left(e_0 + \rho_a c_{p,a} C_D^h W \right) + \rho_a C_D^e W' l M_g \frac{\partial q_s}{\partial T} \Big|_{T=T_{j-1,1}} + U_p c_p + \kappa_1 \frac{1}{\Delta z_1} \right] \\ c_2 &= \frac{-1}{\varepsilon_1 \sigma} \left[\left((1-\alpha) I_s \downarrow + \varepsilon I_{ir} \downarrow + \left(e_0 + \rho_a c_{p,a} C_D^h W \right) T_a + U_p c_p T_a + \kappa_1 \frac{T_{j-1,2}}{\Delta z_1} \right) \right. \\ &\quad \left. - \rho_a C_D^e W' l \cdot \left(M_g \left(q_s (T_{j-1,1}) - \frac{\partial q_s}{\partial T} \Big|_{T=T_{j-1,1}} \cdot T_{j-1,1} \right) - q_a \right) \right].\end{aligned}\quad (4.19)$$

The above assumes that $\kappa dT/dz = \kappa_1 (T_2 - T_1) / \Delta z_1$ and that the saturated mixing ratio may be represented as

$$q_s = q_s (T_{j-1,1}) + \frac{\partial q_s}{\partial T} (T_{j-1,1}) [T_{j,1} - T_{j-1,1}]. \quad (4.20)$$

Equation (4.18) is solved for T using the Newton-Raphson technique.

To ensure numerical stability when solving Equation (4.16), the following criterion holds on the time step for each node:

$$k_{th,i} \left(\frac{\Delta t}{(\Delta z_i)^2} \right) < \frac{1}{2}. \quad (4.21)$$

The thermal diffusivity can change as a function of depth and time depending on the soil layer structure. To simplify calculations, the vertical node increments, Δz_i , are held fixed. The time increment, Δt , is allowed to vary according to

$$k_{th,i} \frac{\Delta t}{(\Delta z_i)^2} < 0.5 \rightarrow \Delta t = \min \left[\frac{0.45(\Delta z_i)^2}{k_{th,i}} \right]. \quad (4.22)$$

Ensuring that the conditions set forth in Equation (4.21) are met, a lower value of 0.45 is used to calculate the time step. Determination of the soil thermal diffusivity, k_{th} , and other physical properties needed to solve Equation (4.16) are discussed in Section 4.3. At each calculation time step, Δt is updated as necessary depending on the current soil physical properties.

4.3 Material Properties

To determine the vertical temperature profile in the ground as governed by Equation (4.16), several physical characteristics of the material are needed. They are the surface albedo, α , and emissivity, ε , and the nodal thermal conductivity, κ , and thermal diffusivity, k . The latter two parameters are, among other things, dependent on the temperature and moisture content of the soil.

Following the recommendations of Farouki (1981), Johanson's method (1975) is used to calculate the soil thermal conductivity as a function of soil type, porosity (n), dry density (γ_d), degree of saturation (S_r), quartz content (q), dry thermal conductivity (κ_{dry}), saturated thermal conductivity (κ_{sat}), thermal conductivity of the soil solids (κ_s), unfrozen water volume (ww), and the Kersten number (K_e). The governing equation is

$$\kappa = (\kappa_{sat} - \kappa_{dry})K_e + \kappa_{dry} \quad (4.23)$$

where

$$\kappa_{dry} = \begin{cases} \text{provided by user} \\ \frac{135\gamma_d + 64.7}{2700 - 947\gamma_d} \pm 20\% \\ 0.05 \quad T_{j,i} > 273.15K \quad \text{peat} \\ 0.55 \quad T_{j,i} \leq 273.15K \quad \text{peat} \end{cases} \quad (4.24)$$

$$\kappa_{sat} = \begin{cases} 0.57^n \kappa_s^{(1-n)} \quad T_{j,i} > 273.15K \\ 2.2^n \kappa_s^{(1-n)} 0.269^{ww} \quad T_{j,i} \leq 273.15K \\ 0.55 \quad T_{j,i} > 273.15K \quad \text{peat} \\ 1.80 \quad T_{j,i} \leq 273.15K \quad \text{peat} \end{cases} \quad (4.25)$$

$$K_e = \begin{cases} 0.7 \log S_r + 1.0 \quad T_{j,i} > 273.15K \quad \text{coarse} \\ \log S_r + 1.0 \quad T_{j,i} > 273.15K \quad \text{fine} \\ S_r \quad T_{j,i} \leq 273.15K \end{cases} \quad (4.26)$$

$$\kappa_s = \begin{cases} 7.7^q 3.0^{(1-q)} & q < 0.20 \text{ coarse} \\ 7.7^q 2.0^{(1-q)} & \text{all others} \end{cases} \quad (4.27)$$

and $\kappa_w = 0.0018T_{j,i} + 0.0787$, $\kappa_i = 488.19T_{j,i}^{-1} + 0.4685$. Farouki (1981) found that Johansen's method for predicting soil thermal conductivity matched the existing data well except for the case of dry ($S_r < 0.2$), unfrozen, coarse soils. Since the recommended methods for this situation rely on unavailable curve fitting parameters, Johansen (1975) is used for all conditions. The physical properties used in Equations (4.23)–(4.27) for the 15 USCS soil types are given in Table 4.3.1.

The soil thermal diffusivity, k_{th} , is equal to

$$k_{th} = \frac{\kappa}{C} \quad (4.28)$$

where the volumetric heat capacity, C , is defined as (Farouki 1981)

$$C = (1-n)\gamma_d C_s + (ww)\rho_w C_w + (n - [ww + wi])\rho_a C_a + (wi)\rho_i (-13.3 + 7.8T_{j,i}) \quad (4.29)$$

and $C_w = 4217.7 \text{ J/kg}\cdot\text{K}$ is the specific heat of water, $C_a = 1250.0 \text{ J/kg}\cdot\text{K}$ is the specific heat of air, and C_s is the specific heat of solids given in Table 4.3.1.

Table 4.3.1 Default Soil Properties

Soil Type	Bulk Dry Density γ_d (g/cm ³)	Porosity n	Emissivity ¹ ε	Albedo ¹ α	Quartz Content ² q	Organic Fraction θ_{of}	Specific Heat ³ C_s (J/kg·K)	Fine/Coarse [*]
GW	1.95 ⁵	0.296 ⁵	0.92	0.40	0.65	0.00	820.0	1
GP	2.16 ⁵	0.203 ⁵	0.92	0.40	0.65	0.00	820.0	1
GM	1.91 ⁵	0.324 ⁵	0.95	0.40	0.65	0.00	820.0	1
GC	1.87 ⁵	0.34 ⁴	0.92	0.40	0.65	0.00	820.0	1
SW	1.876 ⁵	0.320 ⁵	0.92	0.40	0.80	0.00	830.0	1
SP	1.594 ⁵	0.415 ⁵	0.92	0.35	0.80	0.00	816.4 ⁷	1
SM	1.474 ⁵	0.526 ⁵	0.92	0.35	0.80	0.05	850.6	1
SC	1.88 ⁵	0.400 ⁵	0.92	0.35	0.80	0.05	830.0	1
ML	1.457 ⁵	0.464 ⁵	0.94	0.40	0.35	0.10	845.7 ⁷	2
CL	1.589 ⁵	0.422 ⁵	0.97	0.23	0.05	0.10	854.1 ⁷	2
OL	1.165 ⁵	0.533 ⁵	0.955	0.265	0.20	0.25	837.4 ⁷	2
CH	1.517 ⁵	0.457 ⁵	0.98	0.30	0.05	0.10	845.7 ⁷	2
MH	1.060 ¹	0.547 ¹	0.94	0.30	0.35	0.10	830.0	2
OH	0.841 ¹	0.892 ⁴	0.955	0.265	0.20	0.25	866.7 ⁷	2
PT	0.25	0.70	0.92	0.40	0.05	0.50	830.0	2
SMSC (MC)	1.60 ¹	0.396 ¹	0.92	0.40	0.80	0.05	830.0	1
CLML (CM)	1.617 ⁵	0.397 ⁵	0.96	0.30	0.20	0.10	830.0	2
EV	1.876 ⁵	0.320 ⁵	0.92	0.40	0.80	0.00	830.0	1
CO	2.185	0.020	0.90 ⁶	0.40 ⁶		0.00	850.0	
AS	2.500	0.020	0.94 ⁶	0.125 ⁶		0.00	880.0	
RO	2.700	0.020	0.89	0.40		0.00	800.0	
SN	0.920	0.020	0.90	0.70		0.00		

¹ Sullivan et al. (1997), p. 28, 38, and 51

² Tarnawski et al. (1997), p. 96

³ Farouki (1981), p. 136

⁴ Yu et al. (1993)

⁵ Guymon, et al. (1993), p. 21, 25, 47–59

⁶ Balick, L.K. et al. (1981), Table B1

4.4 Model Validation

We conducted a comparison of the surface temperatures generated using the model and measured values for Grayling, MI, during the fall of 1992 and for Yuma, AZ, during the spring of 1993 and Hanover, NH, during the winter of 2002. The data collected consist of soil temperature profiles as well as meteorological conditions. Almost no soil properties data were collected, thus we had to estimate these based on values found in the literature for the general soil types at the sites. The Yuma and Grayling locations are sandy while the CRREL site is pavement. The data collected for the first two sites are part of the SWOE series.

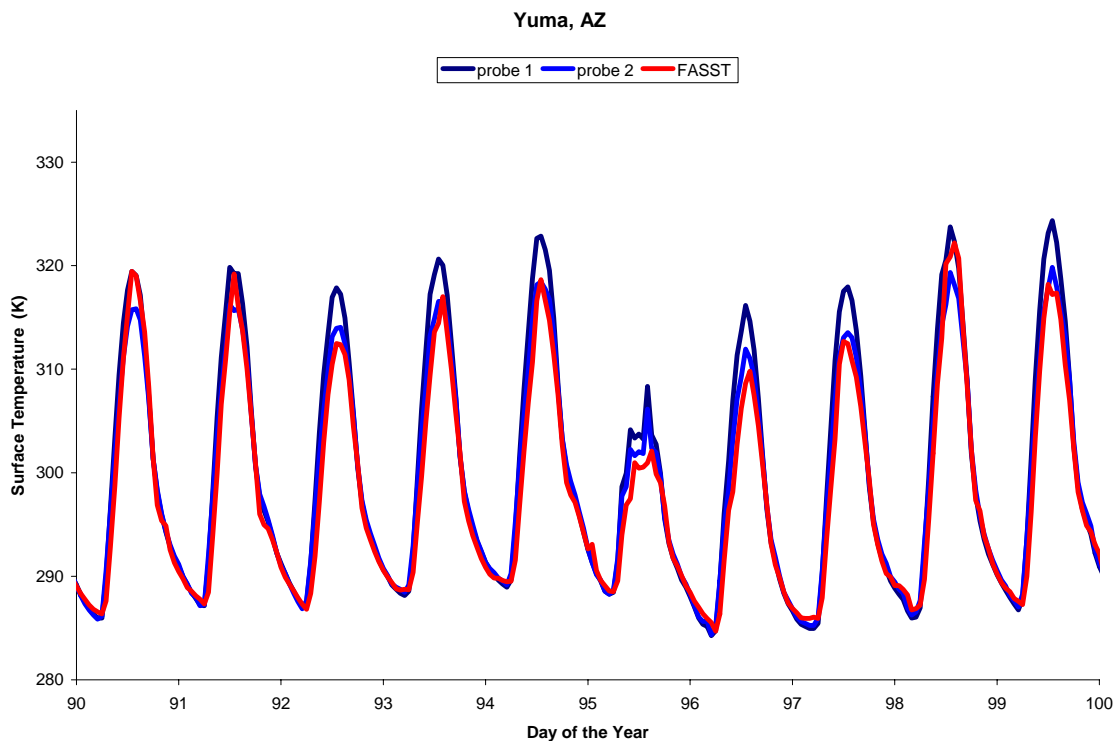


Figure 4.3 Comparison of model results and measurements for surface temperature (K) for Yuma, AZ.

Figure 4.3 demonstrates the capability of FASST. Except for soil type, no other information was collected. The two temperature probes were placed side by side in the vicinity of the meteorological station.

The initial soil temperature profile is either input by the user or generated by the model, which assumes a uniform profile equal to the air temperature. In either case, the model

assumes that the bottom heat flux is constant throughout the exercise. One example of the difference between having measured initial soil temperature profile data and letting the program calculate one is seen in Figure 4.4 below for the Yuma, AZ, data. The “yes” case is the same as the model results shown in Figure 4.3. Based on the user-specified number of layers, position and number of initial soil temperature and moisture measurements, and the total thickness, the model divided the profile into 15 nodes. For the two “no” cases, everything was retained from the “yes” scenario except the measured initial soil temperatures. In one “no” run, the number of nodes was forced to be the same as in the “yes” case; in the other “no” run, the model determined the required number. As can be seen, essentially no difference is discerned between the three runs except at the start of the simulation.

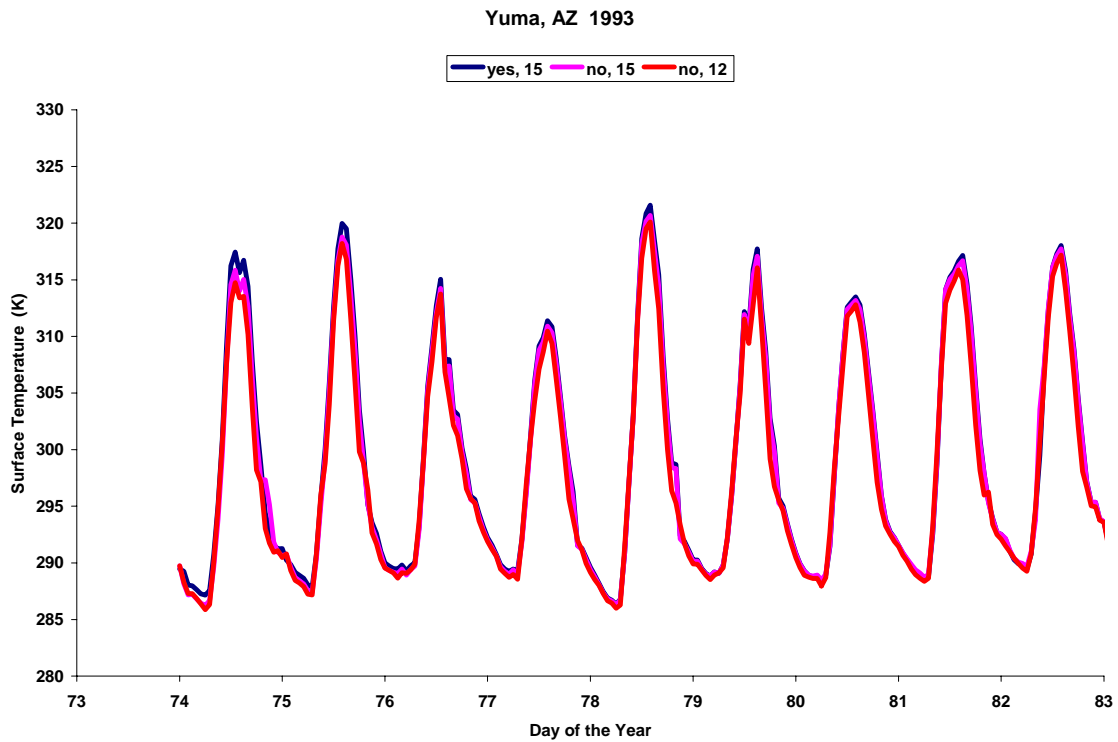


Figure 4.4 Effect on the results of having initial soil temperature profile data (yes) versus letting the model compute one (no). The number in the legend indicates the number of nodes.

We used the Yuma, AZ, data to perform a sensitivity study on the model. The variables tested were number of layers, albedo, and emissivity. We let the model calculate the thermal conductivity and diffusivity. We found no dependence in the results on the number of layers. The results showed little sensitivity to the emissivity. The albedo does affect the surface temperature since the larger the albedo, the less shortwave radiation is absorbed by the surface. The results are seen in Figure 4.5.

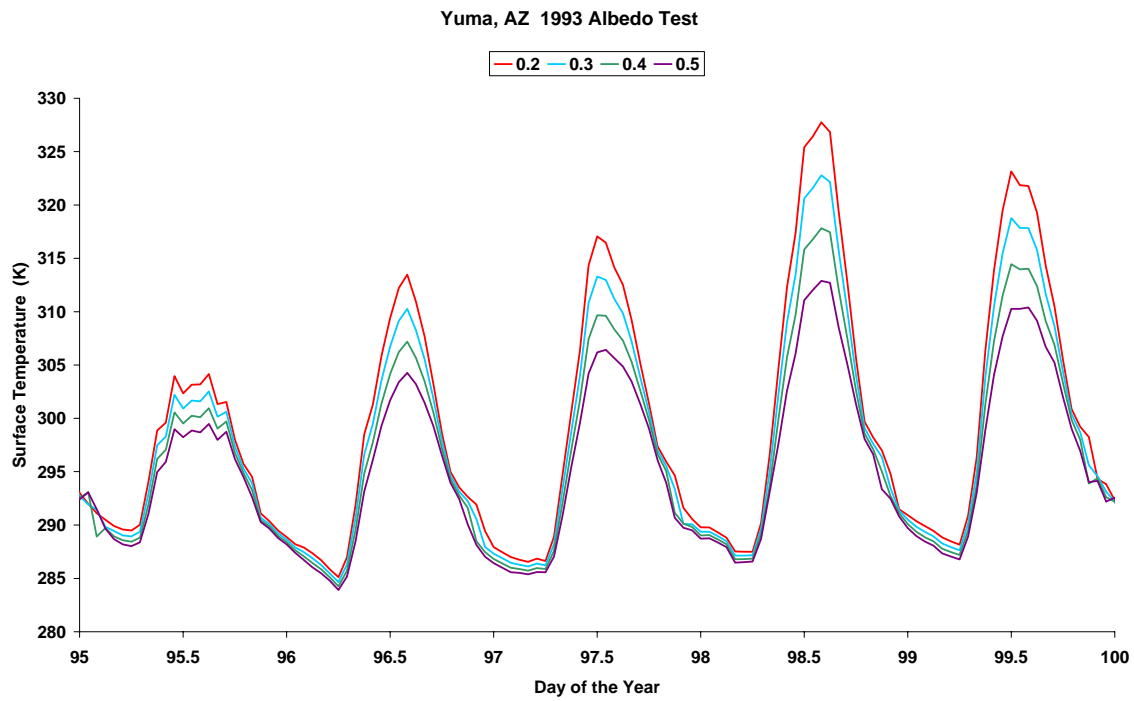


Figure 4.5 Sensitivity of the surface temperature to the albedo.

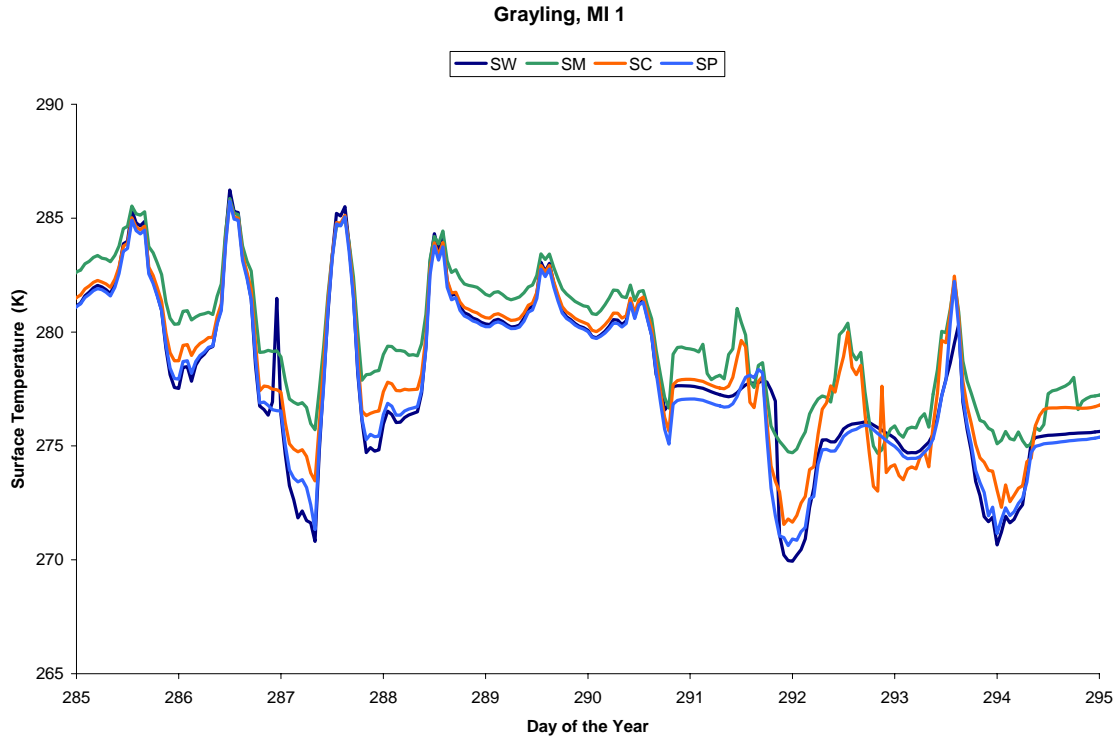


Figure 4.6 The effect of soil type on surface temperature for Grayling, MI.

Since the category of “sand” is broad, we investigated the effects of using different combinations of sand layers with the Grayling, MI, data. We tested all four types: SM (silty sand), SW (well-graded sand), SP (poorly graded sand), and SC (clayey sand). The results are presented in Figure 4.6. The differences follow the thermal conductivity gradient, with the SW soil having the lowest thermal conductivity and the SM soil the highest.

FASST will also be used to predict the surface condition of pavement for mobility purposes. As can be seen in Figure 4.7, it does this very well for the data collected at the Army Corps of Engineer’s CRREL, Hanover, NH, site, especially when compared to the spot radiometer, which is more accurate than the thermistor.

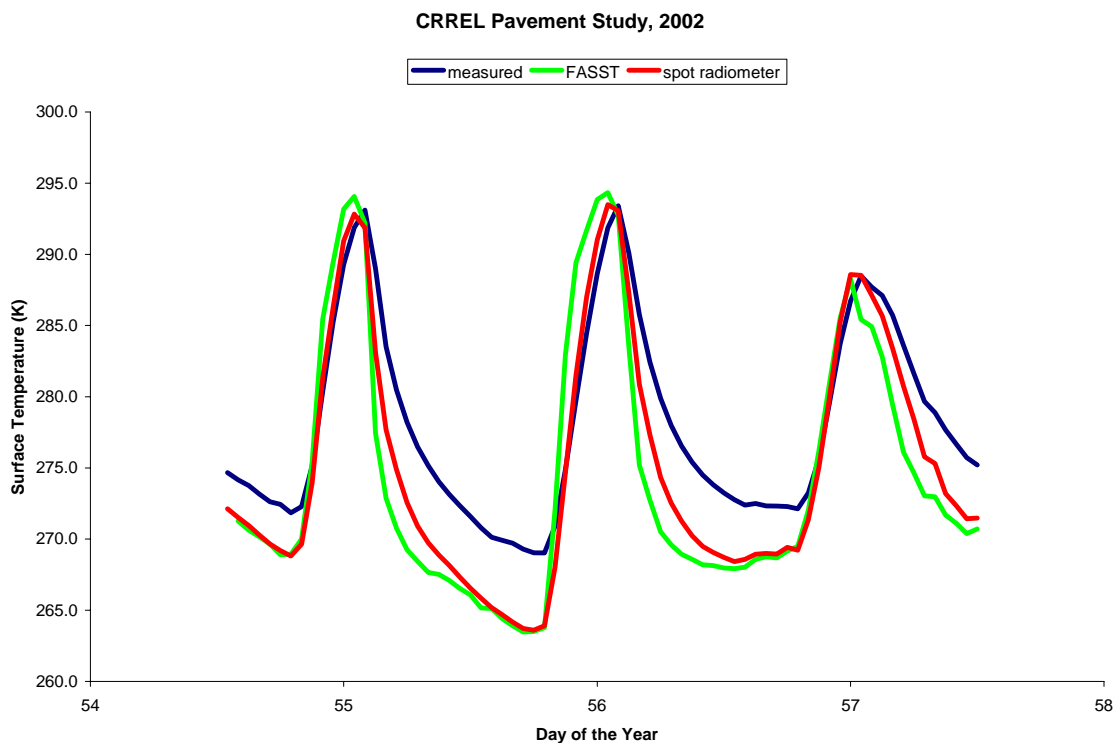


Figure 4.7 Comparison of FASST and measured pavement surface temperatures.

4.5 References

Balick, L.K., L.E. Link, R.K. Scoggins, and J.L. Solomon (1981a) Thermal Modeling of Terrain Surface Elements. U.S. Army Engineer Waterways Experiment Station Environmental Laboratory, Technical Report EL-81-2.

Balick, L.K., R.K. Scoggins, and L.E. Link (1981b) Inclusion of a Simple Vegetation Layer in Terrain Temperature Models for Thermal IR Signature Prediction. *IEEE Trans on Geoscience and Remote Sensing*, V. GE-19, No. 3, p. 143–152.

Farouki, O.T. (1981) Thermal Properties of Soils. U.S. Army Cold Regions Research and Engineering Laboratory, Monograph 81-1.

Guymon, G.L., R.L. Berg, and T.V. Hromadka (1993) Mathematical Model of Frost Heave and Thaw Settlement in Pavements. U.S. Army Cold Regions Research and Engineering Laboratory, CRREL Report 93-2.

Hornbeck, R.W. (1975) *Numerical Methods*, New Jersey: Prentice-Hall.

Hughes, P.A., T.J.L. McComb, A.B. Rimmer, and K.E. Turver (1993) A Mathematical Model for the Prediction of Temperature of Man-Made and Natural Surfaces. *International Journal of Remote Sensing*, V. 14, No. 7, p. 1383–1412.

Johansen, O. (1975) Thermal Conductivity of Soils. Ph.D. thesis, Trondheim, Norway. U.S. Army Cold Regions Research and Engineering Laboratory, CRREL Draft Translation 637, 1977.

Jordan, R. (1991) A One-Dimensional Temperature Model for a Snow Cover: Technical Documentation of SNTHERM.89. U.S. Army Cold Regions Research and Engineering Laboratory, Special Report 91-16.

Jordan, R. (1996) User's Guide for USACRREL One-Dimensional Snow Temperature Model (SNTHERM.89). U.S. Army Cold Regions Research and Engineering Laboratory.

Kahle, A.B. (1977) A Simple Thermal Model of the Earth's Surface for Geologic Mapping by Remote Sensing. *Journal of Geophysical Research*, V. 82, No. 11, p. 1673–1680.

Koenig, G.G. (1994) Smart Weapons Operability Enhancement (SWOE) Joint Test and Evaluation (JT and E) Program: Final Report. Dr. James P. Welch, Joint Test Director, SWOE JT and E, SWOE Report 94-10, Annex D.

Pollack, H.N., Hurter, S.J., and Johnson, J.R. (1993) Heat flow from the earth's interior: Analysis of the global data set. *Reviews of Geophysics*: 31(3), 267–280 (www.geo.lsa.umich.edu/IHFC/heatflow.html).

Press, W.H., S.A. Teukolsky, W.T. Vetterling, and B.P. Flannery (1992) *Numerical Recipes in FORTRAN: The Art of Scientific Computing, Second Edition*. New York: Cambridge University Press.

Sullivan, P.M., C.D. Bullock, N.A. Renfroe, M.R. Albert, G.G. Koenig, L. Peck, and K. O'Neill (1997) Soil Moisture Strength Prediction Model, Version II (SMSPII). U.S. Army Corps of Engineers Waterways Experiment Station, Technical Report GL-97-15.

Tarnawski, V.R., B. Wagner, J. Webber, and L. Pettipas (1997) Optimization of Soil Mineralogical Composition for Prediction Soil Thermal Conductivity. *Proceedings, International Symposium on Physics, Chemistry, and Ecology of Seasonally Frozen Soils*,

I.K. Iskandar, E.A. Wright, J.K. Radke, B.S. Sharratt, P.H. Groeneveld, and L.D. Hinzman (Ed.), Fairbanks, AK, June 10–12. U.S. Army Cold Regions Research and Engineering Laboratory, Special Report 97-10, p. 91–97.

Yu, C., C. Loureiro, J.-J. Cheng, L.G. Jones, Y.Y. Wang, Y.P. Chia, and E. Faillace (1993) Data Collection Handbook to Support Modeling Impacts of Radioactive Material in Soil. Environmental Assessment and Information Sciences Division, Argonne National Laboratory, Argonne, Illinois (www.ead.anl.gov/resrad/datacoll/dcall.htm).

Chapter 5

Soil Moisture and Strength Models

5.0 Introduction

Calculating changes in the volumetric moisture content profile as a function of time is the critical step in determining the state of the ground. This is in part due to the highly nonlinear nature of the parameters associated with soil moisture.

5.1 Soil Moisture

5.1.1 Governing Equations

The flow of water (v) through a porous media is governed by Darcy's Law, which states that

$$v = K \frac{\partial h}{\partial z} \quad (5.1)$$

where K (m/s) is the hydraulic conductivity, z (m) is the depth, positive downward from the surface, and h (m) the total head equals the elevation head, or depth, (z) minus the pressure head (ψ), i.e., $h = z \cos \varphi - \Psi = z \cos \varphi - P_f / \rho_w g$, P_f (Pa) is pressure, ρ_w (kg/m^3) is the density of water, φ is the surface slope, and g (m^2/s) is gravity. If the soil is unsaturated, $\psi < 0$ and $h > z \cos \varphi$. For saturated soils $\psi \geq 0$, requiring that $h \leq z \cos \varphi$.

Also governing the flow of moisture through a soil is the conservation of mass, which states that the time rate of change of the moisture content in a given volume equals the net gain/loss of fluid in the volume, i.e.,

$$\frac{\partial \theta_w}{\partial t} = -\frac{\partial v}{\partial z} - \frac{\rho_i}{\rho_w} \frac{\partial \theta_i}{\partial t} + \text{sources} - \text{losses} \quad (5.2)$$

where θ_w (cm^3/cm^3) is the volumetric moisture content, θ_i (cm^3/cm^3) is the volumetric ice content, ρ_i (kg/m^3) is the density of ice, and t (sec) is time. Equation (5.2) assumes that changes with respect to time in the soil porosity and water density are negligible compared to changes in the soil moisture and total head. Further discussion on the change in ice content is found in Chapter 6. The source and loss terms in this equation account for occurrences such as runoff and plant root uptake. The latter is for future development.

Equation (5.2) is subject to the following flow boundary conditions at the surface and at the bottom of the soil column:

$$\begin{aligned} q_{top} &= -E + C_r + P + (h_{pond} + h_{i,melt} + h_{s,melt}) / \Delta t & @ z = 0 \\ q_{bot} &= K \sin(slope) & @ z = z_{bot} \end{aligned} \quad (5.3)$$

where E (m/s) is the evaporation rate, C_r (m/s) is the condensation rate, P (m/s) is the rate of precipitation, and h_{pond} (m) is the head due to water collecting on the surface, and $h_{i,melt}$ (m) and $h_{s,melt}$ (m) are the heads due to melting ice and snow, respectively, and Δt (sec) is the time step. If the ground is sloped, no water accumulates and any water that falls on the surface, but which does not infiltrate, becomes runoff.

The evaporation and condensation rates depend on the moisture difference between the air and the surface. They are quantified as the latent heat flux. Following the procedure outlined in Chapter 4, Section 4.1.6, the modified surface energy balance is rearranged such that

$$\begin{aligned} \text{latent heat} = & (1-\alpha)I_s \downarrow + \varepsilon I_{ir}^\downarrow - \varepsilon \sigma T^4 + \rho_a c_{p,a} C_D W(T_a - T) \\ & + U_p c_p T_p + \kappa \frac{\partial T}{\partial z} \end{aligned} . \quad (5.4)$$

Reference should be made to Chapter 6 for explanation of the individual terms. The moisture flux to/from the surface is then

$$\text{moisture flux} = \frac{\text{latent heat}}{\rho_w l} \quad (5.5)$$

and l (J/kg) is the latent heat of evaporation if the air temperature is above freezing and the latent heat of sublimation otherwise. If the latent heat flux is positive, evaporation is occurring, otherwise condensation is happening.

5.1.2 Numerical Solution

Equation (5.2) is solved numerically using an explicit scheme such that

$$\frac{\theta_{w_{j+1,i}} - \theta_{w_{j,i}}}{\Delta t} = - \left[\frac{v_{j+1,i+1} - v_{j+1,i}}{\Delta z_i} \right] + \text{sources}(i) - \text{losses}(i) \quad (5.6)$$

where

$$\begin{aligned} v_i &= K_{i-1/2} \left[\frac{h_i - h_{i-1}}{z_i - z_{i-1}} \right] \\ v_{i+1} &= K_{i+1/2} \left[\frac{h_{i+1} - h_i}{z_{i+1} - z_i} \right] \end{aligned} . \quad (5.7)$$

$h_i = z_i \cos \varphi - \Psi_i$, $\Delta z_i = (z_{i+1} - z_{i-1})/2$, n_i is the porosity at i and the subscripts j and i represent time and depth, respectively. The change in soil moisture content due to changes in the ice content, i.e., freezing/thawing, is incorporated into the source and sink terms. In Equation (5.2) it is the second term on the right-hand side. Equation (5.6) is solved for ψ_i using a Newton-Raphson technique so that the final matrix equation becomes

$$\begin{bmatrix} \gamma_1 & a_1^+ & & & & \\ a_2^- & \gamma_2 & a_2^+ & & & \\ & & \ddots & & & \\ & & & a_{n-1}^- & \gamma_{n-1} & a_{n-1}^+ \\ & & & & a_n^- & \gamma_n \end{bmatrix} \begin{bmatrix} \Delta\Psi_{j+1,1} \\ \Delta\Psi_{j+1,2} \\ \vdots \\ \Delta\Psi_{j+1,n-1} \\ \Delta\Psi_{j+1,n} \end{bmatrix} = \begin{bmatrix} B_1 \\ B_2 \\ \vdots \\ B_{n-1} \\ B_n \end{bmatrix} \quad (5.8)$$

where

$$a_i^+ = \frac{\partial B_i}{\partial \Psi_{i+1}} = \frac{\Delta t}{\Delta z_i} \left[\frac{\partial K_{i+1/2}}{\partial \Psi_{i+1}} \left\{ \cos \varphi - \frac{\Psi_{i+1} - \Psi_i}{z_{i+1} - z_i} \right\} - \frac{K_{i+1/2}}{z_{i+1} - z_i} \right] \quad (5.9)$$

$$a_i^- = \frac{\partial B_i}{\partial \Psi_{i-1}} = \frac{\Delta t}{\Delta z_i} \left[\frac{\partial K_{i-1/2}}{\partial \Psi_{i-1}} \left\{ \cos \varphi - \frac{\Psi_i - \Psi_{i-1}}{z_i - z_{i-1}} \right\} + \frac{K_{i-1/2}}{z_i - z_{i-1}} \right]$$

$$\gamma_i = \frac{\partial B_i}{\partial \Psi_i} = \phi_i + \begin{cases} \frac{\Delta t}{\Delta z_i} \left[\frac{\partial K_{i+1/2}}{\partial \Psi_i} \left\{ \cos \varphi - \frac{\Psi_{i+1} - \Psi_i}{z_{i+1} - z_i} \right\} + \frac{K_{i+1/2}}{z_{i+1} - z_i} \right] & i = 1 \\ \frac{\Delta t}{\Delta z_i} \left[\frac{\partial K_{i+1/2}}{\partial \Psi_i} \left\{ \cos \varphi - \frac{\Psi_{i+1} - \Psi_i}{z_{i+1} - z_i} \right\} + \frac{K_{i+1/2}}{z_{i+1} - z_i} \right. \\ \left. - \frac{\partial K_{i-1/2}}{\partial \Psi_{i-1}} \left\{ \cos \varphi - \frac{\Psi_i - \Psi_{i-1}}{z_i - z_{i-1}} \right\} + \frac{K_{i-1/2}}{z_i - z_{i-1}} \right] & 2 \leq i \leq n-1 \\ \frac{\Delta t}{\Delta z_i} \left[- \frac{\partial K_{i-1/2}}{\partial \Psi_{i-1}} \left\{ \cos \varphi - \frac{\Psi_i - \Psi_{i-1}}{z_i - z_{i-1}} \right\} + \frac{K_{i-1/2}}{z_i - z_{i-1}} \right] & i = n \end{cases} \quad (5.10)$$

$$\phi_i = \frac{\partial \theta_{w_{j+1,i}}}{\partial \Psi_i}, \quad B_i = \theta_{w_{j+1,i}} - \theta_{w_{j,i}} + \frac{\Delta t}{\Delta z_i} (v_{j+1,i+1} - v_{j+1,i}) - sources(i) + losses(i). \quad (5.11)$$

To ensure numerical stability when solving Equation (5.8), Δt is chosen such that $(K_{sat})_i \Delta t < \Delta z_i$, where $(K_{sat})_i$ is the saturated hydraulic conductivity. Default values for K_{sat} for the different USCS soil types are found in Table 5.1.1 located in the next section.

5.1.3 Hydraulic Parameters

The relationship between volumetric moisture content and pressure head is highly nonlinear. Following the work of van Genuchten (1980) it is

$$\theta_w = \theta_r + \frac{\theta_{max} - \theta_r}{\left(1 + |\alpha_{vG} \Psi|^{n_{vG}}\right)^{m_{vG}}} \quad (5.12)$$

where θ_r is the residual volumetric water content, θ_{max} is the maximum volumetric water content, α_{vG} (cm^{-1}) is a constant related to the reciprocal of the bubbling pressure head, n is a constant dependent on the distribution of pores, and $m_{vG} = 1 - 1/n_{vG}$. Default values for θ_r , θ_{max} , α_{vG} , and n_{vG} are found in Table 5.1.1. As can be seen in Figure 5.1, the

relationship between the volumetric moisture content and the pressure head is highly nonlinear.

Table 5.1.1 Default Soil Moisture Properties.

Soil Type	Saturated Hydraulic Conductivity K_{sat} (cm/s)	Residual Water Content θ_r (m ³ /m ³)	Maximum Water Content θ_{max} (m ³ /m ³)	<i>Van Genucht. exponent</i> n_{vG}	Bubbling Pressure Head α_{vG} (cm)
GW	0.00026 ²	0.01	0.296 ²	1.5 ³	22.6 ¹
GP	0.0001056 ²	0.01	0.403 ²	2.2 ³	22.6 ¹
GM	0.000067 ²	0.01	0.324 ²	1.2 ³	32.7 ¹
GC	0.00001389 ¹	0.01	0.34 ⁴	1.5 ³	23.2 ¹
SW	0.00002361 ²	0.01	0.320 ²	1.25 ³	38.547 ³
SP	0.00000741 ²	0.01	0.415 ²	2.5 ³	38.547 ³
SM	7.987e-06 ²	0.01	0.526 ²	1.4 ³	68.547 ³
SC	0.00000029 ²	0.01	0.400 ²	1.5 ³	58.547 ³
ML	0.00000057 ²	0.01	0.464 ²	1.5 ³	33.9 ¹
CL	7.7e-08 ²	0.01	0.422 ²	1.34 ³	53.5 ¹
OL	0.00009722 ²	0.01	0.533 ²	1.34 ³	28.6 ¹
CH	4.8e-08 ²	0.01	0.457 ²	1.5 ³	32.9 ¹
MH	1.5e-08 ¹	0.01	0.547 ²	1.34 ³	39.0 ¹
OH	0.000883 ¹	0.01	0.892 ⁴	1.34 ³	29.3 ¹
PT	0.000014	0.15	0.70	1.34	38.6
SMSC (MC)	7.7e-07 ²	0.01	0.396 ²	1.5 ³	23.547 ³
CLML (CM)	1.26e-07 ²	0.01	0.397 ²	1.34 ³	32.9 ¹
EV	0.00002361 ²	0.01	0.320 ²	1.25 ³	38.547 ³
CO, AS, RO, SN	0.0	0.001	0.02		

¹ Sullivan et al. (1997), p. 28

² Guymon et al. (1993), p. 21, 25, 47–59

³ Jordan (2000)

⁴ Yu et al. (1993)

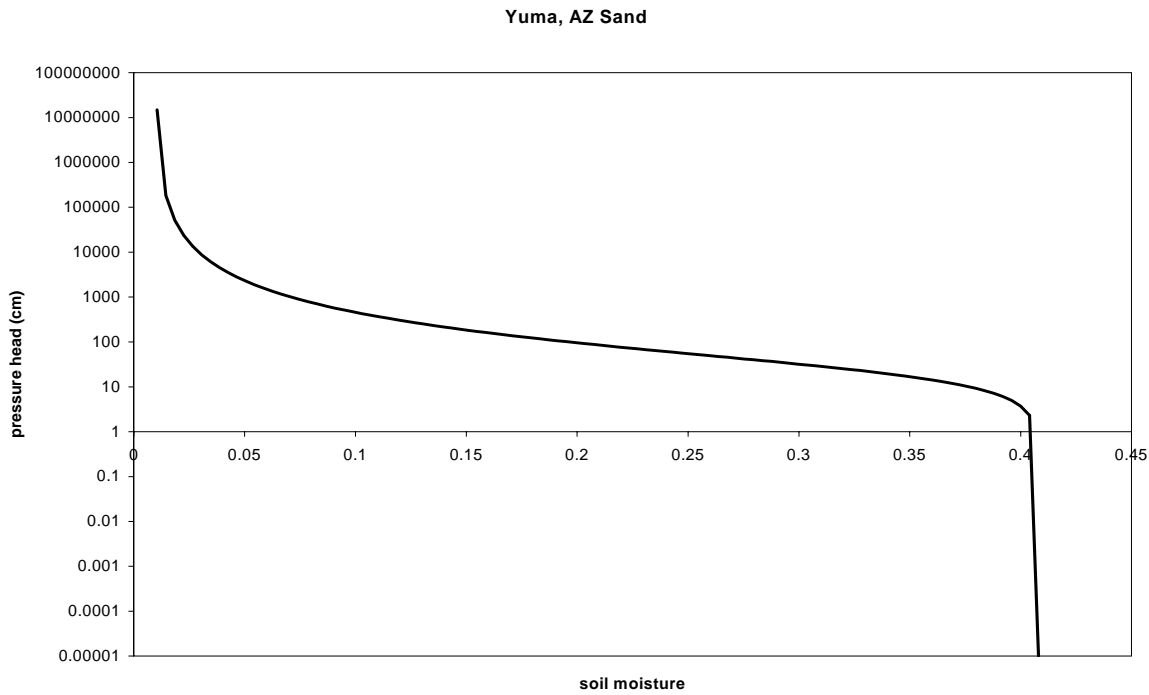


Figure 5.1 ψ versus θ for Yuma, AZ, sand.

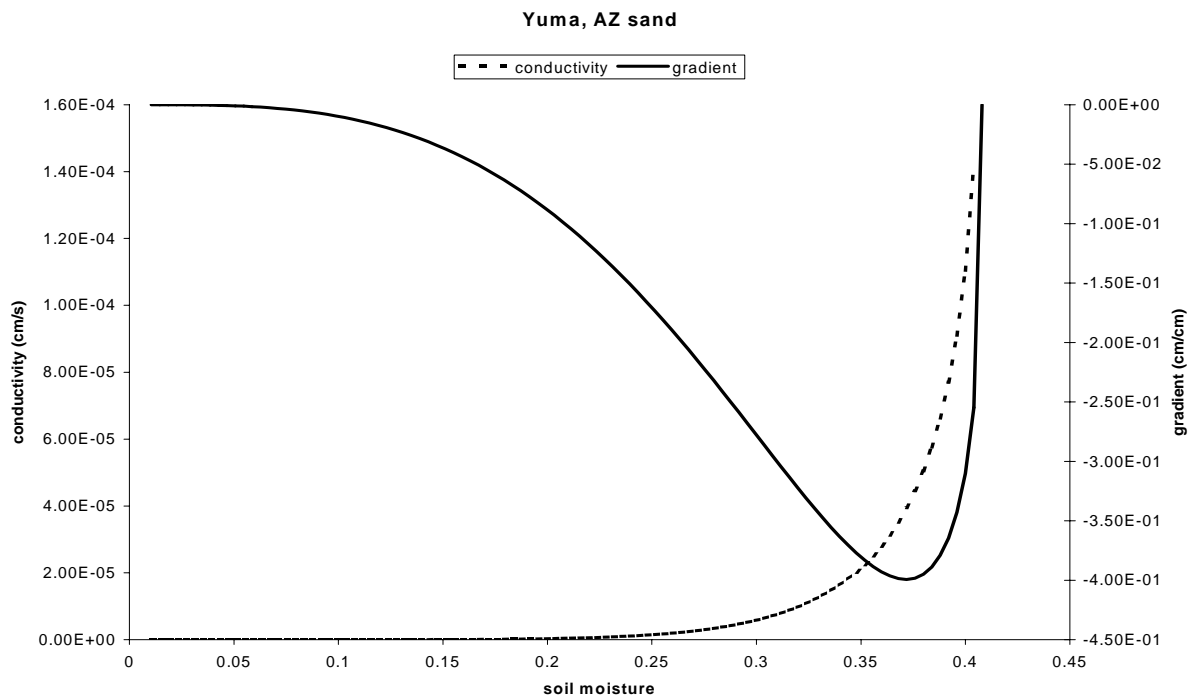


Figure 5.2 K versus θ and $\partial\theta/\partial\psi$ versus θ for Yuma, AZ, sand.

The hydraulic conductivity also depends on the volumetric moisture content such that (van Genuchten 1980)

$$K = K_{sat} w^{0.5} \left[1 - \left(1 - w^{1/m_{vG}} \right)^{m_{vG}} \right]^2 \quad (5.13)$$

where

$$w = \frac{\theta_w - \theta_r}{\theta_{max} - \theta_r}. \quad (5.14)$$

A plot of Equation (5.13) as a function of θ is presented in Figure 7.2 along with the hydraulic gradient, $\partial \theta_w / \partial \psi$ used in Equation (5.11).

In a layered system, the average hydraulic conductivities $K_{i-1/2}$ and $K_{i+1/2}$ found in Equations (5.7), (5.9) and (5.10) equal

$$\begin{aligned} K_{i-1/2} &= \frac{K_i K_{i-1} \Delta z_i \Delta z_{i-1}}{K_i \Delta z_{i-1} + K_{i-1} \Delta z_i} \\ K_{i+1/2} &= \frac{K_i K_{i+1} \Delta z_i \Delta z_{i+1}}{K_i \Delta z_{i+1} + K_{i+1} \Delta z_i}. \end{aligned} \quad (5.15)$$

Their derivatives with respect to the pressure head are of the general form

$$\begin{aligned} \frac{\partial K_{i-1/2}}{\partial \Psi_{i-1}} &= \frac{\partial K_{i-1/2}}{\partial K_{i-1}} \frac{\partial K_{i-1}}{\partial w_{i-1}} \frac{\partial w_{i-1}}{\partial \theta_{w_{i-1}}} \frac{\partial \theta_{w_{i-1}}}{\partial \Psi_{i-1}} \\ \frac{\partial K_{i-1/2}}{\partial \Psi_i} &= \frac{\partial K_{i-1/2}}{\partial K_i} \frac{\partial K_i}{\partial w_i} \frac{\partial w_i}{\partial \theta_{w_i}} \frac{\partial \theta_{w_i}}{\partial \Psi_i} \\ \frac{\partial K_{i+1/2}}{\partial \Psi_{i+1}} &= \frac{\partial K_{i+1/2}}{\partial K_{i+1}} \frac{\partial K_{i+1}}{\partial w_{i+1}} \frac{\partial w_{i+1}}{\partial \theta_{w_{i+1}}} \frac{\partial \theta_{w_{i+1}}}{\partial \Psi_{i+1}} \\ \frac{\partial K_{i+1/2}}{\partial \Psi_i} &= \frac{\partial K_{i+1/2}}{\partial K_i} \frac{\partial K_i}{\partial w_i} \frac{\partial w_i}{\partial \theta_{w_i}} \frac{\partial \theta_{w_i}}{\partial \Psi_i} \end{aligned} \quad (5.16)$$

The problem is now fully developed and comparisons may be made between the model predictions and actual field measurements.

5.1.4 Model Validation

As for the soil temperature model verification, we used data from the SWOE program to validate the model. The specific locations are Grayling, MI, and Yuma, AZ. In both cases, soil moisture by percent weight measurements were taken essentially once a day. Researchers at CRREL (Cold Regions Research and Engineering Laboratory) and WES (Waterways Experiment Station) made independent measurements. The results for Grayling, MI, are shown in Figure 5.3. The percent weight measurements were converted to volumetric soil moisture values to be consistent with the model output. In doing so, we assumed a soil density of 1.49 g/cm^3 . Also for the Grayling comparisons, an initial surface soil moisture of $0.05 \text{ m}^3/\text{m}^3$ was assumed based on the measured data. The model

calculations are well within the spread of the measurements and respond to precipitation events as seen in Figure 5.3. Soil parameters were chosen to obtain the best fit.

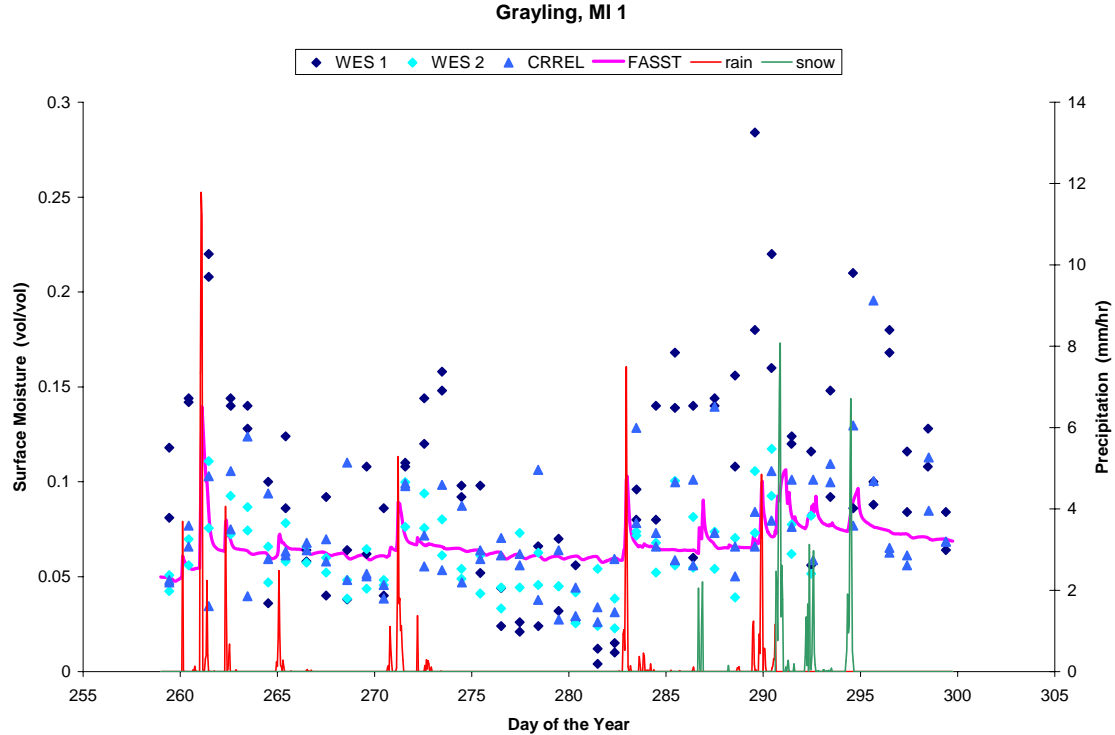


Figure 5.3 Soil moisture comparisons for Grayling, MI, 1992.

We used the CRREL daily measurement for Yuma, AZ, taken on day 74, the first day of the experiment, to initialize the surface soil moisture content. The moisture content at depth was initialized using the procedure discussed in Chapter 11, Section 11.2. The soil is user-specified SM, or silty sand. Overall, the model does fairly well predicting the soil moisture, as can be seen in Figure 5.4. It is certainly within the measurement error of the probes used by WES and CRREL. The daily fluctuations are due to changes in evaporation/condensation.

Since no specific soil type except for sand was recorded for Grayling, we investigated the effect of soil type on the moisture content. As with the surface temperature data, there were only small differences in the model results for the different soil types as seen in Figure 5.5. Unlike the saturated hydraulic conductivity values used to generate the results shown in Figures 5.3 and 5.4, the default values used to generate the results in Figure 5.5 are much smaller and, therefore, no daily oscillations are observed. In all the figures, it is evident that soil moisture measurements are inexact, with as much as a 10% difference exhibited on a given day.

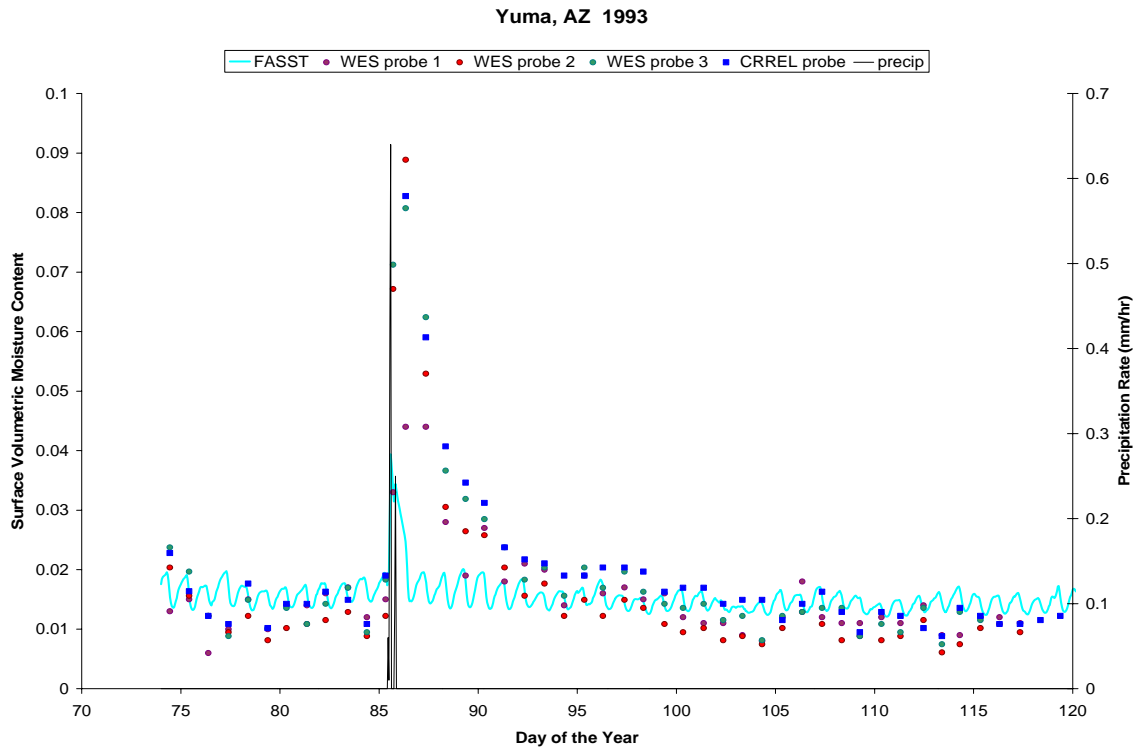


Figure 5.4 Soil moisture comparisons for Yuma, AZ.

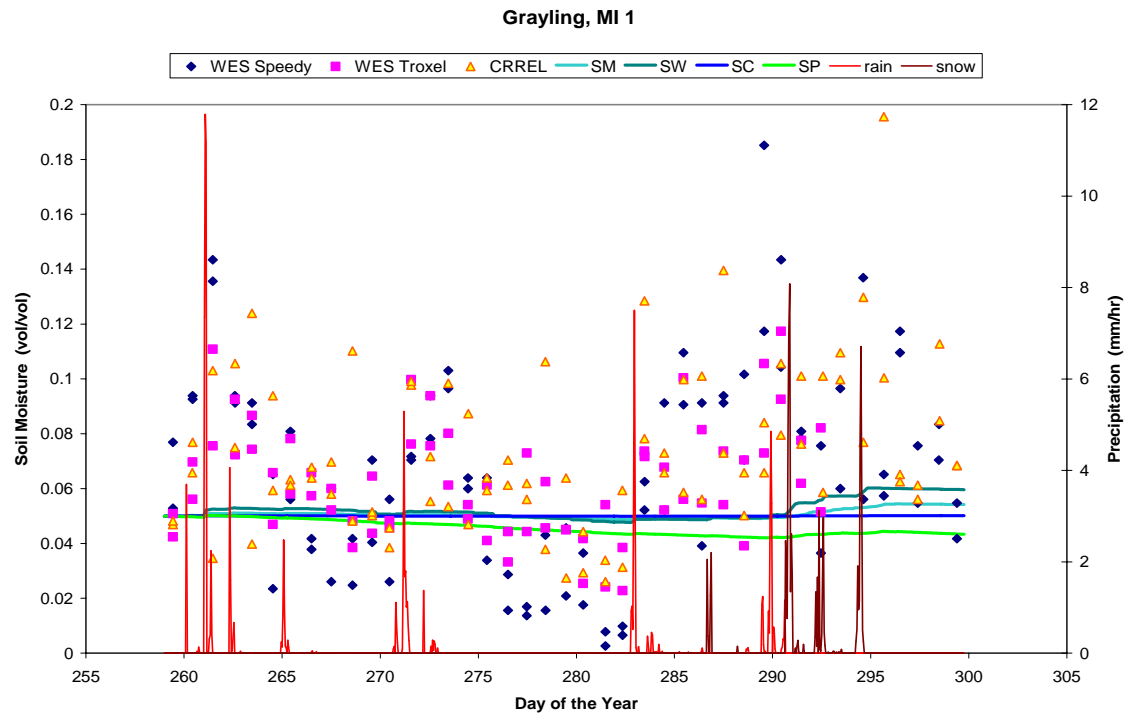


Figure 5.5 Investigation of soil type on soil moisture for Grayling, MI, 1992.

5.2 Soil Strength

The soil strength module was developed for the Soil Moisture Strength Prediction Model Version II (SMSPII). The original documentation is found in Sullivan et al. (1997). Section 7.2.1 is a paraphrase of pages 32–33 and 75–76 of the aforementioned report.

5.2.1 Theory

Historically, cone index (CI) as measured with a standard WES (USA Corps of Engineers Waterways Experimental Station) cone penetrometer, has been used to predict the strength of a soil in establishing vehicle–terrain interaction relationships. The cone index is a measure of the resistance to penetration developed by the cone as it is pushed into the soil. It equals the vertical force applied to the sleeve divided by its surface area. The WES cone has a 30° apex angle with a 0.5-in.² base area that is connected to a circular shaft of 3/8-in. diameter.

The rating cone index (RCI), on the other hand, has been used to represent the proportion of the original soil strength retained after vehicles have passed over the area. The rating cone index is the cone index multiplied by the remolding index (RI) of the soil where the RI equals the ratio of the after-to-before CI values of a soil subjected to a remolding test. The first step of the remolding test is to obtain an undisturbed soil sample using a trafficability sampler. This sample is then placed in a cylinder where the cone penetrometer tests are performed. Measurements are taken at 1-in. intervals. After placing the soil in the cylinder, the sample is subjected to 100 blows with a 2.5-lb hammer, 12-in. fall per blow. A second cone penetrometer test is performed and the resulting RI is defined as the ratio of the average CI value after the 100 blows to that of the CI value before the blows.

Most soils have a minimum strength that will permit a vehicle to complete a specified number of passes over it. This value is referred to as the vehicle cone index (VCI). Insufficient soil strength may cause wheeled and tracked vehicles to become immobilized if the in-situ CI or RCI is less than the VCI required for a specified number of vehicle passes.

Soil strength depends not only on the soil type, but also on the soil moisture. To help quantify the relation between soil strength and moisture, over 1000 field and laboratory tests were performed on samples collected from the United States and elsewhere. Except for gravels and peat, the resulting curve fits for the different USCS soils are

$$\begin{aligned} CI &= \exp[c_1 - c_2 \ln(MC)] \\ RCI &= \exp[c_1 - c_2 \ln(MC)] \end{aligned} \tag{5.17}$$

where c_1 and c_2 are given in Table 7.2.1 below and MC (%) is the soil moisture content by weight, $MC = \theta(\rho_w / \rho_s) \cdot 100\%$, and ρ_s is the soil density. The cone index and rating cone index for gravels is 300, the maximum soil strength allowed. Peat is assumed to have no strength.

The above analysis of soil strength assumes that the soil is not frozen. Cold regions soil conditions present unique difficulties in characterizing the trafficability of soil. A cone index for a soil with a surface frost of 1–2 cm is irrelevant because the high CI obtained is indicative of the difficulty in penetrating the frozen soil with a handheld instrument. It is not necessarily a measure of the bearing capacity of the soil for vehicles or repeated foot traffic. Similarly, the trafficability of a soil with a thawed layer is dependent as much on thaw depth as it is on the CI of the thawed soil. A thaw layer so shallow that personnel or vehicles sink through it to the underlying supportive frozen ground need not be detrimental to mobility, despite the fact that the surface soil has a low CI. Another complication is that because an average CI for the top 15 cm of soil is standard in mobility applications, the bearing capacity of a thaw layer less than 15 cm deep will be misrepresented by the standard CI.

Table 5.2.1 Default Soil Strength Coefficients.

Soil Type	CI Coeff. c_1	CI Coeff. c_2	RCI Coeff. c_1	RCI Coeff. c_2
GW				
GP				
GM				
GC				
SW	3.987	0.81500	3.987	0.8150
SP	3.987	0.81500	3.987	0.8150
SM	8.749	-1.1949	12.542	-2.955
SC	9.056	-1.3566	12.542	-2.955
ML	10.225	-1.565	11.936	-2.407
CL	10.998	-1.848	15.506	-3.530
OL	10.977	-1.754	17.399	-3.584
CH	13.816	-5.583	13.686	-2.705
MH	12.321	-2.044	23.641	-5.191
OH	13.046	-2.172	12.189	-1.942
PT				
SMSC (MC)	9.056	-1.3566	12.542	-2.955
CLML (CM)	9.454	-1.3850	14.236	-3.137
EV	3.987	0.81500	3.987	0.8150
CO, AS, RO, SN				

Sullivan et al. (1997), p. 33 and 34

Despite these difficulties, information highly relevant to trafficability can be obtained from FASST based on the predicted frost and thaw depths and the volume of meltwater produced by the snow. The presence of 5 cm of frost at the surface will usually allow unlimited cross-country operation if, when unfrozen, the soil is not extremely difficult to traverse (Richmond 1991). Therefore, when FASST predicts a frost depth of at least 5 cm in a soil that is predominantly silt or sand, the associated pseudo-CI is 300, the maximum strength allowed. If the terrain is normally untrafficable, then a frost depth of 50 cm is needed in order that most vehicles do not break through the frost layer (Richmond et al. 1995). For clays and peat with predicted frost depths of at least 50 cm, the pseudo-CI is 300.

A finer resolution of bearing capacity when frozen soil overlies incompetent soil has been formulated by Shoop (1995). The minimum frost depth to prevent breakthrough is expressed in terms of the vehicle class (for example, 1 person = 0.1, pickup truck = 4, 5-ton truck = 12, and a D7H tractor = 25 [Shoop 1995 and <http://155.217.58.58/cgi-bin/atdl.dll/fm/3034.343/appb.htm>]), which is the military load classification for bridge and highway limits. It can be approximated using the gross weight of the vehicle (or group of people) in tons. For wet soil beneath the frozen layer, the relation is

$$z_{wet} = 0.10\sqrt{vehicle\ class} \quad (5.18)$$

and for dry soil the relationship is

$$z_{dry} = 0.16\sqrt{vehicle\ class} \quad (5.19)$$

where z (m) is the frost depth.

Another contribution of FASST to trafficability is a quantification of the amount of water available to infiltrate thawed soil from a melting snow cover. Once the wetness of the thawed layer is known, FASST can assess the bearing capacity of the thawed layer as if it were an infinitely thick layer (ignoring the underlying frozen soil). If the bearing capacity of the soil that forms the thawed layer is high, then the presence of the thawed layer is largely irrelevant. If the bearing capacity of the thawed layer is low or moderate, then its thickness must be considered in determining its impact on trafficability.

Finally, FASST outputs a “slippery factor” that tells the mobility model whether the surface is dry, wet, snow covered, or ice covered.

5.3 References

Guymon, G.L., R.L. Berg, and T.V. Hromadka (1993) Mathematical Model of Frost Heave and Thaw Settlement in Pavements. U.S. Army Cold Regions Research and Engineering Laboratory, CRREL Report 93-2.

Jordan, R. (2000) User’s Guide for USACRREL One-Dimensional Coupled Soil and Snow Model (SLTHERM).

Richmond, P.W. (1991) Notes for Cold Weather Military Operations, U.S. Army Cold Regions Research and Engineering Laboratory, Special Report 90-30 (with excerpts from U.S. Army Field Manual FM 90-13/FM 7-26, *Ice Bridging*, p. B-20).

Richmond, P.W., S.A. Shoop, and G.L. Blaisdell (1995) Cold Regions Mobility Models. U.S. Army Cold Regions Research and Engineering Laboratory, CRREL Report 95-1.

Shoop, S.A. (1995) Vehicle Bearing Capacity of Frozen Ground Over a Soft Substrate, *Canada Geotechnical Journal*, V. 32, p. 552–556.

Sullivan, P.M., C.D. Bullock, N.A. Renfroe, M.R. Albert, G.G. Koenig, L. Peck, and K. O'Neill (1997) Soil Moisture Strength Prediction Model Version II (SMSPII). U.S. Army Corps of Engineers Waterways Experiment Station, Technical Report GL-97-15.

van Genuchten, M. Th. (1980) A Closed-Form Equation for Predicting the Hydraulic Conductivity of Unsaturated Soils. *Soil Science Society of America Journal*, V. 44, p. 892–898.

Yu, C. Loureiro, J.-J. Cheng, L.G. Jones, Y.Y. Wang, Y.P. Chia, and E. Faillace (1993) Data Collection Handbook to Support Modeling Impacts of Radioactive Material in Soil. Environmental Assessment and Information Sciences Division, Argonne National Laboratory, Argonne, Illinois (www.ead.anl.gov/resrad/datacoll/dcall.htm).

Chapter 6

Ground State Model

6.0 Introduction

The goal of the Ground State Module is to provide a very simple formulation and very rapid calculation of freezing and thawing that still accounts for fundamental mechanisms and conditions in individual cases. The overall strategy is to use simple flux balance relations to evaluate the interface temperatures in terms of energy input and medium properties; to then use those temperatures to express the fluxes; and then use fluxes at depth to express rate of freeze or thaw. This rate, multiplied by the time step, then gives the depth of freeze or thaw. This depth of freeze or thaw can be continuous or discontinuous, depending on the temperature and moisture profiles of the soil.

6.1 Physical Setup

The phase change process is assumed to be isothermal. The main principle behind the freeze–thaw model is to compare the energy needed to freeze or thaw the soil to that available at a given depth as was done by Guyman et al. (1993). Partial freezing or thawing can occur. If the ice content at a given node is greater than zero, the node is assumed frozen for the purposes of calculating the thickness of the frozen soil layer.

The energy extracted (freezing) or available (thawing) at a node (J/m^3) during a time step can be expressed as

$$\text{node energy} = \Delta Q_1 = |T_i - 273.15| \sum \theta_k \rho_k c_{p_k} \quad (6.1)$$

where T_i is the node temperature (K), and the subscript k is for the soil components dirt, water, ice and air, θ_k is the volume fraction of component k , ρ_k (kg/m^3) is the density of component k , and c_{p_k} (J/kg) is the specific heat of component k . Calculation of T_i is discussed in Chapter 4. Determination of the various volume fractions is discussed in Chapter 5.

The energy remaining before the node can completely freeze or thaw (J/m^3) is defined as

$$\begin{aligned} \text{freeze energy} &= \Delta Q_2 = l_{fus} (\theta_w - \theta_r) \sum \theta_k \rho_k c_k \\ \text{thaw energy} &= \Delta Q_2 = -l_{fus} \theta_i \sum \theta_k \rho_k c_k \end{aligned} \quad (6.2)$$

where l_{fus} is the latent heat of fusion of water ($3.335 \times 10^5 J/kg$) and θ_r is the node residual volumetric water content as discussed in Chapter 7. Freezing can occur only if the node $T_i \leq 273.15 K$ and thawing if $T_i > 273.15 K$.

The change in volumetric ice content per time step is therefore

$$\Delta \theta_i = \frac{\rho_w}{\rho_i} \frac{\min(\Delta Q_1, |\Delta Q_2|)}{l_{fus}} \quad (6.3)$$

and the nodal volumetric soil moisture and ice contents are updated accordingly.

6.2 Validation

We tested the freeze/thaw module using the data collected by Lindamae Peck in South Royalton, VT, spanning the winter of 1990–1991 (personal communication). The site had silty soil of which the density, porosity, and thermal conductivity had been measured (Peck and O’Neill 1997). Figure 8.1 compares the frost depth as extrapolated from the thermister probe to those calculated by FASST. FASST was initialized with two soil layers, the top one a silty sand (SM) 0.10 m thick and the bottom layer an organic silty clay (OL) 1.40 m thick. The FASST determined surface temperature denoted “st FASST” is also shown in Figure 8.1. The largest differences between the calculations and the measurements occur during the thawing period. FASST partially thaws a few days before the measured values. This is in part due to differences in the snow meltout date between the model and the observations as discussed below. Shifting of the surface probe during the winter is also to blame.

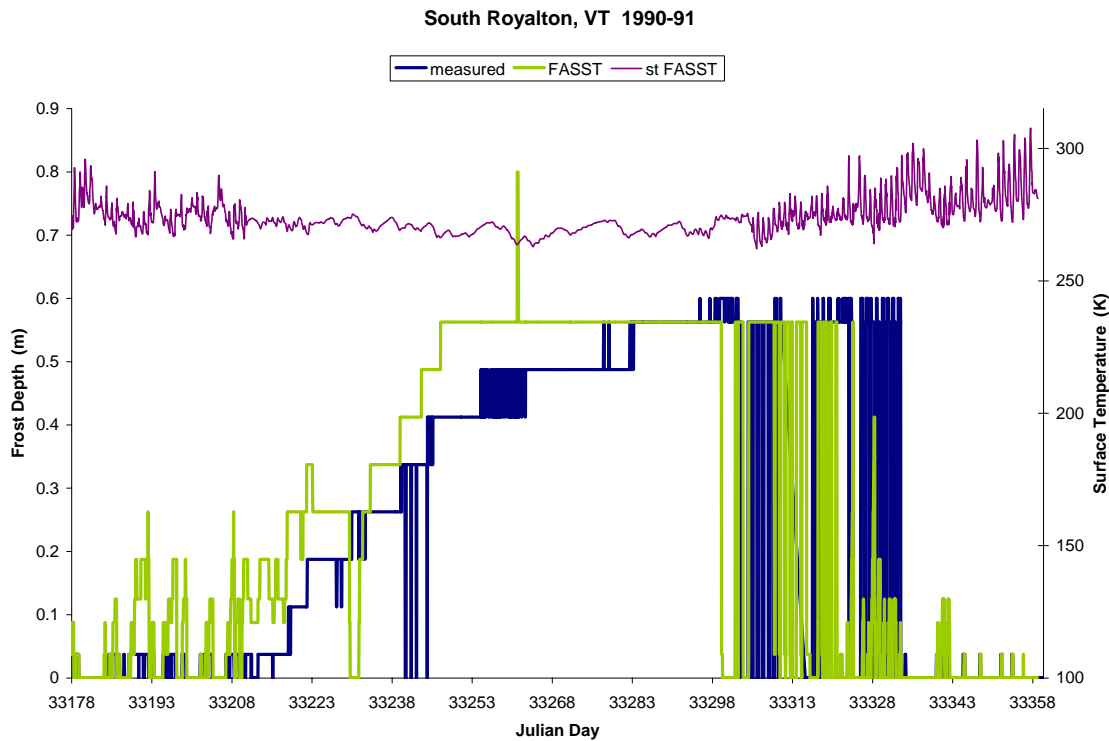


Figure 6.1 Comparison of frost depth between FASST and measured values for South Royalton, VT.

Figure 6.2 shows that several daily shallow freeze/thaw events happen before and after the first snow. This is a common occurrence in temperate climates. From Figure 6.2 one can also discern that when there is snow present (measured values), FASST accurately predicts the frost depth. Differences between FASST and measured values can be due to the thermister string spacing. Another reason could be how “frozen soil” is defined between the two. FASST considers a node frozen if there is any ice present while the measured value is strictly defined by temperature. FASST does a fairly good job at

predicting frost depth, especially their occurrence and under a snow cover. It also does a good job at reproducing the diurnal freeze/thaw cycles that occur in the spring and fall. These are very important to mobility considerations as they result in slippery surface conditions.

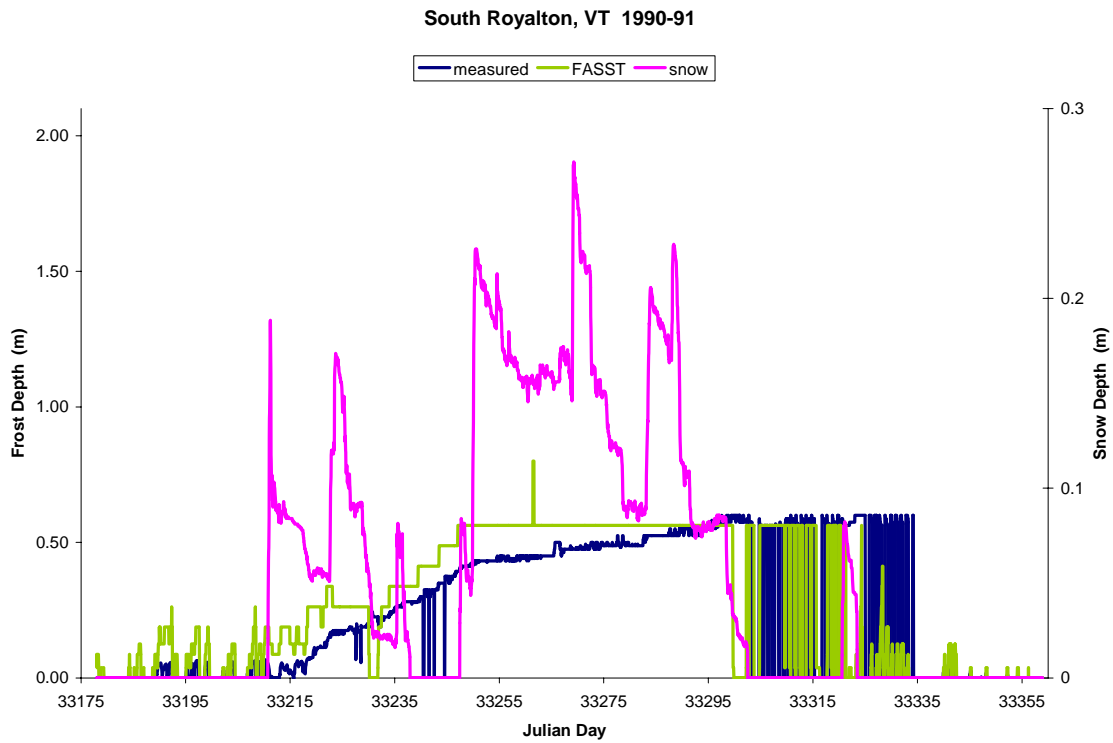


Figure 6.2 Comparison of FASST calculated frost depth and measured values as a function of soil depth and snow depth.

6.3 References

Guyman, G.L., R.L. Berg, and T.V. Hromadka (1993) Mathematical Model of Frost Heave and Thaw Settlement in Pavements. U.S. Army Cold Regions Research and Engineering Laboratory, CRREL Report 93-2.

Peck, L. and K. O'Neill (1997) Frost Penetration in Soil with an Inclusion of Sand: Dependence on Soil Moisture Content and Winter Severity, *Canadian Geotechnical Journal*, V. 34, No. 3, p. 368–383.

Chapter 7

Snow Accretion, Depletion, and Meltwater Outflow Model

7.0 Introduction

The Snow Accretion-Depletion Module uses the Snowmelt Numerical Analysis Package (SNAP) developed by Albert and Krajewski (1998). It is a physically based approach to modeling snowmelt, where the physics of flow through snow are considered and the melt is driven by an energy budget at the snow surface. Snow accretion occurs when a snowfall amount is given in the input or when precipitation is given in the input and the input air temperature is below freezing. In the latter case, the precipitation amount is converted to a snowfall amount. Sections 7.1 and 7.2 are from Albert and Krajewski (1998).

7.1 Governing Equations of Flow within the Snow

For modeling the movement of water through the snow, the effects of capillarity are taken as negligibly small compared to the effects of gravity (Colbeck 1972), yielding the simplified form of Darcy's equation:

$$U = \frac{\rho_w k_w g}{\eta_w} \quad (7.1)$$

where U is the volume flux of water, ρ_w is the density of water, k_w is the relative permeability to water, g is the acceleration of gravity, and η_w is the viscosity of water. Under some circumstances this will be applicable to the entire snowpack, while modifications will be necessary under some conditions of layering. The effective permeability of the water phase is taken to be proportional to a power (n_c) of the effective water saturation (Morel-Sayoux 1969, Colbeck 1972):

$$k_w = k_{w0} S_e^{n_c} \quad (7.2)$$

where the effective water saturation, S_e , is defined by

$$S_e = \frac{S_{wa} - S_{wi}}{1 - S_{wi}} \quad (7.3)$$

where S_{wa} is the absolute water saturation and S_{wi} is the irreducible water saturation. The general applicability of the relationship $k_w \propto S_e^{n_c}$ is discussed in Maulem (1978). Here, n_c is taken as a constant with a default value of 3.3.

The flux in terms of absolute water saturation is defined as

$$U = \frac{\rho_w k_{w0} g}{\eta_w} S_e^{n_c}. \quad (7.4)$$

The water volume conservation equation (Colbeck 1972) used states that the change in water volume flux with depth, U' (where the z axis is positive downwards), is equal to the change in water saturation with time:

$$U' + \phi(1 - S_{wi})\dot{S}_e = 0 \quad (7.5)$$

where ϕ is the total pore volume as a function of the total volume. Changes in S_{wi} occur on a much larger time scale than changes in effective saturation, hence it is sufficient to consider S_{wi} constant over an individual time step (although it can be altered through the course of the snowmelt season). To obtain an analytical expression that can easily be employed in a computer model, the solution of these equations differs from earlier solutions (Colbeck 1972, Tucker and Colbeck 1977) in that Equation (7.4) is used to find \dot{S}_e as a function of U , which is then substituted into Equation (7.5) above, to give the governing equation for water volume flux

$$\dot{U} = -n_c \phi^{-1} (1 - S_{wi})^{-1} \left(\frac{\rho_w k_{w0} g}{\eta_w} \right)^{\frac{1}{n_c}} U^{\left(1 - \frac{1}{n_c}\right)} U'. \quad (7.6)$$

In order to make the problem tractable, n_c , ϕ , S_{wi} , and k_{w0} are assumed to be constant over each time step. These variables change slowly compared to the time scale with which mobile water moves through the snow. By simplifying notation as follows

$$\kappa_{cf} = n_c \phi^{-1} (1 - S_{wi})^{-1} \left(\frac{\rho_w k_{w0} g}{\eta_w} \right)^{\frac{1}{n_c}} \quad (7.7)$$

and

$$\eta_{cf} = 1 - \frac{1}{n_c}, \quad (7.8)$$

the flux governing equation becomes

$$\dot{U} = -\kappa_{cf} U^{\eta_{cf}} U'. \quad (7.9)$$

This equation is solved using separation of variables. The general solutions to the volume flux equation are therefore sums in space and time of particular solutions governed by boundary conditions while maintaining the restrictions indicated above. It is not necessary to completely solve the volume flux equation, as a temporal expansion of particular solutions will tend to approximate the exact solution if the particular solutions are generated near enough to each other in time. With each separate particular solution being generated by meteorological data in separate time steps, the accuracy of the solution will be dependent on the time step of the available meteorological data, with hourly data proving accurate enough to give promising results, and finer resolution data resulting in more accurate approximations of the exact solution.

Equation (7.9) is solved by assuming the solutions take the form

$$U(x, t) = B(x + c_1)^{\alpha_{cc}} (t + c_2)^\beta \quad (7.10)$$

where substitution back into Equation (7.9) and re-grouping gives

$$\beta(x + c_2)^{\alpha_{cc}} (t + c_2)^{\beta-1} = -\kappa_{cf} B^{\eta_{cf}} \alpha_{cc} (x + c_1)^{\alpha_{cc}\eta_{cf} + \alpha_{cc}-1} (t + c_2)^{\beta\eta_{cf} + \beta}. \quad (7.11)$$

For this to hold

$$\alpha_{cc} = \frac{1}{\eta_{cf}} \quad (7.12)$$

$$\beta = -\frac{1}{\eta_{cf}} \quad (7.13)$$

$$B = \kappa_{cf}^{\frac{1}{\eta_{cf}}} \quad (7.14)$$

implying the solution must have the form

$$U(x, t) = \kappa_{cf}^{-1/\eta_{cf}} (x + c_1)^{1/\eta_{cf}} (t + c_2)^{-1/\eta_{cf}}. \quad (7.15)$$

Co-ordinates are then normalized by defining

$$\chi = x + c_1 \quad (7.16)$$

$$\tau = t + c_2 \quad (7.17)$$

thus giving

$$U(\chi, \tau) = \left(\frac{\chi}{\kappa_{cf} \tau} \right)^{1/\eta_{cf}}. \quad (7.18)$$

In the normalized co-ordinates (χ, τ) , each particular solution represents a wave of volume flux with its origin at the point $(\chi = 0, \tau = 0)$. In other words, each differential element of mobile water, dA_m , generates its own particular solution where $\tau = 0$ occurs at the time the water volume becomes mobile within the snow (surface melt or rainfall), and $\chi = 0$ occurs at the vertical height of the snowpack at the time the water volume becomes mobile.

To find the depth of penetration of a wave as a function of time is simply a matter of integrating saturation from the point of generation of the wave to whatever depth necessary to allow the total volume enclosed by the integration to be equal to the original volume of the wave. For an input volume per unit area of A (cm) over an area σ_{wa} , if the depth of penetration of the resulting flux wave is denoted as x_U , then at any point τ in time

$$\int_{\chi=0}^{\chi=x_U} S_e \phi(1 - S_{wi}) \sigma_{wa} d\chi = A \sigma_{wa} \quad (7.19)$$

where A is the volume/unit area runoff in cm and σ_{wa} is the area. Therefore we have

$$\int_{\chi=0}^{\chi=x_U} S_e d\chi = \frac{A}{\phi(1 - S_{wi})}. \quad (7.20)$$

Using S_e from Equation (7.4) and U from Equation (7.18), substituting into Equation (7.20), then solving the integral yields the equation for the depth of penetration of a wave as a function of time

$$x_U = \left(\frac{A}{\eta_{cf} \phi(1 - S_{wi})} \right)^\eta \left(\frac{\rho_w k_{w0} g}{\eta_w} \right)^{\eta_{cf} - \eta_{cf}^2} (\kappa_{cf} \tau)^{1 - \eta_{cf}}. \quad (7.21)$$

Next, consider the time it will take a wave of volume flux to penetrate to a given depth (most useful in calculating the delay between influx and outflux). In order for the water mass to balance in time, the volume of water passing by a given depth D must equal the initial mobile water volume

$$\int_{\tau=\tau_0}^{\tau=\infty} U(D, \tau) d\tau = A_m. \quad (7.22)$$

Substituting from Equation (7.15) yields

$$\int_{\tau=\tau_0}^{\tau=\infty} \kappa_{cf}^{\frac{-1}{\eta_{cf}}} D^{\frac{1}{\eta_{cf}}} \tau^{\frac{-1}{\eta_{cf}}} d\tau = A_m \quad (7.23)$$

where D is the depth of penetration at time τ_0 .

The solution to this integral gives the time required for a wave of volume flux to penetrate to depth D

$$\tau_0 = \left(\frac{1 - \eta_{cf}}{\eta_{cf}} A_m \left(\frac{\kappa_{cf}}{D} \right)^{\frac{1}{\eta_{cf}}} \right)^{\frac{\eta_{cf}}{\eta_{cf}-1}}. \quad (7.24)$$

For modeling purposes, note that Equation (7.21) may also be written in the simpler form

$$x_U = \kappa_{cf} \left(\frac{n_c - 1}{A} \right)^{\frac{1-n_c}{n_c}} \tau^{\frac{1}{n_c}}. \quad (7.25)$$

Having depth of penetration as a function of time, and vice versa, requires only that the effects of preceding flux waves be incorporated in order to construct a working model of water movement through homogeneous snow. Therefore, consider two flux waves, each proceeding according to Equation (7.18)

$$U_1(\chi_1, \tau_1) = \left(\frac{\chi_1}{\kappa \tau_1} \right)^{\frac{1}{\eta_{cf}}} \quad (7.26)$$

and

$$U_2(\chi_2, \tau_2) = \left(\frac{\chi_2}{\kappa_{cf} \tau_2} \right)^{\frac{1}{\eta_{cf}}}. \quad (7.27)$$

Assume that $\chi_1 - \chi_2 = \varepsilon > 0$ (that the wave U_1 began at an earlier point in time than the wave U_2). Since there is no singularity within the region over which the U_2 solution applies, flux will be continuous and differentiable over this region, up to the singularity caused by the $U_1 - U_2$ junction. As the U_2 wave flows through the snow, Equation (7.25) must always be met, even as new water volume is absorbed into wave U_2 from the residual saturation of wave U_1 . Therefore, to accommodate the new water volume the second wave has encountered while still maintaining its solution to the conservation and flux-saturation equations, the volume flux wave U_2 must travel deeper into the snowpack than it otherwise would, thereby encountering more residual saturation in the process. Numerically, the residual saturation encountered will take the form

$$S_1 = \left[\frac{\eta_w}{\rho_w k_{w0} g} \right]^{\frac{1}{n_c}} U_1^{\frac{1}{n_c}} \quad (7.28)$$

which, when combined with U_1 from Equation (7.26), becomes

$$S_1 = \left[\frac{\eta_w}{\rho_w k_{w0} g} \right]^{\frac{1}{n_c}} \left(\frac{\chi_1}{\kappa_{cf} \tau_1} \right)^{\frac{1}{\eta_{cf}}}, \quad (7.29)$$

which means that if x_{A2} is the deepest point within the snow at which the U_2 solution applies, (the point of the singularity), then the volume of water absorbed by the U_2 wave in moving some infinitesimal distance through the snow will be given by

$$\partial A_2 = \phi(1 - S_{wi}) \left[\frac{\eta_w}{\rho_w k_{w0} g} \right]^{\frac{1}{n_c}} \left(\frac{x_{A2}}{\kappa_{cf} \tau_1} \right)^{\frac{1}{\eta_{cf}-1}} \partial x_{A2}. \quad (7.30)$$

Therefore, as found before, (derived with constant volume, but still applicable with a time varying volume),

$$x_{A2}(\tau_2) = \kappa_{cf} \left(\frac{n_c - 1}{A_2} \right)^{\frac{1-n_c}{n_c}} \tau_2^{\frac{1}{n_c}} \quad (7.31)$$

where now A_2 is a function of time. Therefore, define a constant A_{II} equal to the initial mobile water volume of the U_2 wave, and a new variable Δ_2 equal to the total water volume the U_2 wave has absorbed, by the equation

$$A_2 = A_{II} + \Delta_2 \quad (7.32)$$

where we know that because the U_1 wave is undisturbed beneath the $U_1 - U_2$ junction, the total water volume below the junction must be the same as it would be were the U_2 wave not present, giving rise to the conclusion that the total water volume above the $U_1 - U_2$ junction must be equal to the initial volume of the U_2 wave plus the volume of the U_1 wave, which would not otherwise have passed the $U_1 - U_2$ junction point. This means that

$$\Delta_2 = \left[\frac{x_{A2}}{\kappa_{cf}} \right]^{\frac{n_c}{n_c-1}} (n_c - 1) \tau_1^{\frac{1}{1-n_c}}. \quad (7.33)$$

By substituting into Equation (7.32) we get

$$x_{A2}(\tau_2) = \kappa_{cf} \left(\frac{n_c - 1}{A_{II} + \left[\frac{x_{A2}}{\kappa_{cf}} \right]^{\frac{n_c}{n_c-1}} (n_c - 1) (\tau_1)^{\frac{1}{1-n_c}}} \right)^{\frac{1-n_c}{n_c}} \tau_2^{\frac{1}{n_c}}, \quad (7.34)$$

which can be solved for x_{A2}

$$x_{A2} = \kappa_{cf} \tau_2^{\frac{1}{n_c}} \left(\frac{A_{II}}{n_c - 1} \right)^{\frac{n_c-1}{n_c}} \left[1 - \left(\frac{\tau_2}{\tau_1} \right)^{\frac{1}{n_c-1}} \right]^{\frac{1-n_c}{n_c}}. \quad (7.35)$$

This is the form used in the model to find the depth of any wave that has a preceding wave. Finding the point at which one wave of volume flux completely overtakes its antecedent proves to be straightforward if the first wave has no predecessor, with the result being

$$\tau_2 = \delta \left[\left(\frac{A_{II}}{A_I} + 1 \right)^{\frac{1}{n_c-1}} - 1 \right]^{-1} \quad (7.36)$$

where δ is the time between the formation of wave U_1 and wave U_2 . This gives us the ability to calculate the flux as a function of depth and time resulting from a single water volume input, to calculate the depth and net water volume of a following input wave of volume flux, and to calculate the depth and time at which one wave of volume flux will overrun a preceding wave of volume flux. In short, it is now possible to completely describe the saturation and flux resulting from two point inputs in several compact equations, without any finite difference or finite element matrix solutions to differential equations. In order to extend the model to the general case in which many waves may be

flowing through the snowpack without allowing time for complete drainage or refreezing between pairs of volume flux waves, however, it is necessary to know the time of collision of a wave of volume flux with its predecessor, which itself is not traveling through new snow. Unfortunately, in the event that there are multiple waves flowing through the snow, no explicit form for the time of collision can be found. Furthermore, no explicit equation for the time a given volume flux will take to reach any given depth can be found. This is not the downfall of the model, however, because, while the equations governing the time of collision between waves are not tractable in general, they are very well behaved, becoming linear very shortly after the generation of the wave. Therefore the snow melt module uses a Newton's method approximation to find the time a given volume flux will take to reach the bottom of the snowpack (and, if necessary, the time of collision of two waves in the general case). This usually takes four or less iterations of the approximating loop to come within $\pm 0.5\%$ of the true value.

The process of water volume flux waves absorbing residual mobile water saturation from the tails of their predecessors (described by Equation [7.36]), which states that any wave will eventually overtake any preceding wave given an infinite time and an infinite snow depth to traverse), although it necessitates the Newton's method approximation above, also leads to the great strength of this model: its computational simplicity. Because waves continually overtake each other on the way to the bottom of the pack, there rarely are very many of them within the snowpack at any given time. The only conditions under which there will be very many waves within the snowpack is when dA_m is low enough, and snow depth is high enough that melt waves take a long time (compared to the time scale) to flow out of the pack, *and* input volume flux is decreasing at a rapid enough rate that waves are not colliding within the snow. Using an hourly time step, and a surface energy balance for melt input, it is rare to see more than three waves within the snow at any one time in the seasonal snow of New England. Any further modeling of flux waves on their way through the pack would not result in any greater accuracy of outflow prediction, as only one wave may actually flow out of the bottom of the pack at any time.

7.2 Evolution of Parameters

While the snow property parameters, such as grain size, k_{w0} , S_{wi} , n_c , and ϕ_e are relatively stable over the usual lifetime of a wave of volume flux, over the lifetime of a snowcover they do vary. Here the parameters are considered as constants in a given time step, yet they may change over the course of the snowmelt season.

7.2.1 Grain Growth

Grain size is currently used only to calculate the permeability of snow. The equations of Brun (1989) are used to calculate average grain volume. The initial volume of the snow crystals is currently taken as 0.00005 cm^3 , which is quickly dwarfed by the growth equations, especially if the snow is wet. Once the average crystal volume in the wet portion of the pack and the average crystal volume in the dry portion of the pack are

calculated, a weighted average of the two is taken as the average crystal volume within the pack.

7.2.2 Permeability

The most exhaustive search published to date for the permeability of snow as a function of grain size and snow density probably comes from the work of Shimizu (1970), in which he considered previous models of snow permeability produced by Bader (1954), Bender (1957), and Kuroiwa (1968), as well as a range of his own tests, and came to the conclusion

$$k_{w0} = 0.077d^2 \exp(-7.8\rho_s) \quad (7.37)$$

where d is the snow grain diameter (cm) and ρ_s is the specific gravity (g/cm^3). In our model, d is computed as

$$d = 2\sqrt[3]{\frac{3}{4\pi}V_{av}} \quad (7.38)$$

where V_{av} is the average crystal volume computed above. ρ_s is taken as the density of frozen water within the snowpack, either as computed in the snow depth prediction routine, or as a constant $0.3\ g/cm^3$ if snow depth is not being computed.

7.2.3 Irreducible Water Saturation

In the FASST snow module, the irreducible water saturation of snow is computed as a fraction of total volume. Kattlemann (1986) reported that Sulahrie (1972) found a value as high as 40% in some cases, while most authors have reported measurements in the range of 0% to 10%.

7.2.4 Snow Depth

Snow depth prediction equations are based on the form used by Jordan (1991a), which in turn come from Anderson (1973). Both SNATHERM.89 (Jordan 1991a) and Anderson's earlier model break the snow into layers based on age, density, and crystal structure, while here the simplicity of a uniform bulk snowpack is maintained. The model predicts the rate of densification, then adjusts the snowdepth accordingly. The equations used are as follows

$$\left. \frac{1}{D_s} \frac{\partial D_s}{\partial t} \right|_{metamorphism} = -2.778 \times 10^{-6} c_1 c_2 \exp[-0.04T] \quad (7.39)$$

where D_s is the depth of snow, t is time (s), T is temperature ($^{\circ}C$), and

$$\begin{aligned} c_1 &= 1 & \rho_i &\leq 0.12 \\ c_1 &= \exp[-46(\rho_i - 0.15)] & \rho_i &\geq 0.12 \end{aligned} \quad (7.40)$$

where ρ_i is the density of water in the frozen state within the snowpack (g/cm^3) and

$$c_2 = 1 + f_l \quad (7.41)$$

where f_l is the fraction of the snowpack which is wet. Further, we have

$$\left| \frac{1}{D_s} \frac{\partial D_s}{\partial t} \right|_{\text{overburden}} = -\frac{\bar{P}_s}{\eta_c} \quad (7.42)$$

where \bar{P}_s is the average load pressure within the snowpack, and η_c is a viscosity coefficient, which has the form

$$\eta_c = \eta_0 \exp(0.08T + 28\rho_t) \quad (7.43)$$

where ρ_t is the total density of the solid and liquid phases of the snow, and $\eta_0 = 5\text{E}+08$.

Also calculated with snow depth are ρ_i (the density of ice within the snowpack), ρ_t (the density of ice plus irreducible water saturation plus mobile water saturation), ϕ (the total pore volume as a fraction of total volume), ϕ_e (pore volume excluding pore volume filled with immobile water when meeting irreducible saturation requirements, as a fraction of total volume), and *SWE* (the snow water equivalent).

7.2.5 Effective Saturation Exponent

The general applicability of the relationship $k_w \propto S_e^{n_c}$ is discussed in depth in Mualem (1978). Since a way to determine n_c from the available meteorological and lysimeter data could not be found, FASST simply uses a constant n_c , and its value is left up to the user, (with a default of 3.3).

7.2.6 Refreezing

The refreezing algorithm uses a time-averaged value of temperature over the most recent period in which the snowpack is predicted to be less than isothermal, and a depth-averaged value of saturation, along with bulk-approximated thermal conductivity of snow, to calculate the depth of penetration of the refreezing front. Since these values are updated every time step, the depth of penetration produced should be accurate enough. An analytical solution of the well-known Neumann type (Carslaw and Jaeger 1959) given by

$$X = \sqrt{\frac{2k_1(T_f - T_s)t}{\rho l_f}} \quad (7.44)$$

where X is the depth of the freezing front, k_1 is the thermal conductivity of the medium in the refrozen state, T_f is the temperature of fusion, T_s is the surface (ambient air) temperature, t is time, ρ is the density of the medium, and l_f is the latent heat of fusion.

k_1 is taken to be $0.0045 \text{ J/s cm}^\circ\text{C}$, which is approximately the thermal conductivity of snow of density 0.3 g/cm^3 . T_f is taken as 0°C , while T_s is taken as the average temperature over the current period of freeze depth propagation. l_f is taken as 333.05 J/g ,

so that the latent heat of fusion of 1 cm^3 of snow that has been drained to S_{wi} will be $l \cdot S_{wi}$. A correction to account for residual mobile water saturation was implemented, but the effects were found to be minimal in light of the fact that the freezing front progresses slowly compared to the speed of water percolation.

7.3 Surface Energy Balance

In generating melt, FASST currently uses a full surface energy balance to calculate the volume of runoff that is generated from surface melt during each time step. In general, the heat input at the top of the snow (I_{top}) is (Jordan 1991a)

$$I_{top} = I_s \downarrow (1 - \alpha) + I_{ir}^\downarrow - I_{ir}^\uparrow + H + L + I_{conv} \quad (7.45)$$

where $I_s \downarrow$ is the net solar radiation at the surface, α is the surface albedo pertinent to shortwave radiation, I_{ir}^\downarrow is the incoming longwave radiation, I_{ir}^\uparrow is the outgoing longwave radiation, H is the sensible heat flux, L is the latent heat flux, and I_{conv} is the convective heat flux. Solar radiation and albedo are currently not estimated in the module, and neither is net longwave radiation, so $I_s \downarrow (1 - \alpha)$ and $(I_{ir}^\downarrow - I_{ir}^\uparrow)$ are taken as inputs to the model. Details of the exchange follow Jordan (1991a, b). The resulting surface melt depth is

$$\Delta h_{i,top} = I_{top} \frac{\Delta t}{\rho_i l_f}. \quad (7.46)$$

If the ground temperature is above freezing, melting can also occur at the bottom of the snow. The bottom melt depth is

$$\Delta h_{i,bottom} = \kappa \frac{\partial T}{\partial z} \frac{\Delta t}{\rho_i l_f} \quad (7.47)$$

where κ is the soil thermal conductivity ($W/m \cdot K$), T is the soil temperature (K), and z is the soil depth (m).

7.4 Module Input and Output

The Snow Accretion/Depletion Module requires certain information about the snow cover. If known, snow depth, snow water equivalent, initial water saturation (default 0.0288), effective porosity, and the snow surface temperature should be input. Otherwise, the module will compute these parameters. The required meteorological data are air temperature, wind speed, net solar radiation, net longwave radiation, and precipitation (amount and type). If the type of precipitation (rain, snow) is not known, it will be predicted based on the ambient air temperature. Net radiation can be obtained using the two radiation modules described in Chapters 4 and 5. The output of the module is snow depth and the volume of water (total and incremental) that has come out of the snowpack.

7.5 Model Validation

To test how well FASST predicts the snow depth, we compared the model results with data gathered during the winter of 1997 in the Sleepers River, VT, watershed and during the winter of 2003 for Buffalo Pass, CO, and Indian River, CO. The latter two data sets are part of NASA's Cold Land Processes Experiment (CLPX). The results for Sleepers River are plotted in Figure 7.1. FASST can run in two modes, one where FASST uses the measured snow depth to self-correct the model predictions ("FASST, Yes") and one where only initial snow depth is provided ("FASST, No"). The relative errors are 1% and 7%, respectively, both well within the accepted accuracy standard of 15% (Holcombe et al. 2004). It can also be seen in Figure 7.1 that, for the most part, increases in snow depth are accompanied by precipitation events. Increases in the measured values not associated with snowfall are the result of blowing snow. FASST does not account for this at present.

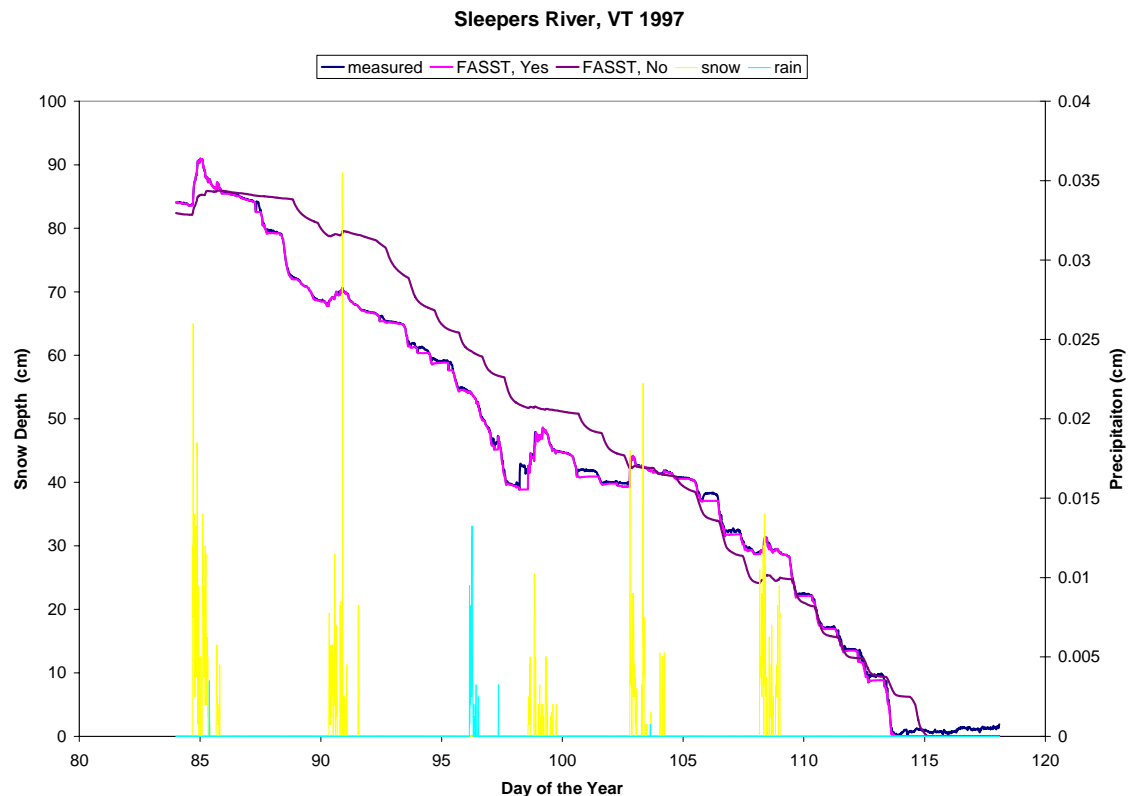


Figure 7.1 Comparison between the measured snow depth and the snow depth calculated by FASST along with snow (yellow) and rain (blue) precipitation events for Sleepers River, VT.

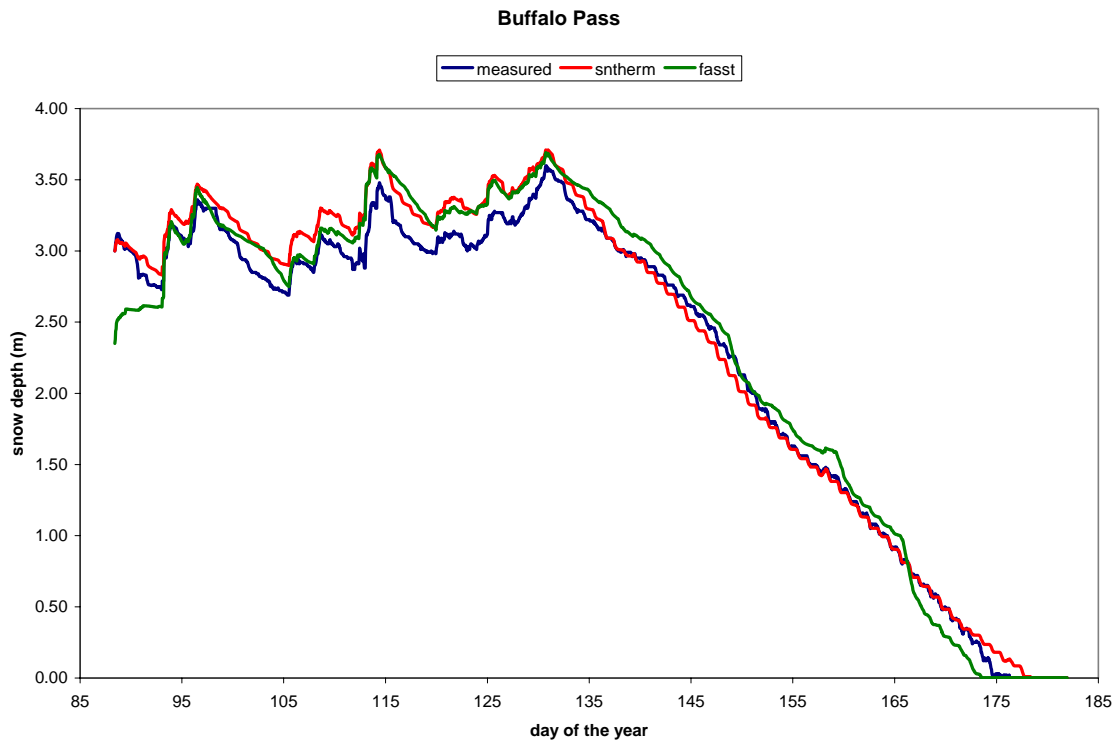


Figure 7.2 Comparison between the measured snow depth and the snow depth calculated by SNTHERM and FASST for Buffalo Pass, CO.

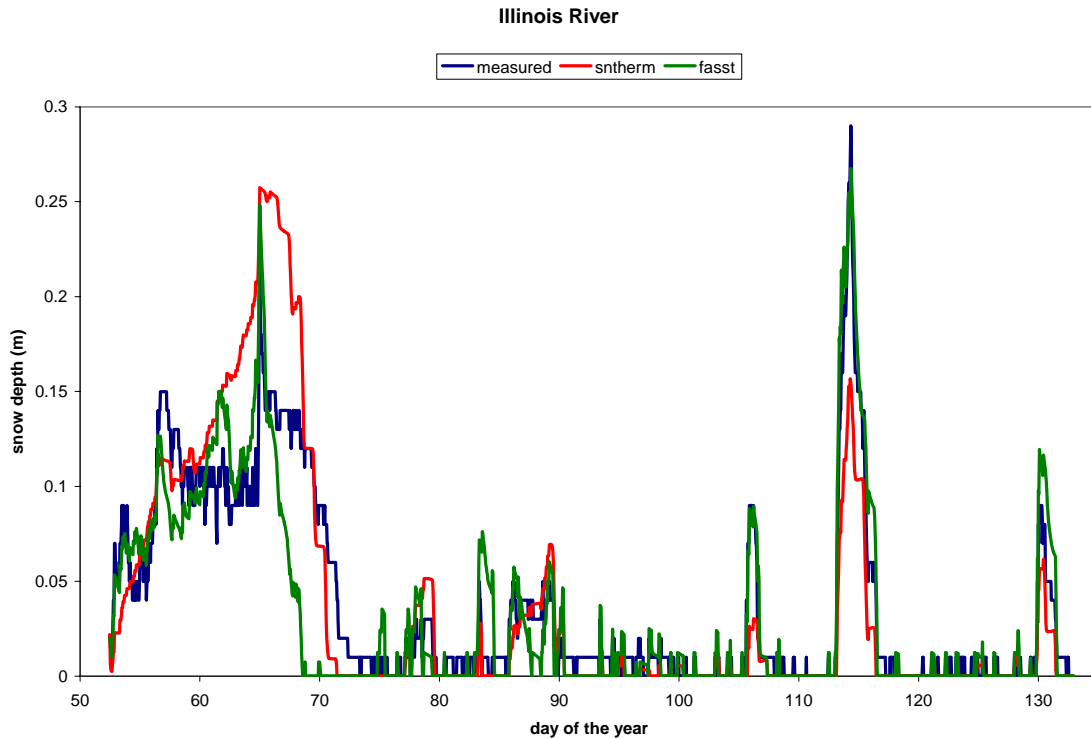


Figure 7.3 Comparison between the measured snow depth and the snow depth calculated by SNTHERM and FASST for Indian River, CO.

Figures 7.2 and 7.3 compare the results of FASST with those of SNTHERM against the measured values for two sites in Colorado. SNTHERM (Jordan 1991a) is considered the most physically based snow model. The Buffalo Pass site is characterized by an accumulation period followed by an ablation period that begins on approximately day 130. Both models accurately transition between the two seasons. FASST underestimates the meltout date by three days while SNTHERM overestimates it by three days. Within five days is considered accurate (Holcombe et al. 2004). The absolute (average of model–measured) and relative (average of [model–measured]/measured) errors for both models are 8% and 3%, respectively.

The snowpack at the Illinois River site, Figure 7.3, is characterized as thin, ephemeral, and windblown. This is a more difficult modeling scenario. Despite this, both models do well. The absolute error is < 1% while the relative error is 2 % for SNTHERM and 11% for FASST.

7.6 References

Albert, M., and G. Krajeski (1998) Fast, Physically Based Point Snow Melt Model for use in Distributed Applications. *Hydrological Process*, V. 12, p. 1809–1824.

Anderson, E.A. (1973) National Weather Service River Forecast System Snow Accumulation and Ablation Model. NOAA Technical Mem. NWS 17, Bethesda, MD.

Bader H., R. Haefeli, E. Bucher, J. Neher, O. Eckel, and C. Thams (1954) Snow and its Metamorphism, SIPRE Translation 14. U.S. Army Corps of Engineers Snow, Ice and Permafrost Organization, Hanover, NH.

Bender, J.A. (1957) Air Permeability of Snow. U.S. Army Corps of Engineers Snow, Ice and Permafrost Organization, Hanover, NH, SIPRE Research Report 37.

Brun, E. (1989) An Energy and Mass Model of Snow Cover Suitable for Operational Avalanche Forecasting. *Journal of Glaciology*, V. 35, No. 121, p. 333–342.

Carslaw, H.S., and J.C. Jaeger (1959) *Conduction of Heat in Solids*, Oxford: Clarendon Press.

Colbeck, S.C. (1972) A Theory of Water Percolation in Snow. *Journal of Glaciology*, V. 11, No. 63, p. 369–385.

Holcombe, J.D., K. Elder, S. Frankenstein, S. Fassnacht and R.E. Davis (2004) Seasonal Simulations of Snow Depth and Soil Moisture at Two Different NASA CLPX Sites. *Hydrological Processes*, submitted.

Jordan, R. (1991a) A One-Dimensional Temperature Model for a Snow Cover: Technical Documentation for SNTHERM.89. U.S. Army Cold Regions Research and Engineering Laboratory, Special Report 91-16.

Jordan, R. (1991b) Predicting Turbulent Transfer Functions for Use in Energy Balance Model. U.S. Army Cold Regions Research and Engineering Laboratory Internal Report 1107.

Kattleman, R. (1986) Measurements of Snow Layer Water Retention. Cold Regions Hydrology Symposium, American Water Resources Association, p. 377–386.

Kuroiwa, D. (1968) Liquid Permeability of Snow, IAHS Pub. 79, p. 380–391.

Morel-Seytoux, H.J (1969) Introduction to Flow of Immiscible Liquids in Porous Media. *Flow Through Porous Media*, R.J.M. De Wiest, Ed. New York: Academic Press, p. 455–516.

Mualem, Y. (1978) Hydraulic Conductivity of Unsaturated Porous Media: Generalized Macroscopic Approach, *Water Resources Research*, V. 14, No. 2, p. 324–334.

Shimizu, H. (1970) Air Permeability of Deposited Snow. *Contributions from the Institute of Low Temperature Science*, A(22), Hokkaido University, Sapporo, Japan, p. 1–32.

Sulahria, M.B (1972) Predictions of Water Retention Capacity of High-Elevation Snowpacks on the East Side of the Sierra Nevada. Unpublished Ph.D. dissertation. University of Nevada at Reno, p. 115, In Kattleman, R. (1986) Measurements of Snow Layer Water Retention, Cold Regions Hydrology Symposium, American Water Resources Association, p. 377–386.

Tucker, W., and S.C. Colbeck (1977) A Computer Routing of Unsaturated Flow Through Snow. U.S. Army Corps of Engineers, Cold Regions Research and Engineering Laboratory, Report 77-10.

Chapter 8

Ice Thickness Model

8.0 Introduction

Of great hindrance to mobility is the presence of ice on the ground. This can happen when the ground is at or below freezing and any precipitation is in the form of rain instead of snow.

8.1 Theory

8.1.1 Growth

The formation of an ice cover on the surface is allowed only if there is no snow. If snow is present, any rain that falls is assumed to percolate into the snowpack instead of forming an ice cover on the snow surface. Following Jones (1996), the fraction of precipitation that freezes is

$$f = \frac{\sum \text{heat fluxes} - \text{latent heat flux}}{\text{latent heat flux}}. \quad (8.1)$$

The sum of the heat fluxes is fully described in Chapter 6, Section 6.1. The resulting ice thickness, h_i (m) per unit area is

$$h_i = fP \frac{\Delta t}{3600} \frac{\rho_w}{\rho_i} \quad (8.2)$$

where P (m/hr) is the precipitation rate, Δt (sec) is the time step, ρ_w (kg/m^3) is the density of water, and ρ_i (kg/m^3) is the ice density.

8.1.2 Decay

Decay of an ice layer can occur from both the top and bottom, but only if enough energy is present at the corresponding interface. Once this condition is met, the resulting melt depths, $\Delta h_{i,top}$ (m) and $\Delta h_{i,bottom}$ (m), are

$$\begin{aligned} \Delta h_{i,top} &= q_{net} \frac{\Delta t}{\rho_i l_f} \\ \Delta h_{i,bottom} &= \kappa \frac{\partial t}{\partial z} \frac{\Delta t}{\rho_i l_f} \end{aligned} \quad (8.3)$$

where q_{net} (W/m^2) is the net surface heat flux, l_f (J/kg) is the latent heat of fusion, c_i ($J/kg \cdot K$) is the specific heat of ice, T_s (K) is the surface temperature, and κ is the soil thermal conductivity ($W/m \cdot K$). This is the same procedure used by the snow accretion and depletion model described in Chapter 9.

8.2 References

Jones, K.F. (1996) Ice Accretion in Freezing Rain. U.S. Army Cold Regions Research and Engineering Laboratory, Special Report 92-6.

Chapter 9

Model Inputs

9.0 Introduction

FASST requires four types of inputs: meteorological, soil properties, initial conditions, and site information. Actual structure of the input files is not discussed here. This information is found in the accompanying report, FASST User's Manual (Frankenstein 2004). Wherever possible, SEDRIS (Synthetic Environment Data Representation and Interchange Specification) nomenclature is used to describe the data in an attempt to standardize the process. More information concerning SEDRIS is found at <http://www.sedris.org>.

9.1 Meteorological Data

For FASST to operate with the most accuracy, the following meteorological data are required.

Year
Day of the Year
Hour of the Day
Minute of the Hour
Air Pressure (*mbar*)
Air Temperature (*K*)
Relative Humidity (%)
Wind Speed (*m/s*)
Wind Direction (*degrees* from N, + = clockwise)
Precipitation Rate (*mm/hr*)
Precipitation Type (SEDRIS enumeration)
Low Cloud Amount (*tenths*)
Low Cloud Height (*km*)
Low Cloud Type (SEDRIS enumeration)
Middle Cloud Amount (*tenths*)
Middle Cloud Height (*km*)
Middle Cloud Type (SEDRIS enumeration)
High Cloud Amount (*tenths*)
High Cloud Height (*km*)
High Cloud Type (SEDRIS enumeration)
Total Incoming Solar Radiation (Direct + Diffuse) (*W/m²*)
Direct Solar Radiation (*W/m²*)
Diffuse Solar Radiation (*W/m²*)
Reflected Solar Radiation (*W/m²*)
Net Solar Radiation (Total -Reflected) (*J/m²*)
Incoming Infrared Radiation (*W/m²*)

Emitted Infrared Radiation (W/m^2)
 Net Infrared Radiation (J/m^2)
 Solar Zenith Angle (*degrees*)
 Solar Azimuth Angle (*degrees*)
 Snow Depth (*m*)
 Soil Surface Temperature (*K*)

At a minimum, FASST requires that the user provide the observed air temperature along with the time and date. The data frequency may range from 1 minute to 24 hours, with the optimum range being 1–3 hours. If any of the above parameters are not provided, the following assumptions are made.

Air Pressure	1000 <i>mbar</i>
Relative Humidity	60%
Wind Speed	1.2 <i>m/s</i>
Wind Direction	0.0 <i>degrees</i>
Precipitation Rate	0.0 <i>mm/hr</i>
Precipitation Type	1 (none)
Low Cloud Amount	0.5 <i>tenths</i>
Low Cloud Height	1.5 <i>km</i>
Low Cloud Type	6 (stratus nebulosus or stratus fractus)
Middle Cloud Amount	0.0 <i>tenths</i>
Middle Cloud Height	4.0 <i>km</i>
Middle Cloud Type	3 altocumulus translucidus, 1 level
High Cloud Amount	0.0 <i>tenths</i>
High Cloud Height	8.0 <i>km</i>
High Cloud Type	5 (cirrus and/or cirrostratus < 45° above the horizon) if High Cloud Amount < 0.4 7 (cirrostratus, full cover) if High Cloud Amount > 0.4

Total Incoming Solar Radiation (Direct + Diffuse)	Model will calculate
Direct Solar Radiation	Model will calculate
Diffuse Solar Radiation	Model will calculate
Upwelling Solar Radiation	Model will calculate
Net Solar Radiation (Total – Upwelling)	Model will calculate
Incoming Infrared Radiation	Model will calculate
Emitted Infrared Radiation	Model will calculate
Net Infrared Radiation	Model will calculate
Solar Zenith Angle	Model will calculate
Solar Azimuth Angle	Model will calculate
Snow Depth	Model will calculate
Soil Surface Temperature	Model will calculate

The enumerations used for the precipitation and cloud types are based on SEDRIS.

9.2 Soil Properties

Besides the meteorological data, how representative the soil parameters are of the region being modeled has a significant effect on FASST's ability to accurately predict the state of the ground. At a minimum, the user must provide information concerning the number of layers (maximum is 10), layer thickness, and the layer USCS (Unified Soil Classification System) soil type. The soil parameters that FASST uses are

Bulk density of dry material (g/cm^3)	γ_d
Intrinsic density of dry material (g/cm^3)	ρ_d
Volume fraction of solids	θ_d
Porosity	n
Void Ratio	e
Albedo ($0.35\text{--}3.0\ \mu m$)	α
Emissivity ($3.0\text{--}100\ \mu m$)	ε
Quartz content	q
Organic Fraction	θ_{of}
Thermal conductivity of dry material ($W/m \cdot K$)	k_{th}
Specific heat of the dry material ($J/kg \cdot K$)	C
Saturated hydraulic conductivity (cm/s)	K_{sat}
Residual water content (vol/vol)	θ_r
Maximum water content (vol/vol)	θ_{max}
van Genuchten bubbling pressure head (cm)	α_{vG}
van Genuchten exponent	n_{vG}
Cone index/moisture content coefficient 1	c_1
Cone index/moisture content coefficient 2	c_2
Rating cone index/moisture content coefficient 1	c_1
Rating cone index/moisture content coefficient 2	c_2

Many of the above parameters are related. For instance, the bulk density (γ_d), mass per total volume, is related to intrinsic density (ρ_d), mass per fractional volume of solids, in the following manner $\gamma_d = \theta_d \rho_d$ where θ_d is the volume fraction of the solids to the soil as a whole. Remember also that the porosity, n , and void ratio, e , are related through $n = e/(1+e)$. In addition, the porosity is also a function of the volume of solids, θ_d , i.e., $n = 1 - \theta_d$.

The thermal conductivity of the bulk dry material (κ_{dry}) is related to the thermal conductivity of the solids (κ_s) by

$$\kappa_{dry} = \kappa_s^{(1-n)} \kappa_a^n \quad (9.1)$$

where $\kappa_a = 0.026\ W/m \cdot K$ is the thermal conductivity of air and n is the porosity. Unfortunately, the thermal conductivity of the solids is seldom known. A different approach, and the one used by FASST, is to calculate κ_{dry} based on (Farouki 1981):

$$\kappa_{dry} = \frac{0.135\gamma_d + 64.7}{2700 - 0.947\gamma_d} \pm 20\%. \quad (9.2)$$

The thermal conductivity is related to the specific heat such that $\kappa = k_{th} \cdot C$ where k_{th} is the thermal diffusivity (m^2/s) and C is the specific heat ($J/kg \cdot K$).

Finally, it should be noted that often, the saturated hydraulic conductivity, K_{sat} (cm/s), is called the saturated permeability, kp_{sat} (cm^2). The two are related by

$$K_{sat} = \frac{kp_{sat}g}{\nu} = \frac{(Nd^2)g}{\eta/\rho_f} \quad (9.3)$$

where N is a pore shape dependent proportionality factor, d (m) is the soil grain diameter, g (m/s^2) is the acceleration due to gravity, ν (m^2/s) is the kinematic fluid viscosity, η ($kg/m \cdot s$) is the dynamic fluid viscosity, and ρ_f is the fluid density (kg/m^3).

FASST provides default values for all of the above parameters, for 15 of the USCS soil types (see Tables 9.2.1 and 9.2.2). Parameters not found in the tables are calculated based on the preceding discussion. The USCS soil types that FASST allows are

GW	Well-graded gravels, gravel–sand mixtures, little or no fines
GP	Poorly graded gravels, gravel–sand mixtures, little or no fines
GM	Silty gravels, gravel–sand–silt mixtures
GC	Clayey gravels, gravel–sand–clay mixtures
SW	Well-graded sands, gravelly sands, little or no fines
SP	Poorly graded sands, gravelly sands, little or no fines
SM	Silty sands, sand–silt mixtures
SC	Clayey sands, sand–clay mixtures
ML	Inorganic silts and very fine sands, rock flour, silty or clayey fine sands or clayey silts with slight plasticity
CL	Inorganic clays of low to medium plasticity, gravelly clays, sandy clays, silty clays, lean clays
OL	Organic silts and organic silty clays of low plasticity
CH	Inorganic silts, micaceous or diatomaceous fine sandy or silty soils, elastic silts
MH	Inorganic clays of high plasticity, fat clays
OH	Organic clays of medium to high plasticity, organic silts
Pt	Peat and other highly organic soils
SMSC	Mixed SM and SC soils
CLML	Mixed CL and ML soils
EV	Evaporites (salt pans, similar properties to SW)
CO	Concrete
AS	Asphalt
RO	Bed rock (assumed to be granitic)
SN	Permanent snow field or glacier
UK	Unknown (This is defaulted to SM.)
US	User-supplied variables

If the soil type “US” is used, the user is then directed, in a step-by-step manner, to enter their values for the soil parameters. If any of the parameters are unknown, FASST reverts to the default values listed in Tables 9.2.1 and 9.2.2 as stated above.

Table 9.2.1 FASST Default Soil Properties

Soil Type	Bulk Dry Density γ_d (g/cm ³)	Porosity n	Emissivity ¹ ε	Albedo ¹ α	Quartz Content ² q	Organic Fraction θ_{of}	Fine/ Coarse [*]	Specific Heat ³ C_s (J/kg·K)
GW	1.95 ⁵	0.296 ⁵	0.92	0.40	0.65	0.00	1	820.0
GP	2.16 ⁵	0.203 ⁵	0.92	0.40	0.65	0.00	1	820.0
GM	1.91 ⁵	0.324 ⁵	0.95	0.40	0.65	0.00	1	820.0
GC	1.87 ⁵	0.34 ⁴	0.92	0.40	0.65	0.00	1	820.0
SW	1.876 ⁵	0.320 ⁵	0.92	0.40	0.80	0.00	1	830.0
SP	1.594 ⁵	0.415 ⁵	0.92	0.35	0.80	0.00	1	816.4 ⁷
SM	1.474 ⁵	0.526 ⁵	0.92	0.35	0.80	0.05	1	850.6
SC	1.88 ⁵	0.400 ⁵	0.92	0.35	0.80	0.05	1	830.0
ML	1.457 ⁵	0.464 ⁵	0.94	0.40	0.35	0.10	2	845.7 ⁷
CL	1.589 ⁵	0.422 ⁵	0.97	0.23	0.05	0.10	2	854.1 ⁷
OL	1.165 ⁵	0.533 ⁵	0.955	0.265	0.20	0.25	2	837.4 ⁷
CH	1.517 ⁵	0.457 ⁵	0.98	0.30	0.05	0.10	2	845.7 ⁷
MH	1.060 ¹	0.547 ¹	0.94	0.30	0.35	0.10	2	830.0
OH	0.841 ¹	0.892 ⁴	0.955	0.265	0.20	0.25	2	866.7 ⁷
PT	0.25	0.70	0.92	0.40	0.05	0.50	2	830.0
SMSC (MC)	1.60 ¹	0.396 ¹	0.92	0.40	0.80	0.05	1	830.0
CLML (CM)	1.617 ⁵	0.397 ⁵	0.96	0.30	0.20	0.10	2	830.0
EV	1.876 ⁵	0.320 ⁵	0.92	0.40	0.80	0.00	1	830.0
CO	2.185	0.020	0.90 ⁶	0.40 ⁶		0.00		850.0
AS	2.500	0.020	0.94 ⁶	0.125 ⁶		0.00		880.0
RO	2.700	0.020	0.89	0.40		0.00		800.0
SN	0.920	0.020	0.90	0.70		0.00		

* 1 = coarse, 2 = fine

¹ Sullivan et al. (1997), p. 28, 38, and 51

² Tarnawski et al. (1997), p. 96

³ Farouki (1981), p. 136

⁴ Yu et al. (1993)

⁵ Guymon, G.L. et al. (1993), p. 21, 25

⁶ Balick, L.K. et al. (1981), Table B1

⁷ Peck, L. (2002), Table 21

Table 9.2.2 FASST Default Soil Moisture Properties.

Soil Type	Saturated Hydraulic Conductivity K_{sat} (cm/s)	Residual Water Content θ_r (m^3/m^3)	Maximum Water Content θ_{max} (m^3/m^3)	<i>Van Genuchten exponent</i> n_{vG}	Bubbling Pressure Head α_{vG} (cm)	CI Coeff. c_1^I	CI Coeff. c_2^I	RCI Coeff. c_1^I	RCI Coeff. c_2^I
GW	0.00026 ²	0.01	0.296 ²	1.5 ³	22.6 ¹				
GP	0.0001056 ²	0.01	0.403 ²	2.2 ³	22.6 ¹				
GM	0.000067 ²	0.01	0.324 ²	1.2 ³	32.7 ¹				
GC	0.00001389 ¹	0.01	0.34 ⁴	1.5 ³	23.2 ¹				
SW	0.00002361 ²	0.01	0.320 ²	1.25 ³	38.547 ³	3.987	0.81500	3.987	0.8150
SP	0.00000741 ²	0.01	0.415 ²	2.5 ³	38.547 ³	3.987	0.81500	3.987	0.8150
SM	7.987e-06 ²	0.01	0.526 ²	1.4 ³	68.547 ³	8.749	-1.1949	12.542	-2.955
SC	0.000000029 ²	0.01	0.400 ²	1.5 ³	58.547 ³	9.056	-1.3566	12.542	-2.955
ML	0.000000057 ²	0.01	0.464 ²	1.5 ³	33.9 ¹	10.225	-1.565	11.936	-2.407
CL	7.7e-08 ²	0.01	0.422 ²	1.34 ³	53.5 ¹	10.998	-1.848	15.506	-3.530
OL	0.00009722 ²	0.01	0.533 ²	1.34 ³	28.6 ¹	10.977	-1.754	17.399	-3.584
CH	4.8e-08 ²	0.01	0.457 ²	1.5 ³	32.9 ¹	13.816	-5.583	13.686	-2.705
MH	1.5e-08 ¹	0.01	0.547 ²	1.34 ³	39.0 ¹	12.321	-2.044	23.641	-5.191
OH	0.000883 ¹	0.01	0.892 ⁴	1.34 ³	29.3 ¹	13.046	-2.172	12.189	-1.942
PT	0.000014	0.15	0.70	1.34	38.6				
SMSC (MC)	7.7e-07 ²	0.01	0.396 ²	1.5 ³	23.547 ³	9.056	-1.3566	12.542	-2.955
CLML (CM)	1.26e-07 ²	0.01	0.397 ²	1.34 ³	32.9 ¹	9.454	-1.3850	14.236	-3.137
EV	0.00002361 ²	0.01	0.320 ²	1.25 ³	38.547 ³	3.987	0.81500	3.987	0.8150
CO, AS, RO, SN	0.0	0.001	0.02						

¹ Sullivan et al. (1997), p. 28

² Guymon, et al. (1993), p. 21, 25, 47–59

³ Jordan (2000)

⁴ Yu et al. (1993)

Parameters in Table 9.2.2 are used to calculate the moisture content and resulting strength of the soil. They are needed for the soil moisture and soil strength subroutines of FASST. Unlike other models, the soil strength requires moisture content by weight and not by volume. The moisture/strength equations are a result of curve fitting. They are

$$CI = \exp[c_1 + c_2 \ln(MC)] \quad (9.4)$$

$$RCI = \exp[c_1 + c_2 \ln(MC)]$$

where CI is the cone index, RCI is the rating cone index, and MC is the moisture content by weight in percent (Sullivan et al. 1997). The rating cone index is used to quantify the strength of soils after traffic has passed.

The relationship between volumetric moisture content and pressure head is highly nonlinear. Following the work of van Genuchten (1980) it is

$$\theta_w = \theta_r + \frac{\theta_{\max} - \theta_r}{\left(1 + |\alpha\Psi|^{n_{vG}}\right)^{m_{vG}}} \quad (9.5)$$

where θ_r is the residual volumetric water content, θ_{\max} is the maximum volumetric water content, α_{vG} (cm^{-1}) is a constant related to the reciprocal of the bubbling pressure head, n_{vG} is a constant dependent on the distribution of pores, and $m_{vG} = 1 - 1/n_{vG}$. The hydraulic conductivity also depends on the volumetric moisture content such that (van Genuchten 1980)

$$K = K_{sat} w^{0.5} \left[1 - \left(1 - w^{1/m_{vG}} \right)^{m_{vG}} \right]^2 \quad (9.6)$$

where

$$w = \frac{\theta - \theta_r}{\theta_{\max} - \theta_r} \quad (9.7)$$

is the relative soil moisture.

9.3 Initial Conditions

FASST requires very little information concerning the initial conditions. At a minimum, it needs to know the initial snow depth and/or ice thickness on the surface. If the initial soil temperature and moisture profiles are known, the user can also input this information.

9.4 Site Information

Several parameters describing the site are needed by FASST. They are

Site Latitude (+ = North)

Site Longitude (+ = East from Prime Meridian)

Site Elevation (m, ft)

Time Offset between Local and Universal Time Conversion (UTC) (hr)
[local – UTC]

Slope (Degrees from horizontal)

Aspect Angle (Degrees from North, + = clockwise)

Surface Vegetation 0 = unknown

8 = grass/pasture/steppe/meadow

50 = mixed trees

999 = other

The vegetation enumerations are based on SEDRIS nomenclature. At present, the vegetation simply changes the surface albedo and emissivity. The next release of the model will include a two-layer vegetation model including root uptake of soil moisture.

9.5 References

Balick, L.K., L.E. Link, R.K. Scoggins, and J.L. Solomon (1981) Thermal Modeling of Terrain Surface Elements. U.S. Army Engineer Waterways Experiment Station, Technical Report EL-81-2.

Farouki, O.T. (1981) Thermal Properties of Soils. U.S. Army Cold Regions Research and Engineering Laboratory, Monograph 81-1.

Frankenstein, S. (2004) FASST User's Manual.

Guymon, G.L., R.L. Berg, and T.V. Hromadka (1993) Mathematical Model of Frost Heave and Thaw Settlement in Pavements. U.S. Army Cold Regions Research and Engineering Laboratory, CRREL Report 93-2.

Jordan, R. (2000) User's Guide for USACRREL One-Dimensional Coupled Soil and Snow Model (SLTHERM).

Peck, L. (2002) Battlespace Terrain Reasoning and Awareness Soil Properties Database Population.

Sullivan, P.M., C.D. Bullock, N.A. Renfroe, M.R. Albert, G.G. Koenig, L. Peck, and K. O'Neill (1997) Soil Moisture Strength Prediction Model Version II (SMSPII). U.S. Army Corps of Engineers Waterways Experiment Station, Technical Report GL-97-15.

Tarnawski, V.R., B. Wagner, J. Webber, and L. Pettipas (1997) Optimization of Soil Mineralogical Composition for Predicting Soil Thermal Conductivity. In *Proceedings, International Symposium on Physics, Chemistry and Ecology of Seasonally Frozen Soils*, I.K. Iskandar, E.A. Wright, J.K. Radke, B.S. Sharratt, P.H. Groenevelt, L.D. Hinzman (Ed.), Fairbanks, AK, June 10–12. U.S. Army Cold Regions Research and Engineering Laboratory, Special Report 97-10, p. 91–97.

van Genuchten, M. Th. (1980) A Closed-Form Equation for Predicting the Hydraulic Conductivity of Unsaturated Soils. *Soil Science Society of America Journal*, Vol. 44.

Yu, C., C. Loureiro, J.-J. Cheng, L.G. Jones, Y.Y. Wang, Y.P. Chia, and E. Faillace (1993) Data Collection Handbook to Support Modeling Impacts of Radioactive Material in Soil. Environmental Assessment and Information Sciences Division, Argonne National Laboratory, Argonne, Illinois (www.ead.anl.gov/resrad/datacoll/dcall.htm).

Chapter 10

Model Initialization

10.0 Introduction

Before any calculations can be made, the surface conditions as well as the temperature, volumetric moisture content, and soil properties profiles must be determined. The initial nodal spacing and number of nodes are also calculated.

10.1 Surface Conditions

The presence of snow or ice affects both the soil temperature and the volumetric moisture content. It also influences the radiative properties of the surface, specifically the albedo and emissivity.

The albedo is a measure of the amount of solar radiation that is reflected by the surface. It is the ratio of the reflected to the total incoming solar radiation. The greater the albedo, the less shortwave radiation is absorbed by the surface. Value of the albedo for a snow-covered soil range between $\alpha_s = 0.78$ or 0.55 following Pomeroy et al. (1998), depending on the age of the snow (see Chapter 7.2.7). For ice-covered soil $\alpha_i = 0.70$. The albedo values for the USCS soil types are given in Table 9.2.1.

The emissivity of a material is the ratio of its emitted energy to emitted infrared radiation in the spectral band from xxx to yyy to that of a black body, or perfect absorber, at the same temperature. It influences the amount of longwave radiation that the surface loses to the atmosphere. If the surface is snow- or ice-covered, the emissivity is $\varepsilon_s = 0.98$ or $\varepsilon_i = 0.90$, respectively. The emissivity values for the USCS soils are given in Table 9.2.1.

10.2 Temperature and Volumetric Moisture and Ice Content Profiles

If the user has any initial soil temperature or volumetric moisture content data, FASST incorporates these into the calculated profiles. For both parameters FASST assumes a linear profile as a function of depth between any consecutive fixed values.

If no initial surface temperature is given, FASST assumes that the soil surface temperature is equal to the air temperature if there is no snow or ice on the ground. If snow or ice is present, FASST sets the soil surface temperature to 0.0°C . If the temperature of the lowest model layer is not provided, FASST assigns a value equal to the surface temperature or the lowest given nodal temperature.

FASST presumes that the initial volumetric soil moisture content at the surface is equal to the residual moisture allowed plus 30% of the difference between the maximum and

residual values unless the user provides a value. The bottom soil moisture is assigned the average value of the residual and maximum moisture contents for the USCS soil type present in Table 9.2.2.

If the temperature of the soil is frozen at any depth, the volumetric ice content at that position equals $0.95 * (\text{soil moisture}) * (\text{water density}) / (\text{ice density})$.

10.3 Node Position and Number

FASST requires a minimum soil depth of 1.0 *m*. If the user-specified depth is less than this, FASST extends the bottom soil layer until the total thickness is 1.0 *m*.

Node spacing is determined by both the number of soil temperature and moisture observations as well as the number of soil layers. If measured temperature and/or moisture values exist, a node is placed at each observation location. Nodes also occur at any layer boundary if there are different soil types as well as the soil surface and bottom. If no initial measurements are provided, 10 nodes are equally spaced through the total soil thickness and at any layer boundaries, the surface, and bottom. Soil type dependent, temperature and moisture independent, parameters are assigned to the nodes depending on which layer they are in. Nodes located at layer boundaries have the properties of the upper layer.

10.4 Time Step Determination

Once the soil type, temperature, and volumetric moisture content are known at a node, the corresponding hydraulic and thermal properties of the soil are calculated. The thermal model calculation time step, Δt (*sec*), is then calculated based on the numerical stability requirement for the soil temperature. Namely for each node,

$$k_{th,i} \frac{\Delta t}{(\Delta z_i)^2} < 0.5 \rightarrow \Delta t = \min \left[\frac{0.45 (\Delta z_i)^2}{k_{th,i}} \right] \quad (10.1)$$

where $k_{th,i}$ (m^2/s) is the thermal diffusivity of the soil and Δz_i (*m*) is the nodal spacing and the subscript *i* refers to the node. Since the thermal diffusivity varies with soil type and temperature, the time step also varies. As indicated in Equation (10.1), the minimum value needed to satisfy all nodal conditions is used.

With the determination of the number of nodes and their placement, as well as the assignment of nodal properties, initialization of FASST is complete.

10.5 References

Pomeroy, J.W., D.M. Gray, K.R. Shook, B. Toth, R.L.H. Essery, A. Pietroniro, and N. Hedstrom (1998) An evaluation of snow accumulation and ablation processes for land surface modeling. *Hydrological Processes*, 12, 2339–2367.

Chapter 11

Model Outputs

11.0 Introduction

FASST produces two output files. One contains information pertaining to the surface conditions and the other contains soil profile information. Details concerning the actual setup of the two files may be found in the FASST User's Manual (Frankenstein 2004).

11.1 Surface Condition Information

At each time step the following meteorological data and surface data are output.

Year

Day of the Year

Hour of the Day

Minute of the Hour

Air Pressure (*mbar*)

Air Temperature (*K*)

Relative Humidity (%)

Wind Speed (*m/s*)

Wind Direction (*degrees* from N, + = clockwise)

Precipitation Rate (*mm/hr*)

Precipitation Type (0 = unknown, 1 = none, 2 = rain, 3 = snow, 4 = freezing rain)

Low Cloud Amount (*tenths*)

Low Cloud Height (*km*)

Low Cloud Type

(If BTRA (VITD): 0 = none, 1 = stratus, 2 = stratocumulus, 3 = cumulus

Else (SEDRIS): 0 = none

1 = cumulus humulis or cumulus fractus

2 = cumulus mediocris or congestus

3 = cumulonimbus calvus with/out cumulus
stratocumulus or stratus

4 = stratocumulus cumulogenitus

5 = other stratocumulus types

6 = stratus nebulosus and/or startus fractus

7 = startus fractus and/or cumulus fractus of bad weather

8 = cumulus and stratocumulus

9 = cumulonimbus capillatus

99 = no clouds visible

Middle Cloud Amount (*tenths*)

Middle Cloud Height (*km*)

Middle Cloud Type

(If BTRA (VITD): 0 = none, 1 = altostratus, 2 = altocumulus,
3 = altocumulus castellanus
Else (SEDRIS): 0 = none
1 = altostratus translucidus
2 = altostratus opacus or nimbostratus
3 = altocumulus translucidus, 1 level
4 = altocumulus translucidus, many levels, varying
5 = altocumulus translucidus in bands
6 = altocumulus cumulogenitus or cumulonimbo genitus
7 = altocumulus translucidus or opacus, multi layer
8 = altocumulus castellanus or floccus
9 = chaotic altocumulus
99 = no clouds visible
High Cloud Amount (*tenths*)
High Cloud Height (km)
High Cloud Type

(If BTRA (VITD): 0 = none, 1 = cirrus, 2 = cirrostratus, 3 = cirrocumulus

Else (SEDRIS): 0 = none,
1 = cirrus fibratus,
2 = cirrus spissatu, patchy
3 = cirrus spissatus cumulonimbo genitus
4 = cirrus unicinus and/or fibratus
5 = cirrus and/or cirrostratus < 45° above horizon
6 = cirrus and/or cirrostratus > 45° above horizon
7 = cirrostratus full cover
8 = cirrostratus not full cover
9 = cirrocumulus
99 = no clouds visible

Total Incoming Solar Radiation (Direct + Diffuse) (W/m^2)

Direct Solar Radiation (W/m^2)

Diffuse Solar Radiation (W/m^2)

Reflected Solar Radiation (W/m^2)

Net Solar Radiation (Total -Reflected) (J/m^2)

Incoming Infrared Radiation (W/m^2)

Emitted Infrared Radiation (W/m^2)

Net Infrared Radiation (J/m^2)

Solar Zenith Angle (*degrees*)

Solar Azimuth Angle (*degrees*)

Snow Depth (m)

Ice Thickness (m)

Soil Surface Temperature (K)

Soil Surface Moisture (0 – 5cm) (vol/vol)

Surface Cone Index

Surface Rating Cone Index

Freeze/Thaw Depth (m)

State of Freeze/Thaw Depth ('frozen/'thawed/'unfrozen)

Visibility (km)

Aerosol Type (0 = unknown, 1 = none, 2 = mist, 3 = dust, 4 = smoke, 5 = haze, 6 = ocean spray, 7 = sand, 8 = volcanic ash, 9 = other)

Snow density (g/cm³)

Slippery Indicator for mobility (0 = not slippery, 1 = wet, 2 = ice, 3 = snow)

11.2 Soil Profile Information

At each time step, the following information is output for each node. Node 1 is at the surface.

Year

Day of the Year

Hour of the Day

Minute of the Hour

Node Number

USCS Soil Type

Soil Temperature (K)

Soil Moisture (vol/vol)

Ice Content (vol/vol)

Total Moisture (Soil Moisture + Ice Content) (vol/vol)

Frozen/Thawed State

11.3 Input/Output Data Source Information

Every user of FASST will not have all of the input data needed. As a result, FASST either uses default values or calculates the parameters internally. If a default value is employed, a flag of “1” is written to this file along with the variable name and the corresponding value. If the model calculates the parameter, a flag of “2” is written to the file along with the name of the variable. An example of such a file for the Grayling, MI, input data is shown in Figure 5 of the FASST User’s Manual (Frankenstein 2004). As a default this file is named “inferred.out.”

11.4 References

Frankenstein, S. (2004) FASST User’s Manual.

REPORT DOCUMENTATION PAGE

Form Approved
OMB No. 0704-0188

Public reporting burden for this collection of information is estimated to average 1 hour per response, including the time for reviewing instructions, searching existing data sources, gathering and maintaining the data needed, and completing and reviewing this collection of information. Send comments regarding this burden estimate or any other aspect of this collection of information, including suggestions for reducing this burden to Department of Defense, Washington Headquarters Services, Directorate for Information Operations and Reports (0704-0188), 1215 Jefferson Davis Highway, Suite 1204, Arlington, VA 22202-4302. Respondents should be aware that notwithstanding any other provision of law, no person shall be subject to any penalty for failing to comply with a collection of information if it does not display a currently valid OMB control number. PLEASE DO NOT RETURN YOUR FORM TO THE ABOVE ADDRESS.

1. REPORT DATE (DD-MM-YY) September 2004		2. REPORT TYPE Special Report		3. DATES COVERED (From - To)	
4. TITLE AND SUBTITLE Fast All-season Soil STrength (FASST)				5a. CONTRACT NUMBER	
				5b. GRANT NUMBER	
				5c. PROGRAM ELEMENT NUMBER	
6. AUTHOR(S) Susan Frankenstein and George G. Koenig				5d. PROJECT NUMBER	
				5e. TASK NUMBER	
				5f. WORK UNIT NUMBER	
7. PERFORMING ORGANIZATION NAME(S) AND ADDRESS(ES) U.S. Army Engineer Research and Development Center Cold Regions Research and Engineering Laboratory 72 Lyme Road Hanover, NH 03755-1290				8. PERFORMING ORGANIZATION REPORT ERDC/CRREL SR-04-1	
9. SPONSORING/MONITORING AGENCY NAME(S) AND ADDRESS(ES) U.S. Army Corps of Engineers Washington, DC 20314-1000				10. SPONSOR / MONITOR'S ACRONYM(S)	
				11. SPONSOR / MONITOR'S REPORT NUMBER(S)	
12. DISTRIBUTION / AVAILABILITY STATEMENT Approved for public release; distribution is unlimited. Available from NTIS, Springfield, Virginia 22161.					
13. SUPPLEMENTARY NOTES					
14. ABSTRACT The ability to predict the state of the ground is essential to manned and unmanned vehicle mobility and personnel movement, as well as determining sensor performance for both military and civilian activities. As part of the Army's Battlespace Terrain Reasoning and Awareness research program, the 1-D dynamic state of the ground model FASST (Fast All-season Soil STrength) was developed. It calculates the ground's moisture content, ice content, temperature, and freeze/thaw profiles, as well as soil strength and surface ice and snow accumulation/depletion. The fundamental operations of FASST are the calculation of an energy and water budget that quantifies both the flow of heat and moisture within the soil and also the exchange of heat and moisture at all interfaces (ground/air or ground/snow; snow/air) using both meteorological and terrain data. FASST is designed to accommodate a range of users, from those who have intricate knowledge of their site to those who know only the site location. It allows for 22 different terrain materials, including asphalt, concrete, bedrock, permanent snow, and the USCS soil types. At a minimum, the only weather information required is air temperature.					
15. SUBJECT TERMS Freeze/thaw Ground temperature Snow depth		Soil moisture Soil strength Surface icing			
16. SECURITY CLASSIFICATION OF: a. REPORT U			17. LIMITATION OF OF ABSTRACT U	18. NUMBER OF PAGES 106	19a. NAME OF RESPONSIBLE PERSON 19b. TELEPHONE NUMBER (include area code)
b. ABSTRACT U			c. THIS PAGE U		

DEPARTMENT OF THE ARMY
ENGINEER RESEARCH AND DEVELOPMENT CENTER, CORPS OF ENGINEERS
COLD REGIONS RESEARCH AND ENGINEERING LABORATORY, 72 LYME ROAD
HANOVER, NEW HAMPSHIRE 03755-1290

Official Business